RICE UNIVERSITY

Synthesis and Chemical Modification of Carbon Nanostructures for Materials Applications

by

Amanda Lynn Higginbotham

A THESIS SUBMITTED
IN PARTIAL FULFILLMENT OF THE
REQUIREMENTS FOR THE DEGREE

Doctor of Philosophy

APPROVED, THESIS COMMITTEE:

James M. Tour, Chair
Chao Professor of Chemistry, Professor of Mechanical Engineering & Materials Science and Professor of Computer Science

Paul S. Engel
Professor of Chemistry

Pulickel M. Ajayan
Benjamin M. & Mary Greenwood Anderson Professor in Engineering and Professor of Mechanical Engineering & Materials Science

HOUSTON, TEXAS

AUGUST 2009

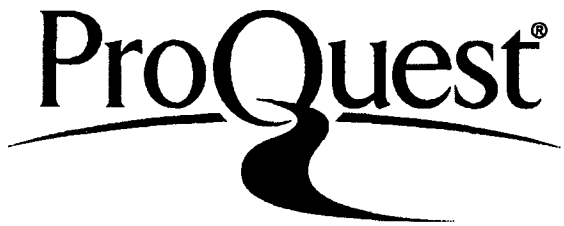

ProQuest LLC
789 East Eisenhower Parkway
P.O. Box 1346
Ann Arbor, MI 48106-1346

RICE UNIVERSITY

Synthesis and Chemical Modification of Carbon Nanostructures for Materials Applications

A THESIS SUBMITTED
IN PARTIAL FULFILLMENT OF THE
REQUIREMENTS FOR THE DEGREE

Doctor of Philosophy

by

Amanda Lynn Higginbotham

HOUSTON, TEXAS

AUGUST 2009

ABSTRACT

Synthesis and Chemical Modification of Carbon Nanostructures for Materials Applications

by

Amanda Lynn Higginbotham

This dissertation explores the structure, chemical reactivities, electromagnetic response, and materials properties of various carbon nanostructures, including single-walled carbon nanotubes (SWCNTs), multi-walled carbon nanotubes (MWCNTs), graphite, and graphene nanoribbons (GNRs). Efficient production and modification of these unique structures, each with their own distinct properties, will make them more accessible for applications in electronics, materials, and biology.

A method is reported for controlling the permittivity from 1 – 1000 MHz of SWCNT-polymer composites (0.5 wt%) for radio frequency applications including passive RF antenna structures and EMI shielding. The magnitude of the real permittivity varied between 20 and 3.3, decreasing as higher fractions of functionalized-SWCNTs were added.

The microwave absorbing properties and subsequent heating of carbon nanotubes were used to rapidly cure ceramic composites. With less than 1 wt% carbon nanotube additives and 30 – 40 W of directed microwave power (2.45 GHz), bulk composite samples reached temperatures above 500 °C within 1 min.

Graphite oxide (GO) polymer nanocomposites were developed at 1, 5, and 10 wt% for the purpose of evaluating the flammability reduction and materials properties of the resulting systems. Microscale oxygen consumption calorimetry revealed that addition of GO reduced the total heat release in all systems, and GO-polycarbonate composites demonstrated very fast self-extinguishing times in vertical open flame tests.

A simple solution-based oxidative process using potassium permanganate in sulfuric acid was developed for producing nearly 100% yield of graphene nanoribbons (GNRs) by lengthwise cutting and unraveling of MWCNT sidewalls. Subsequent chemical reduction of the GNRs resulted in restoration of electrical conductivity. The GNR synthetic conditions were investigated in further depth, and an improved method which utilized a two-acid reaction medium was found to produce GNRs with fewer defects and/or holes on the basal plane and higher aspect ratio.

Two different covalent functionalization methods for GNRs based on diazonium chemistry were developed. The resulting functionalized GNRs (f-GNRs) are readily soluble in organic solvents which increase their solution processability. The f-GNRs were also found to be in a reduced state, with minimal sp^2 carbon disruption, while also keeping the ribbon shape.

Acknowledgments

As with any great achievement in life, earning a Ph.D. would not have been possible without the support and involvement of many people. This is definitely true for me, as I have many to thank for helping me get where I am today. First and foremost, I would like to thank my advisor, Prof. James M. Tour, for eagerly welcoming into his group 4 years ago with promises of exciting research and boundless opportunities. I don't think either of us imagined this would include a *Nature* cover article, but with or without it, he held up to his promise. I am grateful for not only the chemistry knowledge Prof. Tour passed on to me, but for his diligence in teaching the importance of presentation and communication skills. He gave me opportunities to work with amazing scientists – both inside and outside of Rice – from which I learned some of my most valuable lessons while in graduate school.

The involvement and expertise of others for successful completion of any research project is absolutely essential. I have many to thank for their advice, experimental assistance, and training over the last 4 years – from the Tour lab: Jason Stephenson, Jared Hudson, Jay Lomeda, Alex Sinitskii, Zhengzong Sun, and Yu Zhu. Thank you to Wei Lu and Daniela Marcano for taking an interest in my projects and being wonderful students who were a pleasure to train during my final year. I need to give a special thank you to Dmitry Kosynkin, probably the most brilliant chemist I will ever meet. His willingness to try anything in the lab is both scary and admirable, but as the first the unzip a carbon nanotube, he is

obviously doing something right. Without the opportunity to work alongside Dmitry, many of the results written in this thesis would not have been possible.

I would also like to thank the other talented scientists I have worked with from Rice – Prof. Matteo Pasquali, Juan Duque, Nicholas Parra-Vasquez, Natnael Behabtu, Micah Green, Dr. Howard Schmidt, and Carter Kittrell. I am especially grateful to the Rice SEA and for the instrument expertise and eternal patience of Angelo Benedetto, Wenhua Guo, and Bo Chen. Dr. Dustin James deserves a BIG thank you for being the backbone of the Tour lab – he does all the behind-the-scenes magic and has helped me tremendously over the past 4 years.

Many people outside of Rice contributed to my fruitful graduate school experience – Dr. Christina Drake and all my colleagues at Lockheed Martin Missiles and Fire Control for a wonderful internship experience and showing me that working in industry is an exciting career option; collaborators Prof. Leo Kempel and Daniel Killips from Michigan State, as well as Dr. Alexander Morgan from the University of Dayton Research Institute; Padraig Moloney, Dr. Leonard Yowell, and Dr. Sivaram Arepalli as co-investigators at NASA Johnson Space Center. I would also like to thank my high school chemistry teacher Ms. Donna Tate for sparking in me an early interest in chemistry, and for pushing me to participate in the Welch Summer Scholar Program, which became the reason I decided to major in chemistry and continue on to graduate school. I learned a great deal in my undergraduate research experience, and owe thanks to Prof.

Abraham Clearfield and Dr. Joy Heising for guiding me through my first research project.

Emotional support in the form of friends and family is a very important part of my life and contributed greatly to successful completion of my Ph.D. I know I could not have done it without Ashley Leonard – my sister and friend both inside and outside the lab. I could go to her with anything, and I know that our friendship will continue well beyond graduate school. I am grateful to my labmates who also became my friends and were always there for me with advice, some comic relief or a beer at Valhalla – Katherine Price, David Corley, Jason Guerrero, Jay Lomeda, and Jacob Berlin. I would also like to thank my fellow 2005 class members – our continued encouragement and support over the years has helped us all to make it through!

Thank you also to Angela Thomas, Corinne Allen, Nate Pettigrew, and Nicholas Parra-Vasquez for their unending support and lots of good times.

Without a doubt I can say that my family has been the most important thing in my life which has allowed me to reach my goals – my parents instilled early on the importance of hard work and honesty. They gave me the confidence to believe that I could do anything I set my mind to, and then supported me unconditionally as I worked towards each of my goals. For that, they too own a portion of my degrees and I will forever be indebted to them. Thank you to my Gee-Maw the unending love and encouragement; she has been there for every important phase of my life and never leaves a doubt in my mind that she is proud of me. Thank you to Juan – my rock, my strength, my guide, and my love – he

has experienced almost every step of graduate school with me and made so many things possible. Thank you to Mimi, Isa, and the beautiful Sarita – they taught me so many important lessons on life and love, and helped me to maintain perspective and balance. There was never a shortage of warmth, hugs, and home-cooked meals with them in my life.

I dedicate this thesis to my three guardian angels in heaven. Although they are not here with me physically, there is never a doubt in my mind that they are guiding me along my way, assuring me that the paths I have chosen are the ones I am meant to take.

Table of Contents

List of Figures and Illustrations

List of Symbols and Abbreviations

Å	angstroms
ABS	acrylonitrile butadiene styrene
AFM	atomic force microscopy
ATR-IR	attenuated total-reflectance infrared
a.u.	arbitrary units
BET	Brunauer-Emmett-Teller (surface area theory)
°C	*degrees Celsius*
CCG	chemically converted graphene
$CHCl_3$	chloroform
cm	centimeter(s)
cm^{-1}	inverse centimeters
CNT	carbon nanotube
CV	cyclic voltammetry
CVD	chemical vapor deposition
d	day(s)
DFT	density functional theory
DMA	dynamic mechanical analysis
DMF	*N,N*-dimethylformamide
ε	epsilon (permittivity)
Et_2O	diethyl ether
EMI	electromagnetic interference
eV	electron volt(s)
Fc	ferrocene
f-GNR	functionalized graphene nanoribbon
FFT	Fourier transform diffractogram
f-MWCNT	functionalized multi-walled carbon nanotube
FT-IR	Fourier transform infrared spectroscopy
f-SWCNT	functionalized single-walled carbon nanotube
g	gram(s)

GNR	graphene nanoribbon
GONR	graphene oxide nanoribbon
GPa	gigapascal
GHz	gigahertz
GO	graphite oxide
h	hour(s)
HAADF	high angle annular dark-field (TEM)
HCl	hydrochloric acid
HNO_3	nitric acid
H_2O_2	hydrogen peroxide
H_2SO_4	sulfuric acid
H_3PO_4	phosphoric acid
HiPco	high-pressure carbon monoxide
HIPS	high-impact polystyrene
HRTEM	high resolution transmission electron microscopy
IR	infrared
I_{sd}	source-drain current
K	Kelvin
$KMnO_4$	potassium permanganate
λ	wavelength
L	Liter(s)
μ	micro, mu (permeability)
m	meter(s)
M	moles per liter
MCC	microcombustion calorimetry
MHz	megahertz
MeOH	methanol
min	minute(s)
mL	milliliters
mol	mole(s)
MW	microwave

MWCNT	multi-walled carbon nanotube
$NaBH_4$	sodium borohydride
NaOH	sodium hydroxide
N_2H_4	hydrazine
NH_4OH	ammonium hydroxide
nm	nanometer
PC	polycarbonate
PMMA	poly(methyl methacrylate)
pSWCNT	purified single-walled carbon nanotube
PTFE	polytetrafluoroethylene (Teflon)
RBMs	radial breathing modes (Raman spectroscopy)
RF	radiofrequency
rpm	revolutions per minute
rSWCNTs	raw single-walled carbon nanotubes
s	second(s)
S	Siemens
SDS	sodium dodecylsulfate
SEM	scanning electron microscopy
SiC	silicon carbide
SWCNT	single-walled carbon nanotube
TEM	transmission electron microscopy
TFA	trifluoroacetic acid
TFAA	trifluoroacetic anhydride
TGA	thermogravimetric analysis
THF	tetrahydrofuran
T_{max}	maximum temperature
T_g	glass transition temperature
UHV	ultra-high vacuum
UV	ultraviolet
V	volt(s)
wt%	weight percent

W	watts
XGONR	extreme graphene oxide nanoribbon
XGNR	extreme graphene nanoribbon
XPS	x-ray photoelectron spectroscopy
XRD	x-ray diffraction
V	volt(s)
V_g	gate voltage
V_{ds}	source-drain voltage
Z	impedence

Thesis Summary

This work focuses on the synthesis, manipulation and application of the following carbon nanomaterials: single-walled carbon nanotubes (SWCNTs), multi-walled carbon nanotubes (MWCNTs), sheets of oxidized graphene derived from bulk graphite, and graphene nanoribbons produced from longitudinal unzipping of MWCNTs. Chapter 1 gives an overall introduction to these nanomaterials including their significant properties and applications.

Chapter 2 demonstrates bulk permittivity control of SWCNT polymer composites based on variations in the amount of raw and functionalized SWCNTs that are incorporated. With only a total 0.5 wt% of SWCNTs included in the composites, the permittivity values ranged between 20 and 3 (for the real component) from 1 to 1000 MHz.

It was found that carbon nanotubes (CNTs) absorb 2.45 GHz microwave radiation resulting in intense heating and light emission. Although the mechanism is not well understood, the phenomenon applied to CNT composite curing is explored in Chapter 3. Ceramic composites were developed containing less than 1 wt% carbon nanotube additives and subsequently exposed to 30 – 40 W of directed microwave power (2.45 GHz); the bulk composite samples reached temperatures above 500 °C within 1 min and 1000 °C in 5 min. The heating rates of MWCNTs, functionalized MWCNTs, raw SWCNTs, and purified SWCNTs were compared.

Chapter 4 explores the incorporation of graphite oxide at 1, 5, and 10 wt% into polycarbonate, acrylonitrile butadiene styrene, and high-impact polystyrene

for the purpose of evaluating the flammability reduction and materials properties of the resulting systems.

Chapter 5 presents a simple, high-yielding solution-based procedure for production of large amounts of mono- and few-layer carbon nanoribbons from MWCNTs via oxidative longitudinal cleavage of the tube sidewalls in sulfuric acid. After isolation, the resulting oxidized nanoribbons are of high quality with straight edges and high aspect ratios; they are highly soluble in water (12 mg/mL), ethanol, and other polar organic solvents and can be chemically reduced for restoration of the electrical conductivity. Chapter 6 discusses variations in the nanoribbon-production procedure and related changes in reaction conditions such as time, temperature, and presence a second acid to the properties of the produced ribbons. A new ideal method is presented for the production of low-defect oxidized nanoribbons. Chapter 7 extends SWCNT and suspended graphene sheet diazonium functionalization techniques previously discovered in our laboratory to surfactant-wrapped nanoribbons in the reduced form. Upon attachment of various organic moieties to the basal plane of the ribbons, the solubility in organic solvents such as *N,N*-dimethylformamide (DMF) and *N*-methyl-2-pyrrolidinone (NMP) increases from essentially 0 to approaching 1 mg/mL.

Chapter 1

Introduction and Background: Carbon Nanomaterials

The 1985 discovery of fullerenes,[1] including the "bucky ball" – a third form of ordered carbon – was the catalyst which set off an explosion of interest in carbon nanomaterials. Subsequent discoveries of related novel forms of carbon were later made, the most significant being the first report of carbon nanotubes in 1991.[2] The physical characteristics of many types of carbon nanomaterials are actively being explored because of the intriguing possibilities they offer in electronics, materials, and biological applications. These include any all-carbon species – crystalline or non-crystalline – that contains at least one dimension in the nanoscale; fullerenes, carbon nanotubes (single, double, or multiple walls), nanohorns, some forms of carbon fibers, graphene, and nanodiamond are all examples. Each of these materials offers a unique set of properties that are actively being explored for improvements in synthesis and scale-up, as well for industrial applications.

1.1 Carbon nanotubes

1.1.1 Properties

Carbon nanotubes (CNTs) may be thought of as cylindrical sheets of graphene or extended hexagonal arrays of sp^2-hybridized carbon with a conjugated π-system. The sidewalls are arranged in a helical fashion around the tube axis and may be considered single-dimensional objects due to the small outer diameters (nm) and high length-to-width aspect ratio (typically greater than 100). Common methods for producing CNTs include the electric-arc discharge,[3,4] laser vaporization,[5,6] and chemical vapor deposition (CVD) techniques.[7-9] The

most commonly used synthesis method is CVD; this process involves the decomposition of an organic gas over a substrate covered with metal catalyst particles. This technique is usually preferred because it is scalable and the CNTs produced may be used directly without further purification, unless the final material requires catalyst particle removal.[10] Based on the reaction conditions and/or catalyst used, CNTs can be synthesized as multi-walled carbon nanotubes (MWCNTs, 5-100 nm diameter) which are composed of several tubes lying within one another concentrically, or as single-walled carbon nanotubes (SWCNTs, 1-3 nm diameter) as shown in Figure 1.1. The tubes which make up MWCNTs are bound together by weak van der Waals forces.

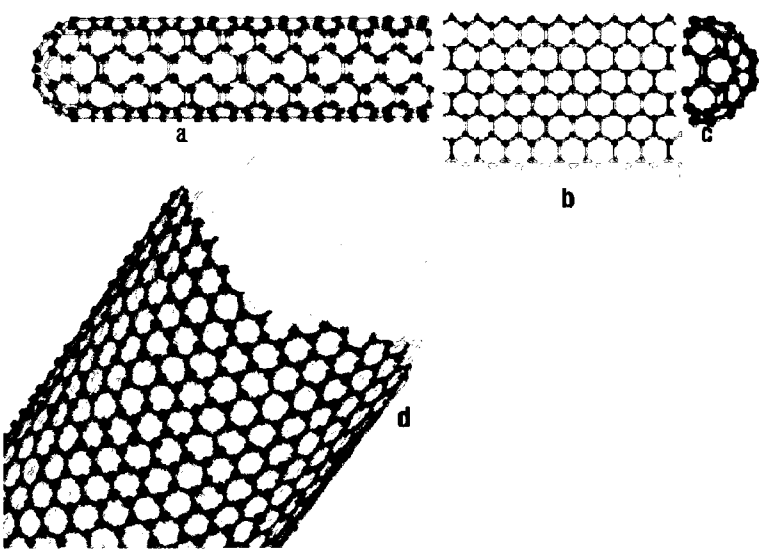

Figure 1.1. Schematics of a SWCNT. a) A (5,5) armchair SWCNT, b) a graphene sheet, and c) a hemispherical end cap. Also shown in d) is a MWCNT. The solid circles in each figure represent the carbon atoms.[11]

Carbon-carbon covalent bonds are among the strongest in nature; therefore it follows that structures based on these bonds form very strong materials. The mechanical properties of CNTs have been studied experimentally and theoretically.[12,13] With a tensile strength of ~100 – 600 GPa, CNTs are about two orders of magnitude stronger than high-strength carbon fibers;[14,15] additionally, the CNT density of 1.3 g/cm^3 is lower than that in commercial carbon fibers (1.8 – 1.9 g/cm^3).[16] The significant reduction of density and volume upon replacement of carbon fibers with CNTs has important implications for aerospace and other high performance composite applications.[17] CNTs also have a high stiffness to weight ratio, with a Young's modulus about 5× higher than carbon fibers.[2,14,18]

CNTs can range from highly conductive metals to semiconductors with a large band gap.[2,19-21] The chirality of the nanotube, or twist, which is described by how a conceptual graphene sheet would be rolled to form the tube, determines whether the CNT behaves as a metal or semiconductor.[22] Metallic CNTs have ballistic transport, meaning there is zero resistance along the tube, and thus can have conductivities several times higher than copper. Because of their very low energy dissipation, CNTs can carry ~10,000× greater current densities than superconducting wires.[23]

1.1.2 Nanocomposites

The unique structural, mechanical,[24] and electronic properties[23,25] possessed by CNTs make them attractive materials as molecular-level

composite reinforcements. Two basic requirements for integrating CNTs into polymer nanocomposites include high dispersibility in the bulk matrix material and having robust interactions with the surrounding host.[11] Strong van der Waals interactions exist between nanotubes, especially SWCNTs, which cause them to form bundles 10 – 100 nm in diameter that must be overcome in order to achieve good dispersion throughout a matrix. In some cases, CNTs can become de-agglomerated via ultrasonication in aqueous surfactant or organic solvent solutions; however, this can introduce defects in the sidewalls that disrupt their electronic properties and mechanical strength, although the defects are minimal. The major hurdle in this method is scaling the process. Another method for debundling, solubilizing, and improving matrix interactions of CNTs is by covalent and non-covalent functionalization. Covalent chemical functionalization introduces new chemical bonds between outside functional groups and some part of the nanotube.[26] This can be achieved by removing the CNT end caps and functionalizing the open ends, or by utilizing one of many methods that directly functionalize the sidewalls. It is important to note that CNT sidewall functionalization depends strongly on the tube diameter – the smaller the diameter, the more strain is present in the system, which leads to more highly reactive sidewalls. MWCNTs possess a much larger diameter than SWCNTs and are more difficult to sidewall functionalize and disperse in common solvents. Other than harsh acid-based etching, most of the reported methods for MWCNT dispersion involve endwall or defect site modifications[27] until the reductive alkylation or arylation sidewall functionalization protocol recently reported, that

results in heavily functionalized MWCNTs that can be solubilized in either water or organic solvents.[28]

Many methods have been developed for covalent sidewall functionalization of SWCNTs including halogenation, hydrogenation, cycloaddition, electrophilic addition, addition of inorganic compounds, ozonolysis, plasma activation, nucleophilic addition, and radical addition.[29-32] While covalent sidewall functionalization improves the solubility of SWCNTs and thus dispersion and cohesion with and throughout polymer matrices, the electronic properties dependent on the conjugated π-system are lost as sp^3 carbons are introduced throughout the sp^2 network. One way to circumvent this loss in conductivity is through the use of noncovalent interactions such as wrapping the SWCNTs with polymers and surfactants.[33,34] It is also important to point out that functionalization of the outer sidewalls of MWCNTs does not result in complete loss of electrical conductivity; electron conduction is still possible throughout the inner, non-functionalized tubes.[28]

1.1.3 Electromagnetic Properties

The study of the electromagnetic wave properties of CNTs in composites is motivated by potential applications in microwave lenses, high-strength low weight electromagnetic interference (EMI) shielding materials, antennas, waveguides, etc.[35-37] Compared to conventional metal-based materials that have historically served these purposes, electrically conductive polymer composites have gained popularity as replacements because of their light weight, resistance

to corrosion, flexibility, and processing advantages.[38] It is thought that ideal polymeric materials for microwave-based applications can be constructed by dispersing small, high aspect ratio conducting cylinders into dielectric polymers; CNTs are therefore good candidates for these systems.[35] For any filler, the EMI shielding effectiveness increases with increasing amount of conducting filler concentration; however there are upper limits to filler concentration because it imparts poor mechanical properties to the composites. Therefore, the goal is to attain optimum properties at the lowest filler loading possible.[39] The permittivity of CNT composites – or the ability to transmit an electric field – is a specific, unitless value inherent in a material used for gauging the effectiveness of a material for radio frequency (RF) applications. It was found that with small addition (~10% or less) of CNTs in a dielectric matrix, the permittivity of the bulk composite increases by a factor of 35.[35,40] This can be attributed to the percolation of the CNTs throughout the matrix leading to effective charge dissipation through the tube network at low loadings.[41] The small size and high aspect ratio of CNTs enable percolation thresholds to be reached with low concentration (<1 wt%) of CNTs.[42,43] Because a nanotube composite's electromagnetic (EM) shielding or absorbing efficiency are dependent on the electronic structure of the CNTs, the bulk properties of composites can be effectively controlled by altering the electronic structure of the tubes, for example via functionalization of the sidewalls.[44]

Another interesting property of CNT interaction with electromagnetic radiation is efficient absorption of radio and microwaves. Upon exposure to

certain MW frequencies (usually 2.45 GHz), CNTs have been shown to undergo intense heating, enabling important applications for processing nanotube-reinforced polymer composites[45] and possibly for the treatment of cancer.[46]

When exposed to a 750 W MW field in air, HiPco[47] SWCNTs ignited and burned. However, when placed under ultra-high vacuum (UHV) in the presence of a MW field, the SWCNTs emitted white light (Figure 1.2).[48] Pyrometer measurements recorded the temperatures of these samples reaching 2000 °C in 5 seconds.[48] This absorption of MW radiation by CNTs may be exploited in materials chemistry to impart crosslinking of a polymer matrix, leading to localized reinforcement and thus improvement in the mechanical properties, especially because this technique is already used to cure thermosetting polymer matrix materials in composites that do not contain CNTs.[45] In addition, the heat produced by the CNTs may also be used as thermal energy to increase curing rates of polymers, effectively acting as internal "nanoheaters" within the matrix.[49] Because of the very efficient conversion of MW radiation to heat, only very low MW power is needed – 50 W or less – especially when the radiation is directly irradiated onto the sample to be cured.

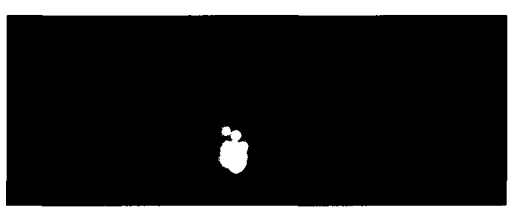

Figure 1.2. SWCNTs in a UHV tube suspended above (~8 cm) an active microwave source, showing the white light emission. Room lights were off.

1.2 Graphene

1.2.1 Properties

Graphene sheets, defined as single atomic layers of carbon sheets with a perfect crystalline lattice, are semimetals that have charge carrying properties that surpass all current materials used in electronics applications.[50,51] Although graphene has been studied theoretically[52] for over 60 years and is integral for describing properties of various carbon-based materials such as CNTs (Figure 1.3), it was presumed not to exist in the free state because it was thermodynamically unstable.[53,54] Nevertheless, theory was proven incorrect in 2004 when graphene was discovered unexpectedly via micromechanical cleavage of bulk graphite.[55] The isolated 2D crystals were found to be both continuous and of high crystal quality.[55-58] Electron mobilities have been recorded up to 200,000 $cm^2/V{\cdot}s$.[59] Furthermore, the flexible yet strong material is an outstanding heat conductor which also makes it interesting for composite applications.[50,60-63] It was found to have a Young's modulus of ~1100 GPa,[64] fracture strength of 125 GPa,[64] thermal conductivity of ~5000 $W/m{\cdot}K$,[65] and an extremely large theoretical specific surface area of 2630 m^2/g.[66] Charge carriers are able to travel thousands of interatomic distances without scattering and demonstrate an ambipolar electric field effect that only weakly depends on temperature.[55-58]

Graphene's electronic properties are dependent on the number of layers, approaching the 3D properties of bulk graphite at ~10 layers.[67] Single and bi-layer graphene are both zero-gap semiconductors, and as the layers increase,

overlap occurs in the conduction and valence bands.[51,55,67] Thus single-, double- and few-layer graphene can be regarded as three different types of 2-D crystals; recently it was shown that these crystals can be identified by distinct Raman signatures.[68,69]

1.2.2 Graphene Production and Applications

Efforts to obtain graphene began before the first confirmed micromechanical exfoliation, or 'Scotch tape' peel-off method in 2004;[55] in fact this method was an extension of earlier work on patterned graphite.[70] Chemical vapor deposition (CVD) and epitaxial growth, such as the decomposition of ethylene on nickel surfaces, were the earliest reported methods for graphene production;[71] recent growth methods include epitaxial growth on electrically insulating surfaces such as SiC.[72-74] Other techniques include thermal expansion of acid or alkali intercalated graphite[75,76] and creation of colloidal graphene suspensions from chemical exfoliation of graphite using strong oxidizing agents to yield graphene oxide (GO).[77]

Applications of graphene are wide-ranging, from use as an additive in polymer composites[60,78] to fabrication of the first room temperature ballistic transistor. As Si-based semiconductor technology is approaching its fundamental limits, graphene is viewed as a promising replacement due to its high mobility, even at high electric-field induced concentrations, and the fact that it does not seem to be affected by chemical doping.[79] Nevertheless, the use of graphene in composite materials will most likely be the first application,

especially since scalable production methods based on colloidal suspensions have already been developed.[60] While the low production costs and high surface area require very low volume percent loading for creation of conductive plastic composites, the mechanical strength will most likely not reach that of its nanotube counterparts due to the much stronger entanglement of CNTs. Other promising applications that can be envisioned for graphene include solid state gas-sensors,[79] spin-valve and superconducting field-effect transistors,[80,81] hydrogen storage materials,[82] energy-storage materials,[66] 'paper-like' materials,[77,83] liquid crystal devices,[84] and mechanical resonators.[85]

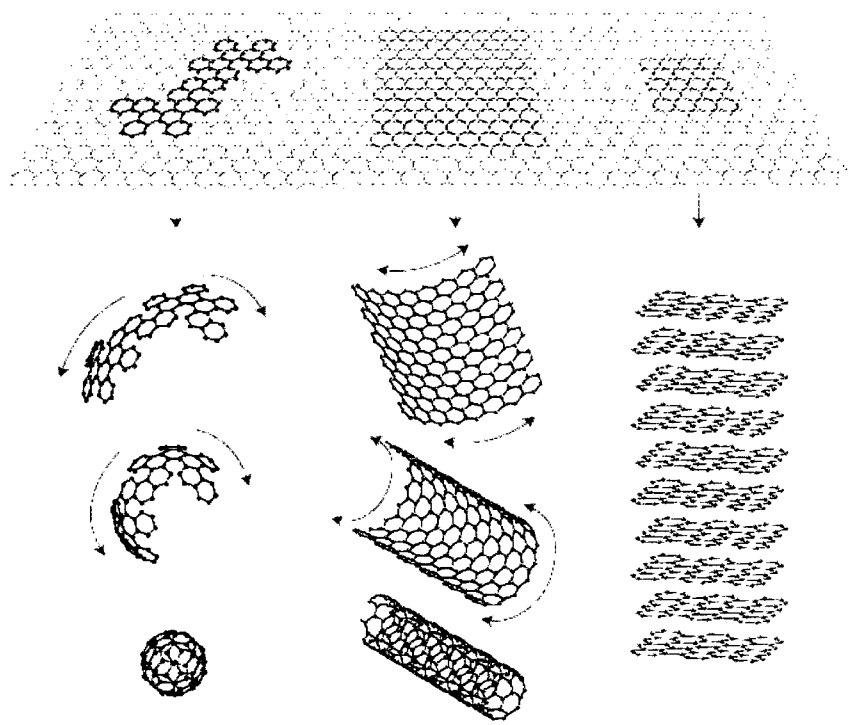

Figure 1.3. Graphene as the mother of all graphitic forms; it is the 2D building material for carbon materials of other dimensionalities – wrapped into 0D buckyballs, rolled into 1D nanotubes, or stacked into 3D graphite.[50]

1.2.3 Chemically Modified Graphene from Graphite Oxide

Graphite oxide (GO) is the product obtained when bulk graphite is exposed to strong oxidizers such as sulfuric acid, nitric acid, potassium chlorate, and potassium permanganate. This oxidation method for producing GO has the highest single sheet yield of the cited protocols with near complete exfoliation of the layers. The most common methods for producing GO are those developed by Brodie,[86] Staudenmaier,[87] and Hummers.[88] Although it was first prepared in the nineteenth century,[86] several models of the exact chemical structure are still being debated in the literature.[89,90] Nevertheless, it has been confirmed that hydrophilic oxygen-containing functional groups including hydroxyl and epoxy groups are introduced on the basal plane surface and edges of the graphene sheets (Figure 1.4).[89] The oxidation prevents stacking via electrostatic repulsion between negatively charged GO sheets[91] and affords easy dispersion in both aqueous and polar organic media. Dispersion of GO sheets in organic solvents is commonly achieved by treatment with isocyanates[89] or long alkyl amines that react with the hydroxyl or acid moieties on the GO, respectively.[92,93] The resulting enhanced processability of GO allows it to be easily incorporated into polymer matrices, and the scalability and low cost of this process makes it attractive for industrial applications.[94]

Because GO as produced is electrically insulating due to the disruption of the graphitic networks caused by the oxidation, chemical or thermal reduction must be employed for partial recovery of the graphite structure. Heating to 200 °C will begin decomposition of the oxygen-containing functional groups, and

rapid heating up to 1050 °C exfoliates and reduces GO to form thermally converted graphene.[95,96] Restoration of electrical conductivity by chemical means can be achieved using reductants such as hydrazine,[97-99] dimethylhydrazine,[60] hydroquinone,[100] and $NaBH_4$.[101,102] Unless polymers or surfactants are present during reduction, or the pH is kept at alkaline conditions,[91] the sheets will reagglomerate; when the agglomerated graphene-based nanosheets are isolated, the dry black powder has an electrical conductivity of ~2×10^2 S/m.[97] Despite the many techniques available for production of GO and its subsequent conversion to chemically modified graphene, the products still contain a significant amount of oxygen and/or defects such as holes. Subsequent thermal annealing of reduced GO does improve the quality to become more graphene-like,[103,104] but this is often performed on surfaces and dispersibility in solvents is no longer possible. Nevertheless, as better understanding is obtained of the chemical structure and reaction mechanisms of chemically modified graphene sheets, better materials can begin to be engineered from these structures by precise control over the chemistry.

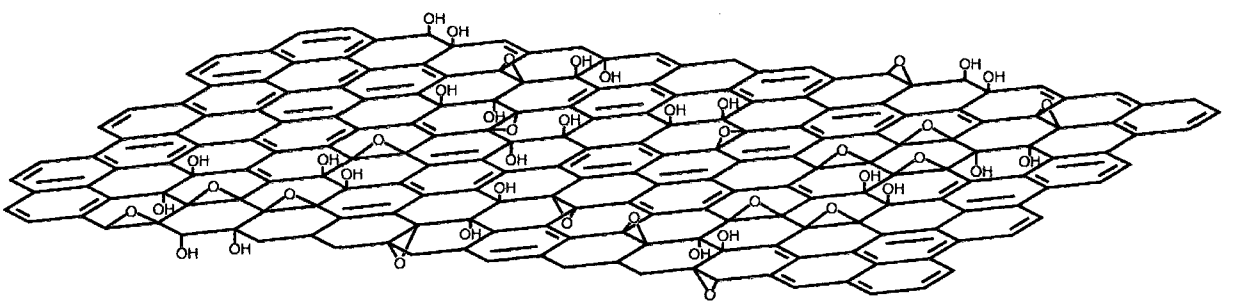

Figure 1.4. Chemical structure of GO.[105] For clarity, minor functional groups, carboxylic groups and carbonyl groups have been omitted at the edges.

1.2.4 Graphene nanoribbons

Graphene, in the form of micron-sized sheets, is a zero-gap semiconductor and cannot be used directly in applications such as field-effect transistors. However, if further confined into thin, elongated strips that possess very straight edges, termed graphene nanoribbons (GNRs), the band gap properties become dependent on the width of the ribbon[106-110] and represent a particularly versatile variety of graphene. When graphene is patterned into a narrow ribbon, the carriers are confined to a quasi-one dimensional system and opening of an energy gap occurs.[107,111] Similar to CNTs, the energy gap depends on the width and crystallographic orientation of the GNR.[110] As shown in Figure 1.5, the band gap decreases as the width of both carbon nanotubes and graphene nanoribbons increases.[112] GNRs exhibit distinct electronic and transport properties as a consequence of the linear energy dispersion relation near the charge neutrality (Dirac) point in the electronic band structure.[109,111,113] Exceptionally high carrier mobility (~25000 to 200000 $cm^2/V \cdot s$) of GNRs has been experimentally and theoretically demonstrated, and is attributed to carrier confinement and coherence.[112] Controlled production of GNRs would circumvent the growth control problems of CNTs and enable the production of GNRs with tunable electronic properties based on width and edge states.

One important difference between CNTs and GNRs is the presence of defined edges in GNRs with localized states that can affect the transport properties of the ribbons. The edge states become increasingly significant as the width of the ribbon decreases, and it is predicted that very narrow GNRs are

needed to achieve the band gap of even large diameter CNTs.[114] The edges of GNRs can, in general, have a combination of armchair or zigzag regions; if a GNR is limited by one type of edge, it is defined as either armchair or zigzag (Figure 1.6). Recent experiments using UHV scanning tunneling microscopy confirmed theory by showing that GNRs with higher fractions of zigzag edges exhibit a smaller energy band gap than a predominantly armchair ribbon of similar width.[115] One example of an important property of GNRs based on edge states was found using periodic *ab-initio* density functional theory (DFT) calculations – zigzag-edge GNRs may become half-metallic when an external electric field is applied across the ribbon.[108,116] A half-metallic material shows a band gap in one spin direction, while the band gap in the other spin direction is zero,[116] and is of great interest in spintronics applications.

Experimentally it was found that zigzag edges in graphene structures are shorter in length, occur less frequently, and thus must be energetically more unstable than that of an armchair edge.[117] This is in agreement with theoretical results that show the stability of an armchair edge is higher than that of a zigzag edge in terms of the total energy.[113] Recently it was reported that Raman spectroscopy can be a useful tool for probing the nature of graphene edges by monitoring the position, width, and intensity of the G and D peaks; the D peak should be zero for an ideal zigzag edge and large for armchair.[118,119]

Methods for producing microscopic quantities of few-layer GNRs include microfabrication on graphite surfaces followed by exfoliation,[110] exfoliation of bulk graphite in the presence of surfactants,[120] or plasma etching of MWCNTs partially

imbedded in a layer of protective polymer.[121] The first method for producing bulk quantities of GNRs was reported through a CVD growth process that resulted in GNRs containing multiple layers of graphene with kinked morphology and highly defective atomic structure.[122] Recently, a high-yielding solution-based bulk method for producing high quality single and few-layer GNRs from MWCNTs via oxidative longitudinal cleavage was reported.[123] Such advances in experimental production of GNRs will lead to realization of applications in composite materials and electronics, and may prove to be more efficient than isolation of graphene sheets.

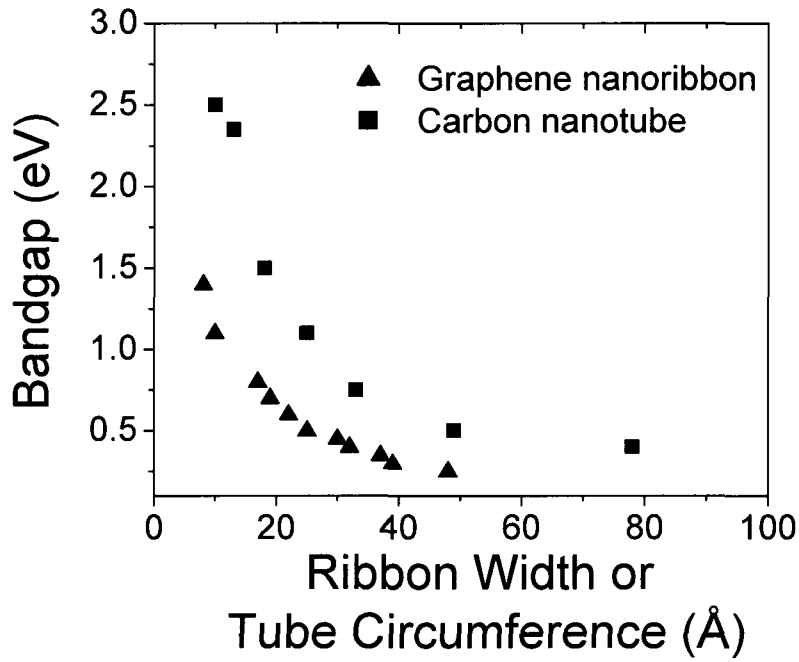

Figure 1.5. The size dependence of the energy gap of carbon nanoribbons and carbon nanotubes is shown. At the same width or circumference, carbon nanoribbons have significantly smaller band gaps than carbon nanotubes.[112]

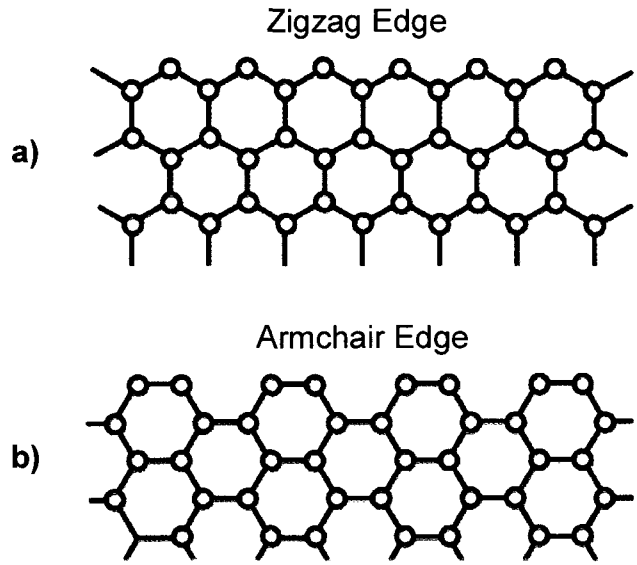

Figure 1.6. Zigzag and armchair edges of graphene. Adapted from Enoki, *et al.*[117]

1.3 References

1. Kroto, H. W.; Heath, J. R.; Obrien, S. C.; Curl, R. F.; Smalley, R. E. *Nature* **1985**, *318*, 162-163.
2. Iijima, S. *Nature* **1991**, *354*, 56-58.
3. Ebbesen, T. W.; Ajayan, P. M. *Nature* **1992**, *358*, 220-222.
4. Seraphin, S.; Zhou, D.; Jiao, J.; Withers, J. C.; Loutfy, R. *Carbon* **1993**, *31*, 685-689.
5. Guo, T.; Nikolaev, P.; Rinzler, A. G.; Tomanek, D.; Colbert, D. T.; Smalley, R. E. *J. Phys. Chem.* **1995**, *99*, 10694-10697.
6. Eklund, P. C.; Pradhan, B. K.; Kim, U. J.; Xiong, Q.; Fischer, J. E.; Friedman, A. D.; Holloway, B. C.; Jordan, K.; Smith, M. W. *Nano Lett.* **2002**, *2*, 561-566.
7. Kong, J.; Cassell, A. M.; Dai, H. J. *Chem. Phys. Lett.* **1998**, *292*, 567-574.
8. Hafner, J. H.; Bronikowski, M. J.; Azamian, B. R.; Nikolaev, P.; Rinzler, A. G.; Colbert, D. T.; Smith, K. A.; Smalley, R. E. *Chem. Phys. Lett.* **1998**, *296*, 195-202.
9. Endo, M. *Chemtech* **1988**, *18*, 568-576.
10. Awasthi, K.; Srivastava, A.; Srivastava, O. N. *J. Nanosci. Nanotechnol.* **2005**, *5*, 1616-1636.
11. Breuer, O.; Sundararaj, U. *Polym. Compos.* **2004**, *25*, 630-645.
12. Qian, D.; Wagner, G. J.; Liu, W. K.; Yu, M.-F.; Ruoff, R. S. *Appl. Mech. Rev.* **2002**, *55*, 495-533.

13. Thostenson, E. T.; Ren, Z.; Chou, T. W. *Compos. Sci. Technol.* **2001**, *61*, 1899-1912.

14. Cooper, C. A.; Ravich, D.; Lips, D.; Mayer, J.; Wagner, H. D. *Compos. Sci. Technol.* **2002**, *62*, 1105-1112.

15. Sennett, M.; Welsh, E.; Wright, J. B.; Li, W. Z.; Wen, J. G.; Ren, Z. F. *Appl. Phys. A: Mater. Sci. Process.* **2003**, *76*, 111-113.

16. Hadjiev, V. G.; Iliev, M. N.; Arepalli, S.; Nikolaev, P.; Files, B. S. *Appl. Phys. Lett.* **2001**, *78*, 3193-3195.

17. Li, F.; Cheng, H. M.; Bai, S.; Su, G.; Dresselhaus, M. S. *Appl. Phys. Lett.* **2000**, *77*, 3161-3163.

18. Bower, C.; Rosen, R.; Jin, L.; Han, J.; Zhou, O. *Appl. Phys. Lett.* **1999**, *74*, 3317-3319.

19. Lau, K. T.; Hui, D. *Compos. Pt. B-Eng.* **2002**, *33*, 263-277.

20. McEuen, P. L.; Fuhrer, M. S.; Park, H. K. *IEEE Trans. Nanotechnol.* **2002**, *1*, 78-85.

21. Avouris, P. *Chem. Phys.* **2002**, *281*, 429-445.

22. Schonenberger, C.; Forro, L. *Phys. World* **2000**, *13*, 37-41.

23. "Carbon Nanotubes: Synthesis, Structure, Properties, and Applications.," Dresselhaus, M. S.; Dresselhaus, G.; Avouris, P.; Editors, Springer-Verlag: Berlin, Germany, 2001.

24. Wong, E. W.; Sheehan, P. E.; Lieber, C. M. *Science (Washington, D. C.)* **1997**, *277*, 1971-1975.

25. Tans, S. J.; Devoret, M. H.; Dal, H.; Thess, A.; Smalley, R. E.; Geerligs, L. J.; Dekker, C. *Nature* **1997**, *386*, 474-477.

26. Sinnott, S. B.; Andrews, R. *Crit. Rev. Solid State Mat. Sci.* **2001**, *26*, 145-249.

27. Lin, Y.; Rao, A. M.; Sadanadan, B.; Kenik, E. A.; Sun, Y.-P. *J. Phys. Chem. B* **2002**, *106*, 1294-1298.

28. Stephenson, J. J.; Sadana, A. K.; Higginbotham, A. L.; Tour, J. M. *Chem. Mater.* **2006**, *18*, 4658-4661.

29. Tasis, D.; Tagmatarchis, N.; Bianco, A.; Prato, M. *Chem. Rev.* **2006**, *106*, 1105-1136.

30. Dyke, C. A.; Tour, J. M. *Nano Lett.* **2003**, *3*, 1215-1218.

31. Bahr, J. L.; Tour, J. M. *Chem. Mater.* **2001**, *13*, 3823-3824.

32. Hudson, J. L.; Casavant, M. J.; Tour, J. M. *J. Am. Chem. Soc.* **2004**, *126*, 11158-11159.

33. Star, A.; Stoddart, J. F.; Steuerman, D.; Diehl, M.; Boukai, A.; Wong, E. W.; Yang, X.; Chung, S.-W.; Choi, H.; Heath, J. R. *Angew. Chem., Int. Ed.* **2001**, *40*, 1721-1725.

34. Moore, V. C.; Strano, M. S.; Haroz, E. H.; Hauge, R. H.; Smalley, R. E.; Schmidt, J.; Talmon, Y. *Nano Lett.* **2003**, *3*, 1379-1382.

35. Grimes, C. A.; Mungle, C.; Kouzoudis, D.; Fang, S.; Eklund, P. C. *Chem. Phys. Lett.* **2000**, *319*, 460-464.

36. Roberts, J. A.; Imholt, T.; Ye, Z.; Dyke, C. A.; Price, D. W., Jr.; Tour, J. M. *J. Appl. Phys.* **2004**, *95*, 4352-4356.

37. Duque, J. G.; Pasquali, M.; Schmidt, H. K. *J. Am. Chem. Soc.* **2008**, *130*, 15340-15347.

38. Li, N.; Huang, Y.; Du, F.; He, X. B.; Lin, X.; Gao, H. J.; Ma, Y. F.; Li, F. F.; Chen, Y. S.; Eklund, P. C. *Nano Lett.* **2006**, *6*, 1141-1145.

39. Yang, Y. L.; Gupta, M. C. *Nano Lett.* **2005**, *5*, 2131-2134.

40. Wu, J. H.; Kong, L. B. *Appl. Phys. Lett.* **2004**, *84*, 4956-4958.

41. Potschke, P.; Dudkin, S. M.; Alig, I. *Polymer* **2003**, *44*, 5023-5030.

42. Nogales, A.; Broza, G.; Roslaniec, Z.; Schulte, K.; Sics, I.; Hsiao, B. S.; Sanz, A.; Garcia-Gutierrez, M. C.; Rueda, D. R.; Domingo, C.; Ezquerra, T. A. *Macromolecules* **2004**, *37*, 7669-7672.

43. Hu, G.; Zhao, C.; Zhang, S.; Yang, M.; Wang, Z. *Polymer* **2006**, *47*, 480-488.

44. Higginbotham, A. L.; Stephenson, J. J.; Smith, R. J.; Killips, D. S.; Kempel, L. C.; Tour, J. M. *J. Phys. Chem. C* **2007**, *111*, 17751-17754.

45. Gibson, R. F.; Ayorinde, E. O.; Wen, Y. F. *Compos. Sci. Technol.* **2007**, *67*, 1-28.

46. Gannon, C. J.; Cherukuri, P.; Yakobson, B. I.; Cognet, L.; Kanzius, J. S.; Kittrell, C.; Weisman, R. B.; Pasquali, M.; Schmidt, H. K.; Smalley, R. E.; Curley, S. A. *Cancer* **2007**, *110*, 2654-2665.

47. Nikolaev, P.; Bronikowski, M. J.; Bradley, R. K.; Rohmund, F.; Colbert, D. T.; Smith, K. A.; Smalley, R. E. *Chem. Phys. Lett.* **1999**, *313*, 91-97.

48. Imholt, T. J.; Dyke, C. A.; Hasslacher, B.; Perez, J. M.; Price, D. W.; Roberts, J. A.; Scott, J. B.; Wadhawan, A.; Ye, Z.; Tour, J. M. *Chem. Mater.* **2003**, *15*, 3969-3970.

49. Higginbotham, A. L.; Moloney, P. G.; Waid, M. C.; Duque, J. G.; Kittrell, C.; Schmidt, H. K.; Stephenson, J. J.; Arepalli, S.; Yowell, L. L.; Tour, J. M. *Compos. Sci. Technol.* **2008**, *68*, 3087-3092.

50. Geim, A. K.; Novoselov, K. S. *Nature Mater.* **2007**, *6*, 183-191.

51. Morozov, S. V.; Novoselov, K. S.; Katsnelson, M. I.; Schedin, F.; Elias, D. C.; Jaszczak, J. A.; Geim, A. K. *Phys. Rev. Lett.* **2008**, *100*.

52. Slonczewski, J. C.; Weiss, P. R. *Phys. Rev.* **1958**, *109*, 272-279.

53. Venables, J. A.; Spiller, G. D. T.; Hanbucken, M. *Rep. Prog. Phys.* **1984**, *47*, 399-459.

54. Evans, J. W.; Thiel, P. A.; Bartelt, M. C. *Surf. Sci. Rep.* **2006**, *61*, 1-128.

55. Novoselov, K. S.; Geim, A. K.; Morozov, S. V.; Jiang, D.; Zhang, Y.; Dubonos, S. V.; Grigorieva, I. V.; Firsov, A. A. *Science* **2004**, *306*, 666-669.

56. Novoselov, K. S.; Jiang, D.; Schedin, F.; Booth, T. J.; Khotkevich, V. V.; Morozov, S. V.; Geim, A. K. *Proc. Natl. Acad. Sci. U. S. A.* **2005**, *102*, 10451-10453.

57. Novoselov, K. S.; Geim, A. K.; Morozov, S. V.; Jiang, D.; Katsnelson, M. I.; Grigorieva, I. V.; Dubonos, S. V.; Firsov, A. A. *Nature* **2005**, *438*, 197-200.

58. Zhang, Y.; Tan, Y.-W.; Stormer, H. L.; Kim, P. *Nature* **2005**, *438*, 201-204.

59. Bolotin, K. I.; Sikes, K. J.; Jiang, Z.; Klima, M.; Fudenberg, G.; Hone, J.; Kim, P.; Stormer, H. L. *Solid State Commun.* **2008**, *146*, 351-355.

60. Stankovich, S.; Dikin, D. A.; Dommett, G. H. B.; Kohlhaas, K. M.; Zimney, E. J.; Stach, E. A.; Piner, R. D.; Nguyen, S. T.; Ruoff, R. S. *Nature* **2006**, *442*, 282-286.

61. Ruoff, R. *Nature Nanotech.* **2008**, *3*, 10-11.

62. Stankovich, S.; Dikin, D. A.; Dommett, G. H. B.; Kohlhaas, K. M.; Zimney, E. J.; Stach, E. A.; Piner, R. D.; Nguyen, S. T.; Ruoff, R. S. *Nature* **2006**, *442*, 282-286.

63. Stankovich, S.; Piner, R. D.; Nguyen, S. T.; Ruoff, R. S. *Carbon* **2006**, *44*, 3342-3347.

64. Lee, C.; Wei, X. D.; Kysar, J. W.; Hone, J. *Science* **2008**, *321*, 385-388.

65. Balandin, A. A.; Ghosh, S.; Bao, W. Z.; Calizo, I.; Teweldebrhan, D.; Miao, F.; Lau, C. N. *Nano Lett.* **2008**, *8*, 902-907.

66. Stoller, M. D.; Park, S. J.; Zhu, Y. W.; An, J. H.; Ruoff, R. S. *Nano Lett.* **2008**, *8*, 3498-3502.

67. Partoens, B.; Peeters, F. M. *Phys. Rev. B* **2006**, *74*, 075404.

68. Ferrari, A. C.; Meyer, J. C.; Scardaci, V.; Casiraghi, C.; Lazzeri, M.; Mauri, F.; Piscanec, S.; Jiang, D.; Novoselov, K. S.; Roth, S.; Geim, A. K. *Phys. Rev. Lett.* **2006**, *97*.

69. Gupta, A.; Chen, G.; Joshi, P.; Tadigadapa, S.; Eklund, P. C. *Nano Lett.* **2006**, *6*, 2667-2673.

70. Lu, X. K.; Yu, M. F.; Huang, H.; Ruoff, R. S. *Nanotechnology* **1999**, *10*, 269-272.

71. Eizenberg, M.; Blakely, J. M. *Surf. Sci.* **1979**, *82*, 228-236.

72. Berger, C.; Song, Z.; Li, T.; Li, X.; Ogbazghi, A. Y.; Feng, R.; Dai, Z.; Marchenkov, A. N.; Conrad, E. H.; First, P. N.; de Heer, W. A. *J. Phys. Chem. B* **2004**, *108*, 19912-19916.

73. Berger, C.; Song, Z.; Li, X.; Wu, X.; Brown, N.; Naud, C.; Mayou, D.; Li, T.; Hass, J.; Marchenkov, A. N.; Conrad, E. H.; First, P. N.; de Heer, W. A. *Science* **2006**, *312*, 1191-1196.

74. Ohta, T.; Bostwick, A.; Seyller, T.; Horn, K.; Rotenberg, E. *Science* **2006**, *313*, 951-954.

75. Chen, G.; Wu, D.; Weng, W.; Wu, C. *Carbon* **2003**, *41*, 619-621.

76. Chung, D. D. L. *J. Mater. Sci.* **2002**, *37*, 1475-1489.

77. Dikin, D. A.; Stankovich, S.; Zimney, E. J.; Piner, R. D.; Dommett, G. H. B.; Evmenenko, G.; Nguyen, S. T.; Ruoff, R. S. *Nature* **2007**, *448*, 457-460.

78. Ramanathan, T.; Abdala, A. A.; Stankovich, S.; Dikin, D. A.; Herrera-Alonso, M.; Piner, R. D.; Adamson, D. H.; Schniepp, H. C.; Chen, X.; Ruoff, R. S.; Nguyen, S. T.; Aksay, I. A.; Prud'homme, R. K.; Brinson, L. C. *Nature Nanotech.* **2008**, *3*, 327-331.

79. Schedin, F.; Geim, A. K.; Morozov, S. V.; Hill, E. W.; Blake, P.; Katsnelson, M. I.; Novoselov, K. S. *Nature Mater.* **2007**, *6*, 652-655.

80. Hill, E. W.; Geim, A. K.; Novoselov, K.; Schedin, F.; Blake, P. *IEEE Trans. Magn.* **2006**, *42*, 2694-2696.

81. Heersche, H. B.; Jarillo-Herrero, P.; Oostinga, J. B.; Vandersypen, L. M. K.; Morpurgo, A. F. *Nature* **2007**, *446*, 56-59.

82. Sofo, J. O.; Chaudhari, A. S.; Barber, G. D. *Phys. Rev. B* **2007**, *75*, 153401.

83. Park, S.; Lee, K. S.; Bozoklu, G.; Cai, W.; Nguyen, S. T.; Ruoff, R. S. *ACS Nano* **2008**, *2*, 572-578.

84. Blake, P.; Brimicombe, P. D.; Nair, R. R.; Booth, T. J.; Jiang, D.; Schedin, F.; Ponomarenko, L. A.; Morozov, S. V.; Gleeson, H. F.; Hill, E. W.; Geim, A. K.; Novoselov, K. S. *Nano Lett.* **2008**, *8*, 1704-1708.

85. Bunch, J. S.; van der Zande, A. M.; Verbridge, S. S.; Frank, I. W.; Tanenbaum, D. M.; Parpia, J. M.; Craighead, H. G.; McEuen, P. L. *Science* **2007**, *315*, 490-493.

86. Brodie, B. C. *Ann. Chim. Phys.* **1860**, *59*, 466-472.

87. Staudenmaier, L. *Ber. Dtsch. Chem. Ges.* **1898**, *31*, 1481-1487.

88. Hummers, W. S., Jr.; Offeman, R. E. *J. Am. Chem. Soc.* **1958**, *80*, 1339.

89. Lerf, A.; He, H.; Forster, M.; Klinowski, J. *J. Phys. Chem. B* **1998**, *102*, 4477-4482.

90. Cai, W. W.; Piner, R. D.; Stadermann, F. J.; Park, S.; Shaibat, M. A.; Ishii, Y.; Yang, D. X.; Velamakanni, A.; An, S. J.; Stoller, M.; An, J. H.; Chen, D. M.; Ruoff, R. S. *Science* **2008**, *321*, 1815-1817.

91. Li, D.; Mueller, M. B.; Gilje, S.; Kaner, R. B.; Wallace, G. G. *Nature Nanotech.* **2008**, *3*, 101-105.

92. Bourlinos, A. B.; Gournis, D.; Petridis, D.; Szabo, T.; Szeri, A.; Dekany, I. *Langmuir* **2003**, *19*, 6050-6055.

93. Niyogi, S.; Bekyarova, E.; Itkis, M. E.; McWilliams, J. L.; Hamon, M. A.; Haddon, R. C. *J. Am. Chem. Soc.* **2006**, *128*, 7720-7721.

94. Steurer, P.; Wissert, R.; Thomann, R.; Mülhaupt, R. *Macromol. Rapid Commun.* **2009**, *30*, 316-327.

95. Schniepp, H. C.; Li, J. L.; McAllister, M. J.; Sai, H.; Herrera-Alonso, M.; Adamson, D. H.; Prud'homme, R. K.; Car, R.; Saville, D. A.; Aksay, I. A. *J. Phys. Chem. B* **2006**, *110*, 8535-8539.

96. McAllister, M. J.; Li, J.-L.; Adamson, D. H.; Schniepp, H. C.; Abdala, A. A.; Liu, J.; Herrera-Alonso, M.; Milius, D. L.; Car, R.; Prud'homme, R. K.; Aksay, I. A. *Chem. Mater.* **2007**, *19*, 4396-4404.

97. Stankovich, S.; Dikin, D. A.; Piner, R. D.; Kohlhaas, K. A.; Kleinhammes, A.; Jia, Y.; Wu, Y.; Nguyen, S. T.; Ruoff, R. S. *Carbon* **2007**, *45*, 1558-1565.

98. Lomeda, J. R.; Doyle, C. D.; Kosynkin, D. V.; Hwang, W.-F.; Tour, J. M. *J. Am. Chem. Soc.* **2008**, *130*, 16201-16206.

99. Tung, V. C.; Allen, M. J.; Yang, Y.; Kaner, R. B. *Nature Nanotech.* **2009**, *4*, 25-29.

100. Wang, G. X.; Yang, J.; Park, J.; Gou, X. L.; Wang, B.; Liu, H.; Yao, J. *J. Phys. Chem. C* **2008**, *112*, 8192-8195.

101. Si, Y.; Samulski, E. T. *Nano Lett.* **2008**, *8*, 1679-1682.

102. Muszynski, R.; Seger, B.; Kamat, P. V. *J. Phys. Chem. C* **2008**, *112*, 5263-5266.

103. Li, X. L.; Zhang, G. Y.; Bai, X. D.; Sun, X. M.; Wang, X. R.; Wang, E.; Dai, H. J. *Nature Nanotech.* **2008**, *3*, 538-542.

104. Jung, I.; Dikin, D.; Park, S.; Cai, W.; Mielke, S. L.; Ruoff, R. S. *J. Phys. Chem. C* **2008**, *112*, 20264-20268.

105. He, H. Y.; Klinowski, J.; Forster, M.; Lerf, A. *Chem. Phys. Lett.* **1998**, *287*, 53-56.

106. Areshkin, D. A.; Gunlycke, D.; White, C. T. *Nano Lett.* **2007**, *7*, 204-210.

107. Nakada, K.; Fujita, M.; Dresselhaus, G.; Dresselhaus, M. S. *Phys. Rev. B: Condens. Matter* **1996**, *54*, 17954-17961.

108. Son, Y.-W.; Cohen, M. L.; Louie, S. G. *Phys. Rev. Lett.* **2006**, *97*, 216803/216801-216803/216804.

109. Barone, V.; Hod, O.; Scuseria, G. E. *Nano Lett.* **2006**, *6*, 2748-2754.

110. Han, M. Y.; Oezyilmaz, B.; Zhang, Y.; Kim, P. *Phys. Rev. Lett.* **2007**, *98*, 206805/206801-206805/206804.

111. Wakabayashi, K.; Fujita, M.; Ajiki, H.; Sigrist, M. *Phys. Rev. B* **1999**, *59*, 8271-8282.

112. Obradovic, B.; Kotlyar, R.; Heinz, F.; Matagne, P.; Rakshit, T.; Giles, M. D.; Stettler, M. A.; Nikonov, D. E. *Appl. Phys. Lett.* **2006**, *88*, 142102/142101-142102/142103.

113. Kawai, T.; Miyamoto, Y.; Sugino, O.; Koga, Y. *Phys. Rev. B* **2000**, *62*, R16349-R16352.

114. Chen, Z.; Lin, Y.-M.; Rooks, M. J.; Avouris, P. *Physica E* **2007**, *40*, 228-232.

115. Ritter, K. A.; Lyding, J. W. *Nature Mater.* **2009**, *8*, 235-242.

116. Son, Y.-W.; Cohen, M. L.; Louie, S. G. *Nature* **2006**, *444*, 347-349.

117. Enoki, T.; Kobayashi, Y.; Fukui, K. I. *Int. Rev. Phys. Chem.* **2007**, *26*, 609-645.

118. Casiraghi, C.; Hartschuh, A.; Qian, H.; Piscanec, S.; Georgi, C.; Fasoli, A.; Novoselov, K. S.; Basko, D. M.; Ferrari, A. C. *Nano Lett.* **2009**, *9*, 1433-1441.

119. Gupta, A. K.; Russin, T. J.; Gutierrez, H. R.; Eklund, P. C. *ACS Nano* **2009**, *3*, 45-52.

120. Li, X.; Wang, X.; Zhang, L.; Lee, S.; Dai, H. *Science* **2008**, *319*, 1229-1232.

121. Jiao, L.; Zhang, L.; Wang, X.; Diankov, G.; Dai, H. *Nature* **2009**, *458*, 877-880.

122. Campos-Delgado, J.; Romo-Herrera, J. M.; Jia, X.; Cullen, D. A.; Muramatsu, H.; Kim, Y. A.; Hayashi, T.; Ren, Z.; Smith, D. J.; Okuno, Y.; Ohba, T.; Kanoh, H.; Kaneko, K.; Endo, M.; Terrones, H.; Dresselhaus, M. S.; Terrones, M. *Nano Lett.* **2008**, *8*, 2773-2778.

123. Kosynkin, D. V.; Higginbotham, A. L.; Sinitskii, A.; Lomeda, J. R.; Dimiev, A.; Price, B. K.; Tour, J. M. *Nature* **2009**, *458*, 872-876.

Chapter 2

Tunable Permittivity of Polymer Composites through Incremental Blending of Raw and Functionalized Single-Walled Carbon Nanotubes

2.1 Introduction

Single-walled carbon nanotubes (SWCNTs) possess desirable properties that can be utilized to form durable, lightweight composite materials for a variety of applications due to their high aspect ratio, mechanical strength,[1] and unique electronic properties.[2] SWCNTs are comprised of an extended network of sp^2 hybridized carbons with a conjugated π-system that results in excellent tube conductivity. Differences in chirality with which a conceptual graphene sheet is rolled to form the nanotube give variations in the band structure, and thus different types of SWCNTs. Three categories of SWCNTs exist in the pristine form – those that are metallic-like with a band gap of 0 eV, semi-metallics with band gaps on the order of meV, and semi-conductors with band gaps varying between 0.8 and 1.4 eV.[3]

SWCNTs have also been shown to be high absorbers of radio and microwaves, implying important telecommunication applications for SWCNT composites.[4,5] The incorporation of SWCNTs into radio frequency (RF) magneto-dielectric materials has great potential in the development of passive RF antenna structures with specific, tunable properties. Though passive structures are not located at the site of an actual active device (i.e. transistors, diodes, amplifiers, etc.), they are nonetheless very important for parameters such as reflection, transmission, phase shifting, and other RF wave controls.

A few desirable characteristics that most passive RF materials strive to exhibit are low electric field loss, wide bandwidth through which interaction can occur, and high ease of fabrication. It is envisioned that these types of materials can be incorporated into an entire antenna system that is constructed by a "layer-by-layer" approach in which the overall observable properties can be fine-tuned through the manipulation of each layer (i.e. source or receiver, circuits, shield, radome, etc.) independently (Figure 2.1).

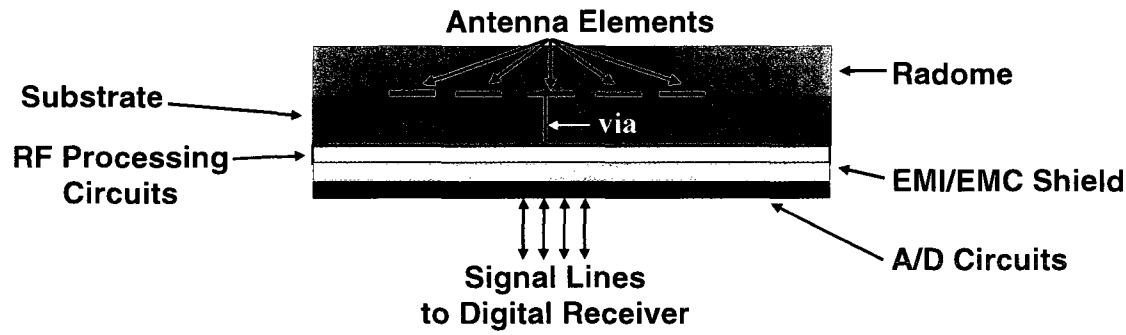

Figure 2.1. An integrated aperture built through a "layer-by-layer" approach in which magneto-dielectric material constructed from SWCNT composites could comprise the radome layer.

The outermost protective layer of an antenna, often referred to as the radome (Figure 2.2) due to its dome-shape, is of great importance because it must protect the antenna from environmental influences while leaving the signal undisturbed. A perfect dielectric wall is ideal, but in reality it is difficult to achieve with the strong, weatherproof nature of the

material that is needed. Thus, a typical goal is to create impedence-matched materials in which the impedence of free space and the material is near equal, resulting in minimum wave interference by the material. Equation 1 shows the relationship between the impedence of free space (Z_o) and the impedence of the material (Z_r) through which the electromagnetic radiation is passed.

$$Z_r = \sqrt{\frac{\mu_r}{\varepsilon_r}} Z_o \qquad (1)$$

Hence, when the permeability (μ) and permittivity (ε) of the desired materials are equal, the impedence-matching requirement can be fulfilled. Therefore, it is these values that must be accurately measured and tailored when devising materials used for constructing passive RF materials. A low permittivity is important to ensure efficient matching of the incident and propagated wave through the material while a maximum permeability is essential to promote rapid attenuation of the wave over a wide range of frequencies. An ideal impedance-matched material will have these two parameters converging to a common value, as close to being equal as possible.

The incorporation of functionalized, magneto-dielectric SWCNTs into polymer composites is thought to not only enhance the strength of the resulting material, but also allow for a wide range of propagation properties and bandwidth access. Through control of both permittivity and permeability in a SWCNT composite, a material can be created that has

high flexibility with variable and flexible conformations, resulting in an extensive variety of possible applications that include radomes as well as patch antennas, resonant and traveling wave antennas, and microwave components such as microstrip lines, filters, and couplers.

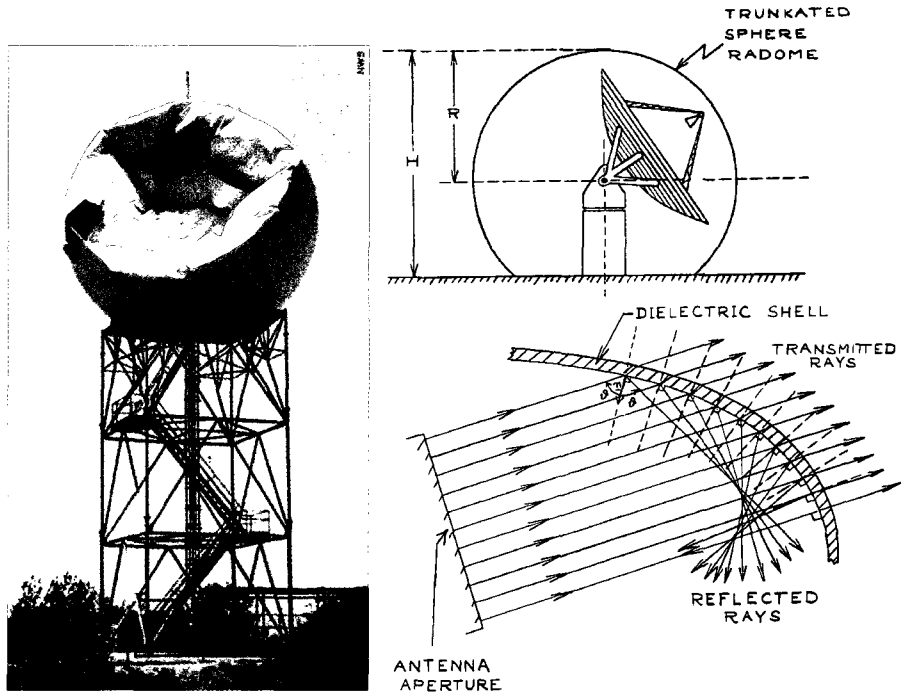

Figure 2.2. (Left): A radome which has been damaged by environmental effects. (Top right): A schematic showing a radome. (Bottom right): Diagram showing reflection and transmission from a radome.[6] SWCNT composites will provide materials that are higher in strength, are more robust, and provide transmission of RF frequency.

Pristine SWCNTs are highly conductive and thus have inherently high permittivity ($\varepsilon > 20$) and absorb radar signals easily. These pristine SWCNTs with high radar signature are not suitable for passive RF materials and need to be modified either through chemical functionalization or through physical blending with other materials with low ε. It is known that functionalizing the sidewalls of SWCNTs disrupts the conjugation of the overall SWCNT and alters its inherent conductivity and electrical properties.[7] Even very light functionalization of tubes, with one functional group in every 100 carbons for example, has been shown to entirely deplete the presence of the metallic-like SWCNTs.[8] Figure 2.3 shows how the functionality control of a SWCNT can be monitored using Raman spectroscopy, specifically the D/G ratio. The D/G ratio is the ratio of peaks arising from the disorder mode (D-band) and the graphite mode (G-band), or the sp^3-mode to the sp^2-mode, which determines the level of sidewall disruption, or functionalization. As more functional groups are attached to the sidewall of a SWCNT, the intensity of the D band increases relative to that of the G band.

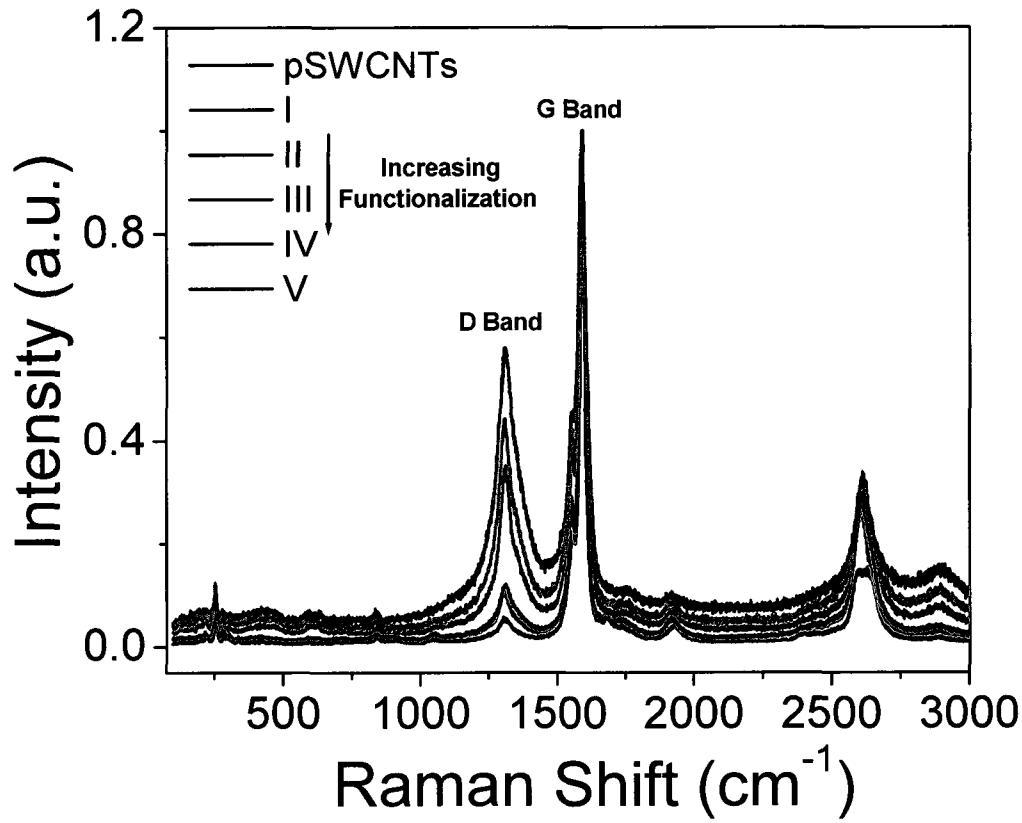

Figure 2.3. Raman spectroscopy (633 nm excitation) of SWCNTs functionalized to varying degrees, as demonstrated by the increasing intensity of the D band.

A method is presented for controlling the permittivity between the values of 20 and 3 (for the real component) over a range of 1 to 1000 MHz in a SWCNT elastomer composite, containing only 0.5 wt% SWCNTs, based on the ratio of raw to functionalized SWCNTs (f-SWCNTs) that are incorporated. The functionalization process is shown in Scheme 2.1. It is expected that the bulk permittivity of samples which contain f-SWCNTs

will be considerably lower than samples that contain only raw SWCNTs. By simply blending the two types of nanotubes (f-SWCNTs and raw SWCNTs) together into the same matrix at varying ratios, the real permittivity (ε_r) of the resulting composite can be tuned to any desired value between 20 and 3. Previous methods have shown[9] that the permittivity (500 MHz to 5.5 GHz) of SWCNT polymer composites can be adjusted between 0 and 140 by varying the loading of raw SWCNTs from 0 to 23 wt%, often requiring large weight fractions of nanotubes.

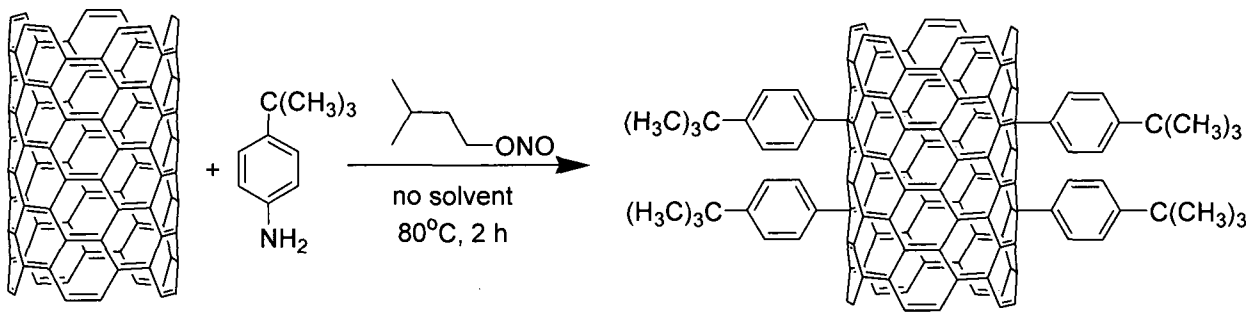

Scheme 2.1. The solvent-free SWCNT functionalization protocol.[10]

2.2 Results and Discussion

In a prior attempt to control the dielectric permittivity of SWCNT composites utilizing functionalization techniques, SWCNTs possessing varying degrees functionalization with *tert*-butylphenyl groups were loaded into single elastomer samples. The degree of functionalization of SWCNTs can easily be controlled when individual SDS-coated SWCNTs in water are functionalized with aryldiazonium salts.[11] By simply adjusting the equivalents of aryldiazonium salt (relative to SWCNT carbon content)

that is added to the aqueous SWCNT solution, the sidewall coverage can be controlled. Raman spectroscopy, thermogravimetric analysis (TGA), and X-ray photoelectron spectroscopy (XPS) all confirm this observation. However, regardless of the degree of functionalization, the measured permittivity did not change from the baseline matrix value of around 3. This reveals that once the SWCNTs become functionalized, the permittivity of the composites is rapidly diminished regardless of the degree of coverage of the SWCNT sidewalls.

When the above technique failed to control the overall permittivity of SWCNT-loaded elastomer samples, the method of blending different ratios of raw to f-SWCNTs (which were all functionalized to roughly the same degree as shown in Scheme 2.1) was attempted. The success of the experiment can be seen in Figures 2.4 and 2.5, which compare the real and imaginary permittivities, respectively, taken from 1 to 1000 MHz, of varying ratios of raw to f-SWCNTs loaded at a total of 0.5 wt% (relative to the elastomer). It is clear that the real values at 1000 MHz can be tuned between about 20 and 3.3 while the imaginary values fluctuate between 14 and 0 (that is from a very lossy material to a loss-less material). As expected, the composite containing only raw SWCNTs displays the highest permittivity, which can subsequently be lowered as a greater amount of f-SWCNTs are incorporated. Figure 2.6 illustrates the observed loss tangent, or the ratio of the imaginary to real permittivity, from 1 to 1000 MHz. For all ratios of raw to f-SWCNTs, the magnitude of

the loss tangent at 1000 MHz remains very close to zero. Table 2.1 compares the magnitude of the real and imaginary permittivity at 1000 MHz, as well as the value of the loss tangent, as the raw to f-SWCNT ratio is varied. Several different ratios that fall between 0.5% raw, 0.25% raw and 0.25% functionalized, and 0.5% f-SWCNTs were tested to arrive at varying values of permittivity. It is important to keep in mind, however, that while the observed trends are highly reproducible, the reported values of permittivity are not entirely absolute. The properties of functionalized SWCNTs will vary on a batch-to-batch basis due to inhomogeneities in the bulk functionalization of the sample as well as with slight differences in the overall degree of functionalization of the tubes. Therefore, if samples are prepared with functionalized SWCNTs from the same batch, they will follow the disclosed trend nicely although the actual permittivity values may be slightly different from those reported here. This is a problem that will be circumvented when the SWCNT functionalization process is commercialized and carried out on a large scale. Even still, this method is a particularly attractive alternative to previously disclosed methods[9] which must increase the weight percentage of SWCNTs up to 23% in order to control the bulk composite dielectric permittivity, and can furthermore suffer from percolation of the highly conductive tubes while affecting the mechanical properties of the composite at those higher loadings.

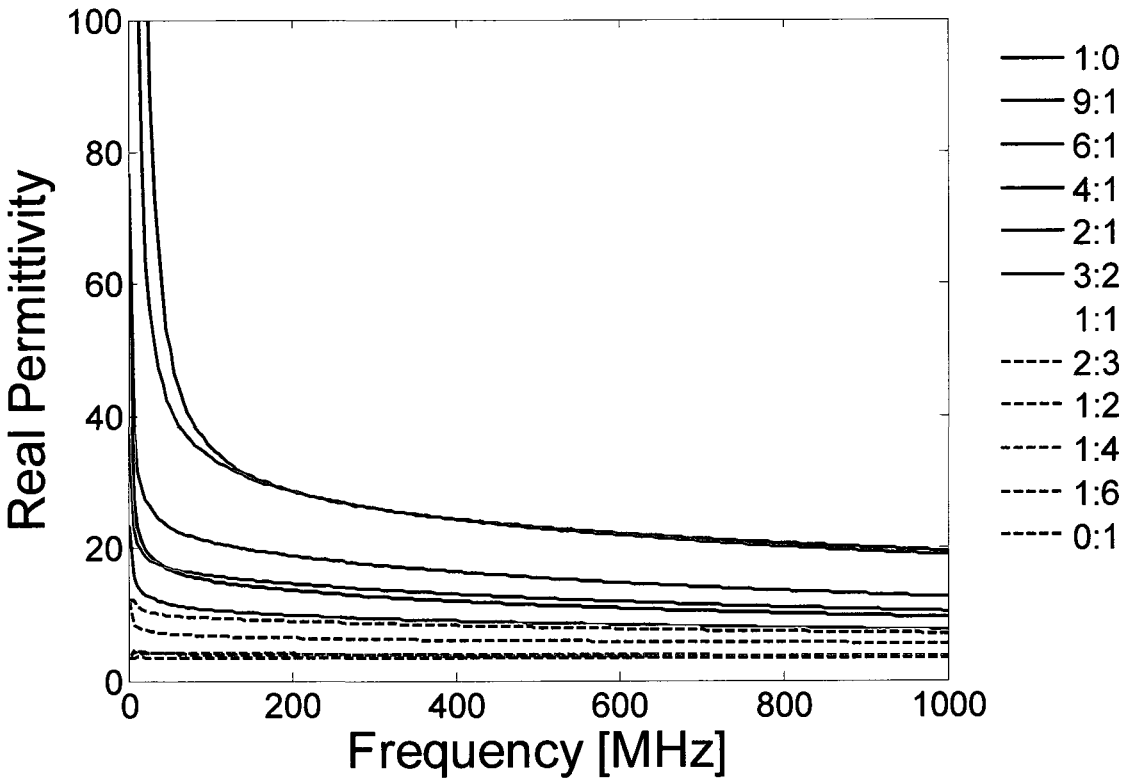

Figure 2.4. The real measured permittivity from 1 to 1000 MHz of 0.5 wt% SWCNT-loaded elastomer composites. Varying ratios of raw:f-SWCNTs are compared in the legend to the right.

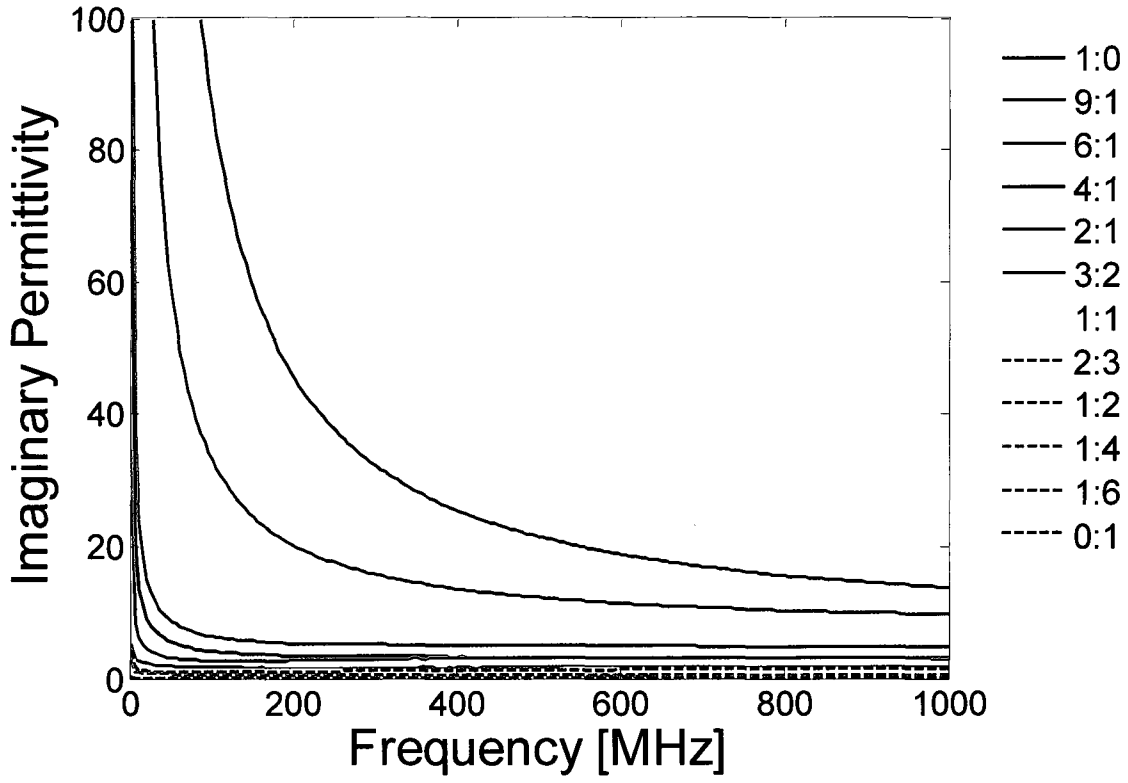

Figure 2.5. The imaginary permittivity from 1 to 1000 MHz of 0.5 wt% SWCNT-loaded elastomer composites. Varying ratios of raw:f-SWCNTs are compared in the legend to the right.

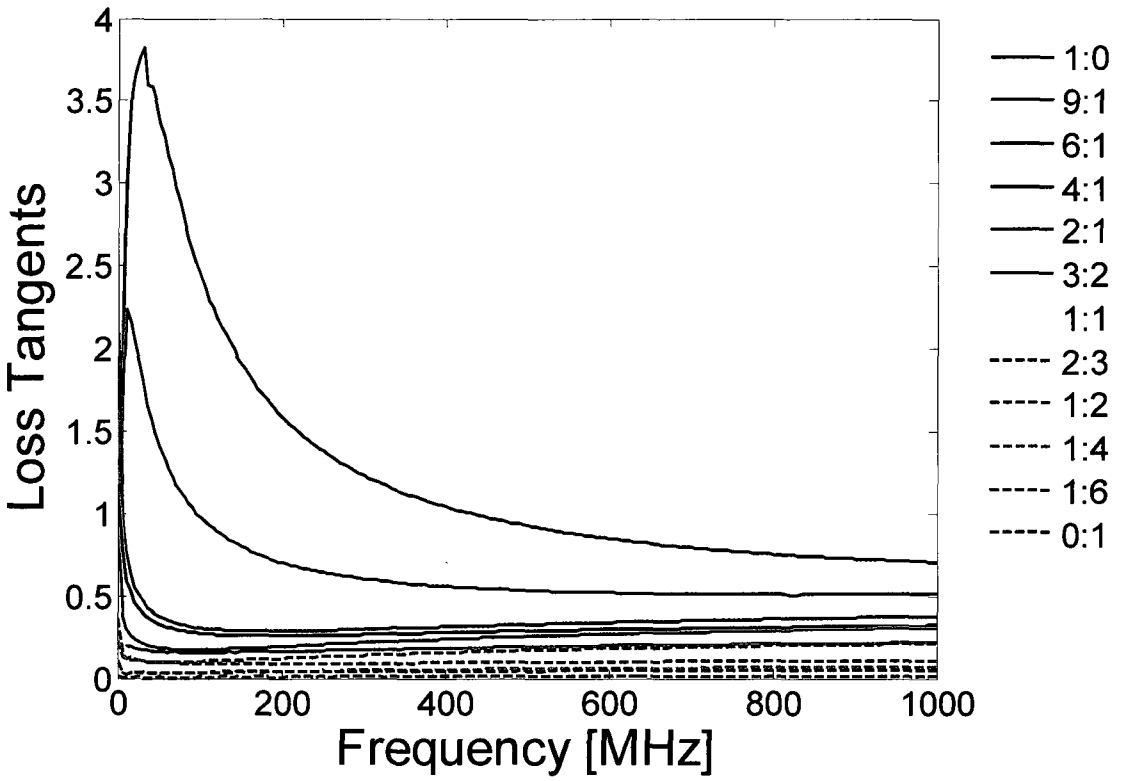

Figure 2.6. The loss tangents of the permittivity from 1 to 1000 MHz of 0.5 wt% SWCNT-loaded elastomer composites. Varying ratios of raw:f-SWCNTs are compared in the legend to the right.

Raw:Functionalized SWCNTs	Real Permittivity	Imaginary Permittivity	Permittivity Loss Tangent
1:0	19.73	14.14	0.71
9:1	19.17	9.91	0.52
6:1	12.64	4.75	0.38
4:1	9.50	3.03	0.32
2:1	7.64	1.71	0.22
1:1	7.32	1.46	0.31
2:3	6.92	1.43	0.21
1:2	5.61	0.63	0.11
1:4	3.70	0.27	0.07
1:6	3.61	0.20	0.05
0:1	3.37	0.05	0.02

Table 2.1. Real and imaginary permittivities, as well as the loss tangent, are compared for varying ratios of raw:f-SWCNTs at 1000 MHz.

2.3. Conclusions

The ability to control the dielectric permittivity of a polymer composite blend incorporating single-wall carbon nanotubes, based on the amount of raw to f-SWCNTs, is disclosed. The magnitude of the real permittivity could to be tuned between 20 and 3.3 with only a 0.5 wt% loading of nanotubes. A number of different incremental ratios of raw to f-SWCNTs were tested. Incorporating a greater amount of raw SWCNTs leads to a higher observed permittivity while including more f-SWCNTs decreases the overall observed permittivity to a predictable degree based on the ratio. In all samples, the loss tangent was very close to zero at 1000 MHz. This type of control over the observed electronic properties of a composite with such a low incorporation of SWCNTs could have

applications in a variety of radio-frequency applications such as radar and antenna devices.

2.4 Experimental

SWCNT composites were formed in a two-part silicone elastomer matrix (NuSil Technology, R-2615). The f-SWCNTs were prepared via a previously published procedure[10] under solvent-free conditions. Raw HiPco-produced[12] SWCNTs were functionalized using 4-*tert*-butylaniline (2.5 equiv to SWCNT carbon) in excess isoamyl nitrite. The reaction components were heated to reflux at 80 °C for 2 h. Upon completion, the resulting SWCNT paste was diluted with 25 mL of acetone and filtered through a PTFE (0.45 μm) membrane. The solid was washed with acetone until the filtrate became colorless. Dispersion of the product in DMF via bath sonication (Cole Parmer ultrasonic cleaner, Model 08849-00) followed by filtration through a PTFE membrane with subsequent acetone washes afforded the final functionalized nanotubes (f-SWCNTs). The mass of the final yield and the TGA reveals, to a rough estimate, the degree of functional group coverage on the SWCNT sidewalls.[11]

The unfunctionalized HiPco SWCNTs were blended in raw form, without purification, directly into the elastomer. The general procedure for making the composite samples is to first disperse 12 mg total carbon weight of SWCNTs (raw, functionalized, or both) into a minimum amount of chloroform by bath sonication. The carbon weight of f-SWCNTs is

determined based on the amount of TGA weight loss observed in a given sample; for example, a 16 mg batch of f-SWCNTs that loses 25 wt% in the TGA is said to possess 12 mg of SWCNT carbon. After NuSil Part A elastomer (2.36 g) is separately dissolved into a minimum amount of chloroform, the two chloroform mixtures are combined and the solvent then evaporated by applying a stream of air (fume hood; efficient ventilation is essential). The mixture is then heated at 60 °C for 2 h in a vacuum oven to remove any remaining solvent before the NuSil Part B (10 wt% of Part A, 0.24 g) is added and mixed with a spatula. The mixture is then poured into an appropriately shaped mold to create samples that fit the dielectric insert for an Agilent E4991A RF Impedance/Material Analyzer (Figure 2.7a). In this case, a stainless steel two-piece mold with a circular cut-out 20 mm in diameter and 2 mm deep was used. The uncured sample, once placed in the bottom half of the mold, was evacuated in a vacuum desiccator (0.5 mm Hg) for 1 h in order to eliminate any trapped air or residual solvent. The top of the mold was then placed on the sample and it was then thermally cured at 200 °C in a drying oven for 2 h before being carefully stripped from the mold (Figure 2.7d). The permittivity of the sample is calculated from the capacitance measured on the impedance analyzer. Five scans from 1 to 1000 MHz were recorded on each sample and the average values are reported here.

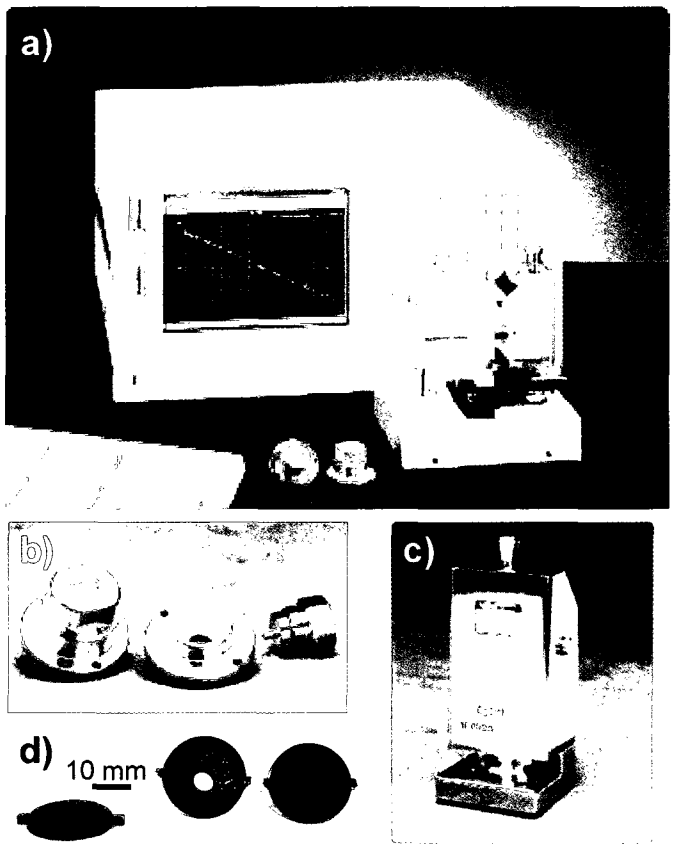

Figure 2.7. a) Instrument used to measure the permittivity of polymer samples - Agilent E4991 RF impedance/material analyzer located at Michigan State University (Prof. Leo Kempel). The instrument is capable of testing both permeability with a magnetic material test fixture (b) and permittivity with the dielectric material fixture (c). Shown in (d) are SWCNT-containing elastomer samples prepared to fit in the test fixtures.

2.5 References

1. Wong, E. W.; Sheehan, P. E.; Lieber, C. M. *Science* **1997**, *277*, 1971-1975.
2. Tans, S. J.; Devoret, M. H.; Dal, H.; Thess, A.; Smalley, R. E.; Geerligs, L. J.; Dekker, C. *Nature* **1997**, *386*, 474-477.
3. O'Connell, M. J.; Bachilo, S. M.; Huffman, C. B.; Moore, V. C.; Strano, M. S.; Haroz, E. H.; Rialon, K. L.; Boul, P. J.; Noon, W. H.; Kittrell, C.; Ma, J.; Hauge, R. H.; Weisman, R. B.; Smalley, R. E. *Science* **2002**, *297*, 593-596.
4. Imholt, T. J.; Dyke, C. A.; Hasslacher, B.; Perez, J. M.; Price, D. W.; Roberts, J. A.; Scott, J. B.; Wadhawan, A.; Ye, Z.; Tour, J. M. *Chem. Mater.* **2003**, *15*, 3969-3970.
5. Roberts, J. A.; Imholt, T.; Ye, Z.; Dyke, C. A.; Price, D. W., Jr.; Tour, J. M. *J. Appl. Phys.* **2004**, *95*, 4352-4356.
6. "Understanding Antennas for Radar, Communications, and Avionics," Rulf, B.; Robertshaw, G. A., Van Nostrand Reinhold Company, Inc.: New York, 1987.
7. Bahr, J. L.; Tour, J. M. *J. Mater. Chem.* **2002**, *12*, 1952-1958.
8. Dyke, C. A.; Stewart, M. P.; Tour, J. M. *J. Am. Chem. Soc.* **2005**, *127*, 4497-4509.
9. Grimes, C. A.; Mungle, C.; Kouzoudis, D.; Fang, S.; Eklund, P. C. *Chem. Phys. Lett.* **2000**, *319*, 460-464.
10. Dyke, C. A.; Tour, J. M. *J. Am. Chem. Soc.* **2003**, *125*, 1156-1157.

11. Dyke, C. A.; Tour, J. M. *Nano Lett.* **2003**, *3*, 1215-1218.

12. Nikolaev, P.; Bronikowski, M. J.; Bradley, R. K.; Rohmund, F.; Colbert, D. T.; Smith, K. A.; Smalley, R. E. *Chem. Phys. Lett.* **1999**, *313*, 91-97.

2.6 Experimental Contributions

My contribution to the experimental work in this chapter is the following: experimental design and preparation of the composites, including SWCNT functionalization. Assistance in composite preparation was received from Ramsey J. Smith. Daniel S. Killips (Michigan State University) performed the permittivity testing of the composites.

Chapter 3

Carbon Nanotube Composite Curing Through Absorption of Microwave Radiation

3.1 Introduction

Polymer curing is the process of polymerization or cross-linking in order to form a matrix. It is often initiated and carried out through thermal photo-induced heating. The use of microwave irradiation to promote polymer curing has been actively explored.[1-3] Microwave-initiated curing is effective and has gained popularity since studies have shown that the strength and integrity of the final composite after curing with microwaves is comparable, if not better, to similar samples that were cured thermally.[4,5] In addition, microwave curing can produce interactions at the molecular level, resulting in faster cure times as well as uniform heating throughout the sample. This high heating efficiency results in shortened total time of processing which leads to lower production costs. Moreover, remote repair, where access to furnaces is prohibitive, could be aided by a method to easily access high temperature (~1000 °C) conditions.

Recently, it has been shown that single-walled carbon nanotubes (SWCNTs)[6] and multi-walled carbon nanotubes (MWCNTs)[7] display strong microwave absorbing properties (2.45 GHz, 700 - 800 W) that result in intense heating, outgassing, and light emission.[6] Even though several theories have been offered,[8,9] the mechanism of nanotube-microwave interaction is still not well-understood. It is noted that the metal catalyst particles that remain associated with the carbon nanotubes do not seem to contribute to the observed efficient absorption of microwave radiation and subsequent heating of the carbon nanotube materials.[10]

This chapter demonstrates how the microwave absorbing properties of various types of carbon nanotubes can be exploited to act as an internal heat source for rapid curing of polymer composites. It is demonstrated that with low microwave power (30 – 40 W) and the addition of a small percentage (< 1.0 wt%) of MWCNTs or SWCNTs, the rapid heating of silicon carbide pre-ceramics occurs with bulk temperatures exceeding 500 °C within 1 min. These composites have promising applications in the aerospace, power materials, and microelectronics industries.[11]

3.2 Results and Discussion

Bulk composite samples of silicon carbide pre-ceramic (SMP-10) with < 1 wt% of MWCNTs, functionalized MWCNTs (f-MWCNTs), raw SWCNTs (r-SWCNTs), and purified SWCNTs (p-SWCNTs) all readily undergo rapid heating when exposed to 30 – 40 W of 2.45 GHz microwave frequency. While the shape of the time-temperature heating curves varies slightly from sample to sample, repeated runs all produce rapid initial heating within the first 1 min (~500 °C) followed by gradual but steady heating exceeding 500 °C within the first 6 min (T_{max} from 550 to 1150 °C, depending on the sample). Due to the rapid heating of the samples and the nature of the SMP-10 matrix, a large amount of outgassing was observed when samples reached 450 °C and above. The outgassing of the sample can be attributed to the nature of the SMP-10 matrix. The pre-ceramic allylhydridopolycarbosilane will decompose and release H_2, CH_4, and C_2H_6 gases, especially at temperatures between 300 – 400 °C.[12] This

resulted in an increase in sample volume due to the formation of pores within the sample as it transformed from a liquid to a solid. Comparatively, samples that were furnace-cured did not expand but are flakey in texture with a grey, ash-like color.

Figure 3.1 shows the heating rates of various loadings of unmodified MWCNTs, all < 1 wt%, under microwave irradiation at 30 – 40 W. As the loading of MWCNTs is increased from 0.1 to 0.75 wt%, the samples heat faster and to higher temperatures. Composites containing 0.75 wt% MWCNTs had the fastest initial heating rate (~500 °C in 10 s) and reached a maximum temperature of ~1150 °C within 6 min (Figure 3.1, red filled circles). It is important to note that this concentration which gives the fastest heating rate corresponds roughly to the electrical percolation threshold for MWCNTs in polymer composites.[13-15] SMP-10 samples that contained 0.5 and 0.1 wt% MWCNTs had a slower initial heating rate, reaching 500 °C in 50 s and plateauing with the temperature stabilization at 692 °C and 628 °C, respectively (Figure 3.1, green filled squares and blue filled triangles). A plateau in the heating curve was not observed for the 0.75 wt% MWCNT sample; the sample continued to slowly heat as it absorbed microwaves over time. This ability is most likely due to the percolation threshold being achieved at this wt% of MWCNTs and thus allows the sample to continue to heat slightly through the more efficient microwave energy to heat conversion. When control samples without nanotubes (SMP-10 alone) were subjected to the same microwave exposure, very minimal heating was observed (111 °C in 5 min) (Figures 3.1 and 3.2, black filled stars). Other control experiments (not shown)

included microwave irradiation of carbon black and graphene SMP-10 composites (0.75 wt%). The samples underwent little heating, and closely resembled the heating curve of the SMP-10-only control shown in Figures 3.1 and 3.2.

In an effort to explore the relationship between nanotube dispersion and microwave heating characteristics, composites were prepared containing f-MWCNTs. It has been shown that the addition of long alkyl chains onto the sidewalls of nanotubes increases the solubility in organic solvents.[16,17] Therefore, f-MWCNTs were prepared with octyl chains covalently attached to the nanotube sidewalls and they were then blended into a SMP-10 composite. Faster rates of heating and higher maximum temperatures might be expected in systems which have a better dispersion of nanotubes throughout the matrix. To test this hypothesis, samples were prepared at a constant loading of 0.75 wt%. To obtain a complete comparison, r-SWCNTs and p-SWCNTs were also evaluated (Figure 3.2). As seen in Figure 3.2, MWCNTs (red filled circles) and r-SWCNTs (pink open squares) display the fastest heating rate in the first 10 s (~500 °C and ~350 °C, respectively) and highest temperature (1150 °C and 768 °C). However, while the f-MWCNTs (Figure 3.2, purple open triangles) and p-SWCNTs (green open circles) did not heat as fast or as high as the MWCNTs and r-SWCNTs, they displayed more effective heating than the control sample (Figure 3.2, black filled stars).

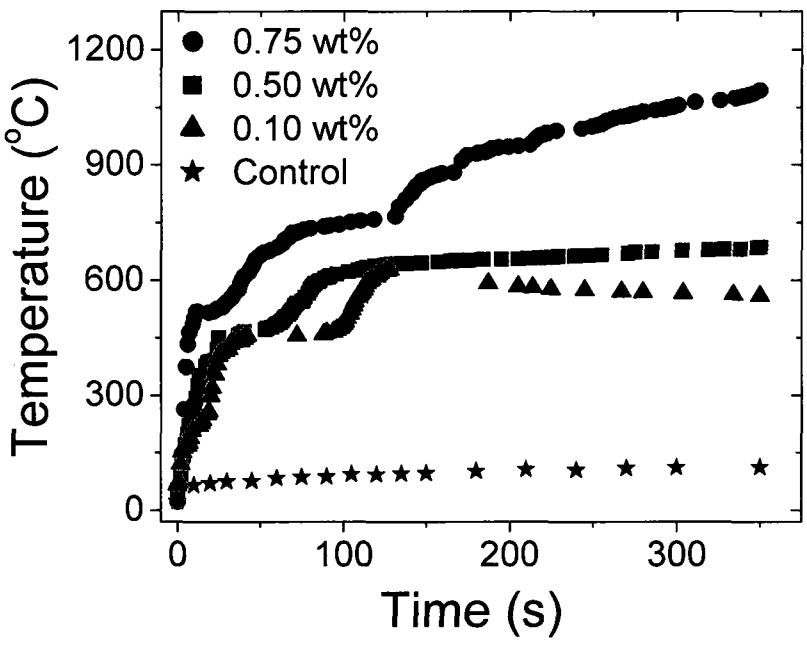

Figure 3.1. Representative microwave heating runs of various wt% loadings of pristine MWCNTs in SMP-10 (30 – 40 W).

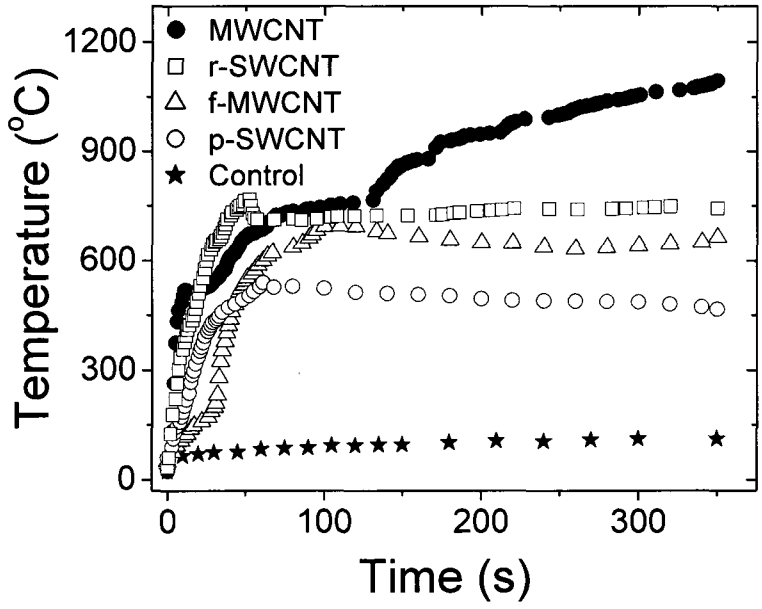

Figure 3.2. Representative runs of 0.75 wt% of each MWCNTs, r-SWCNTs, f-MWCNTs, and p-SWCNTs in SMP-10 (30 – 40 W).

To obtain an estimate of nanotube dispersion before microwave exposure, optical microscope images were obtained on composite samples after removal of the THF. The samples were prepared by placing two drops of uncured nanotube/SMP-10 composite onto a glass microscope slide and then pressing it firmly with another glass slide to create a thin film of the composite between. The samples were then imaged using a polarizing optical microscope (Zeiss Axioplan-2) with representative images shown in Figure 3.3. The degree of dispersion can be qualitatively described by comparing the size of the black aggregates (nanotubes) in the samples and by looking at the overall ratio of white area (SMP-10 matrix only) to nanotubes. Smaller areas of black aggregation and minimal amount of exposed white matrix can be interpreted as better dispersion. It appears that the r-SWCNT sample was the best dispersed, followed by the MWCNT and f-MWCNT samples while the p-SWCNT sample had the poorest dispersion. However, samples with the best dispersion did not necessarily display the best heating ability. Results from current work indicate that it is not dispersion that is the most important variable for microwave heating, but the use of pristine, unmodified tubes as these nanotubes with unperturbed sidewalls likely have a higher microwave cross-sectional absorbance. This is consistent with conductivity studies on functionalized vs. unfunctionalized nanotubes.[17] Nevertheless, good dispersion of an additive throughout the matrix will always lead to enhancement of properties, and the poor dispersion throughout the ceramic matrix is an issue that is currently being addressed. Better dispersion of all the tube types would surely lead to increased

homogeneity in curing throughout the sample, though this may or may not have an effect on the maximum temperature reached by the bulk sample.

In order to assess the degree of curing and composite integrity of the samples after exposure to microwave irradiation, Raman spectroscopy, thermogravimetric analysis (TGA), scanning electron microscopy (SEM), and transmission electron microscopy (TEM) were performed. Note that before analysis, the samples were thoroughly ground into a fine powder and mixed using a mortar and pestle to ensure that all of the properties and images obtained are representative of the bulk sample.

Raman spectroscopy (Renishaw Ramascope, 633 nm diode laser) was used to determine the state of the nanotubes after exposure to microwave radiation. SWCNTs are known to give highly characteristic Raman spectroscopic signatures;[18,19] in particular the radial breathing modes (RBMs)[20] readily identify the presence of SWCNTs as opposed to graphitic structures. However, because of the large difference in size and inherent structure, MWCNTs do not display the characteristic RBM and in general give less intense Raman spectra than SWCNTs. Therefore Raman spectra of MWCNT/SMP-10 composites do not reveal significantly helpful information. The Raman spectra of r-SWCNT/SMP-10 composites before and after microwave exposure (T_{max} = 768 °C), as well as the SMP-10 standard, are given in Figure 3.4. Though the bands are less intense, the presence of the RBMs after microwave exposure (inset) shows that the nanotube structures remain.

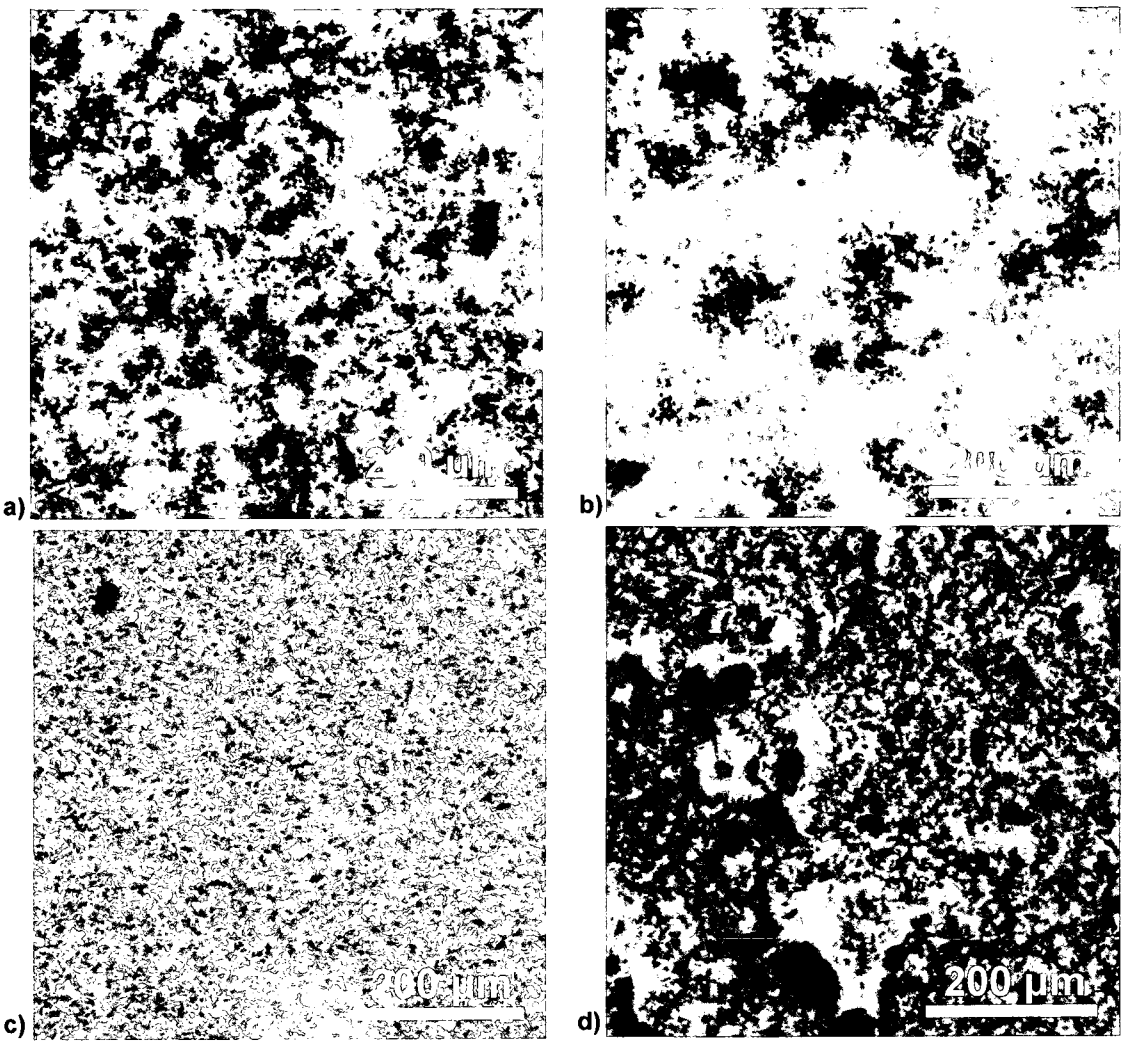

Figure 3.3. Optical microscope images of a) 0.75 wt% MWCNTs b) 0.75 wt% f-MWCNTs c) 0.75 wt% r-SWCNTs and d) 0.75 wt% p-SWCNTs in SMP-10 before microwave exposure.

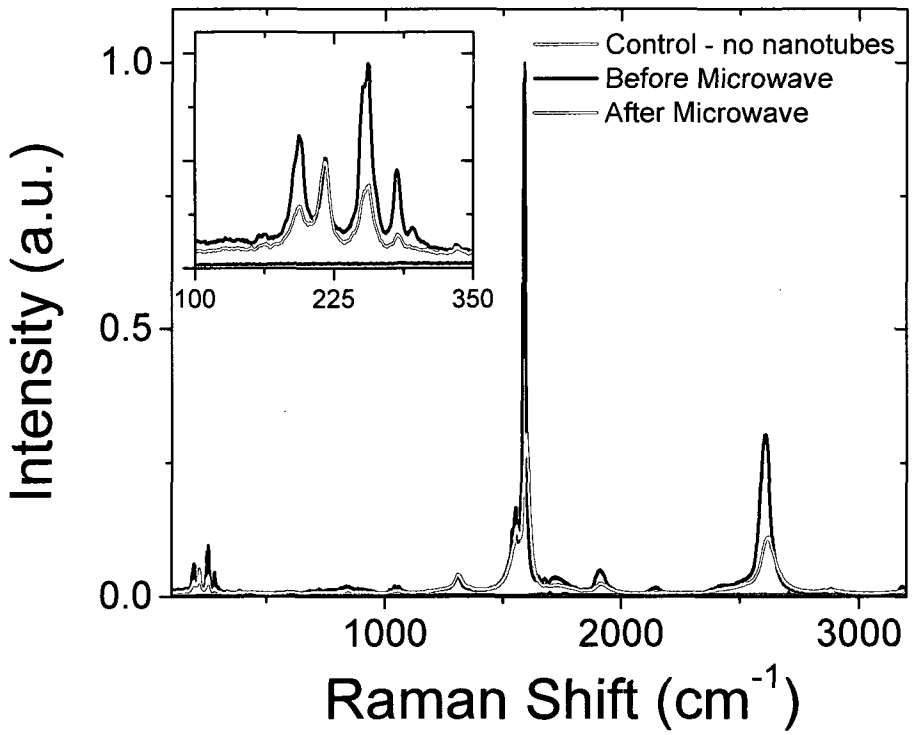

Figure 3.4. Raman spectrum (633 nm excitation) of 0.75 wt% r-SWCNT/SMP-10 composites before (black) and after (red) microwave exposure. The SMP-10-only reference (no nanotubes) is also shown in blue. The inset is an expansion of the radial breathing mode region of the spectrum.

TGA (TA Instruments Q50) measurements were performed on samples after microwave treatment in order to evaluate the extent of curing achieved by the microwave heating. Previous work has shown that examining the mass yields of pre-ceramic and partially formed SiC will indicate the degree to which the polymeric structure has converted to the ceramic phase.[12,21,22] Significant weight loss is categorized by the vaporization of low molecular weight polymers and decomposition with gas evolution (primarily H_2 and CH_4). The TGA samples

were heated at 2 °C/min to 600 °C under an inert argon atmosphere. This was comparable to the standard furnace curing procedure of SMP-10 (1-2 °C/min to 850 °C, hold at 850 °C for 1 h under inert atmosphere). The weight loss curve for uncured SMP-10 served as the control. The control sample had a weight loss of 20% by 300 °C and 31% by 600 °C (Figure 3.5a). In contrast, SMP-10 that has been preheated for ~15 h in a furnace to 850 °C per the curing instructions of the material, and was presumably completely cured, only lost 0.13 wt% by 300 °C and 0.15 wt% by 600 °C (Figure 3.5g). The composite containing 0.75 wt% MWCNTs in SMP-10 had the highest recorded temperature upon microwave treatment (1150 °C) and exhibited the lowest TGA weight loss (2.9 wt% at 600 °C). Figure 3.5a gives a summary of the percent weight loss at 300 °C and 600 °C versus the maximum temperature recorded as the sample was microwave heated. Multiple TGA runs gave consistent weight loss values that varied within 1 wt%. The nanotube composite samples follow the trend of increasing weight loss with decreasing maximum temperatures reached upon microwave treatment. The weight loss is a further indication that the microwave-induced heating of the nanotubes has imparted curing-like behavior of the SMP-10. Figure 3.5b shows a typical weight loss with derivative curve of uncured SMP-10. The two major inflection points centered at 163 °C and 418 °C are highlighted.

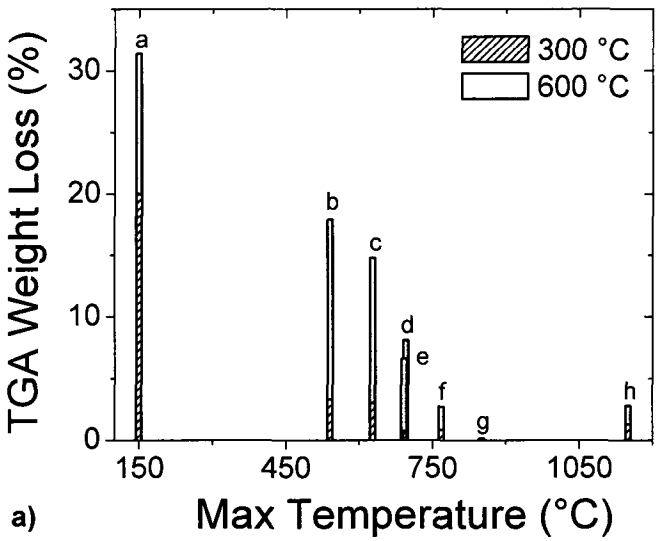

a)

	Sample
a	SMP-10 (uncured)
b	0.75% p-SWCNTs
c	0.10% MWCNTs
d	0.75% f-MWCNTs
e	0.50% MWCNTs
f	0.75% r-SWCNTs
g	SMP-10 (furnace cured to 850 °C)
h	0.75% MWCNTs

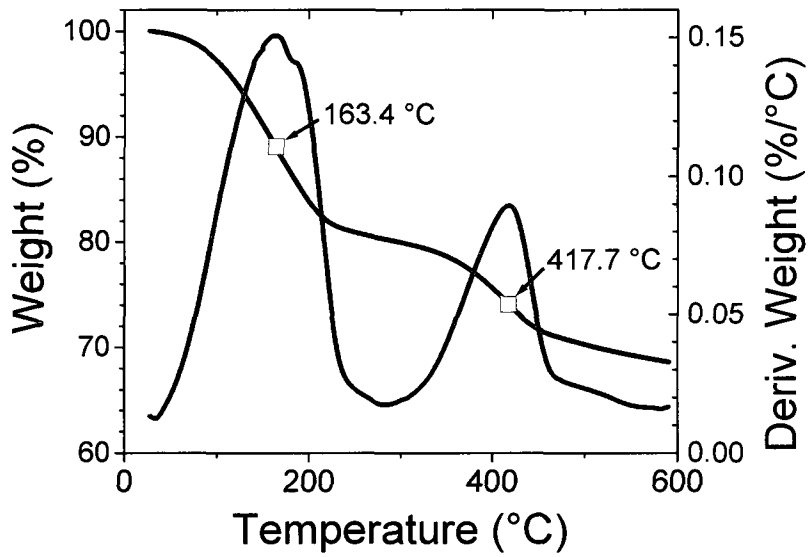

b)

Figure 3.5. a) TGA weight loss percentage of all samples when heated to 300 °C and 600 °C in the TGA apparatus versus the maximum temperature recorded as the samples were treated with microwave irradiation. b) Typical TGA weight loss curve of uncured SMP-10 (sample a, above) with two major points of inflection (11 wt% loss at 163 °C, 26 wt% loss at 417 °C and 31 wt% loss at 600 °C). All experiments were ramped at 2 °C/min under argon.

Representative SEM and TEM images of 0.75 wt% MWCNTs in SMP-10 after microwave treatment are shown in Figures 3.6 and 3.7. These images are also characteristic of what is observed with other MWCNT loadings and tube types as well. Nanotubes were identified in the majority of regions imaged; however, a number of areas scanned did not appear to contain any identifiable nanotubes. This supports the conclusion drawn from optical microscopy that the samples are only marginally dispersed. Even still, the bulk samples were able to undergo a high level of heating which did not appear to be affected by the marginal dispersion. These images also support the hypothesis from Raman spectroscopy that at least a portion of the nanotubes remain intact after microwave treatment. In addition, the images show that the surrounding matrix solidifies around the nanotube as the material cures.

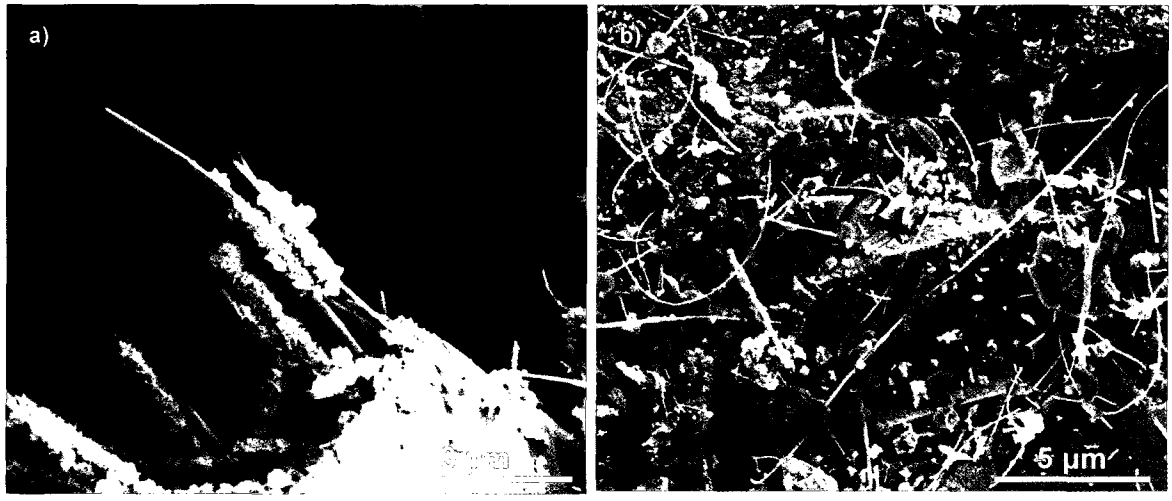

Figure 3.6. SEM images (5.00 kV) of 0.75 wt% MWCNTs in SMP-10 after microwave exposure. The same sample is shown in a) and b), with a close view of the matrix-coated tubes in a) and an overall picture of one face of the SMP-10 matrix in b) that shows MWCNTs protruding from the surface.

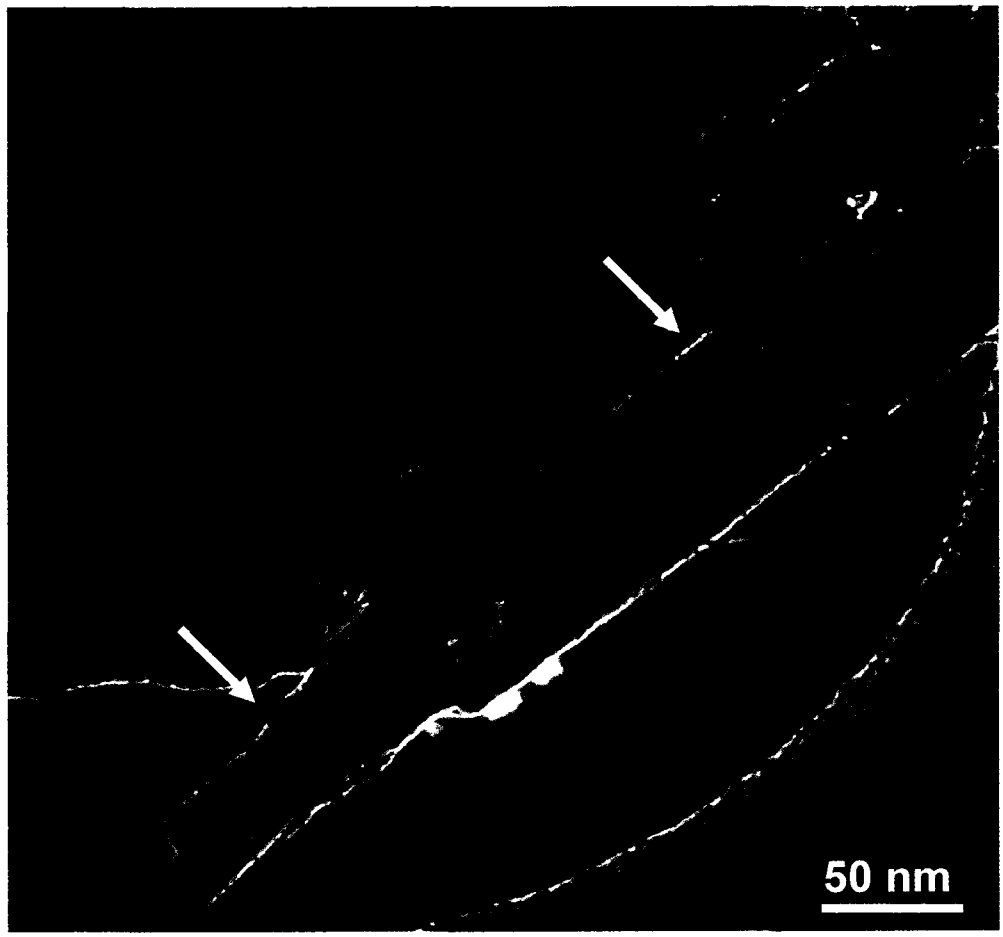

Figure 3.7. TEM image of 0.75 wt% MWCNTs in SMP-10 post-microwave irradiation. The MWCNT (depicted by the arrows) is in close contact with the SMP-10 matrix.

3.3 Conclusions

Microwave irradiation caused pre-ceramic composites containing < 1 wt% nanotubes to heat rapidly, producing products similar to those from much longer thermal curing protocols. The nanotube composites demonstrate very fast initial rates of heating and bulk temperatures reaching 600 °C to 1150 °C within 5 to 7 min with 30 – 40 W of microwave irradiation. Unmodified MWCNTs consistently

produced the best results with the most rapid initial heating (~500 °C in 10 s) and maximum temperatures over 1000 °C within 4 min of exposure. Post microwave analysis of the composites revealed that the nanotubes remain intact, and in close association with the ceramic matrix. TGA experiments showed that the higher the temperature reached when subjected to microwave irradiation, the closer the final composite was to a complete cure. The use of microwave irradiation as a means of curing composites is advantageous over typical thermal methods due to the higher rate of heating and more uniform temperature distribution than can be obtained with internally-produced heat. Microwave heating of carbon nanotube composites can be applied to improving polymer processing by shortening the processing time and thus lowering the production cost and increasing the cure temperatures in composites, especially those related to remote system repair.

3.4 Experimental

The ceramic composites were made by mixing Starfire® SMP-10 (Starfire Systems, Inc.) and the various types of carbon nanotubes (MWCNTs, f-MWCNTs (Figure 3.8), r-SWCNTs, and p-SWCNTs). SMP-10 is a pre-ceramic polysilylene-methylene copolymer that is converted into a silicon carbide ceramic at high temperatures (~850 – 1200 °C). MWCNTs (99.8% carbon purity, Bussan Nanotech Research Institute Inc., a subsidiary of Mitsui & Co., Ltd.) produced using the Endo method[23,24] were used as received. f-MWCNTs functionalized with octyl groups were prepared via the Billups procedure as published

previously[17] (Figure 3.8). SWCNTs were made by the HiPco process[25] at Rice's Carbon Nanotechnology Laboratory and were used in both r-SWCNT and p-SWCNT[26] forms. All other reagents and solvents were used as received from Sigma-Aldrich.

3.4.1 General procedure for preparing nanotube/SMP-10 pre-ceramic composites

The composites were prepared using solvent blending techniques with tetrahydrofuran (THF) by first dispersing 50 mg of nanotubes into 20 mL of THF. This mixture was homogenized for 15 min (IKA® T 25 digital ULTRA-TURRAX® high-performance disperser) at 10,000 rpm, and bath sonicated (Cole Parmer ultrasonic cleaner, Model 08849-00) for 15 min. The SMP-10 was added to the nanotube/THF mixture in amounts necessary to produce the desired nanotube wt%. The mixture was then subjected to 15 min of homogenization followed by 15 min of bath sonication. The solvent was removed by exposing the mixture to an air stream (this must be done in a fume hood; efficient ventilation is essential) for 6 h with intermittent stirring with a spatula every 1 h to ensure that the majority of THF was evaporated. The sample was then transferred to a vacuum oven at 56 Torr and 30 °C for 12 h. The nanotube/SMP-10 composites (1.5 mL) were then loaded into cylindrical quartz test tubes (1 cm diameter x 10 cm height) for exposure to microwave radiation.

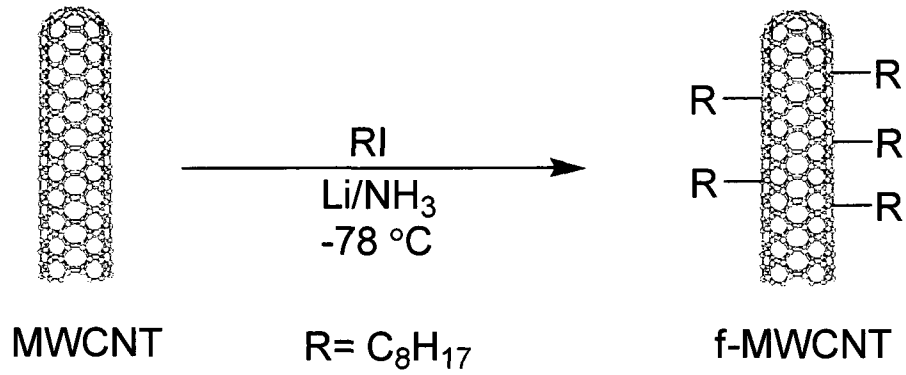

Figure 3.8. The functionalization of raw MWCNTs via reductive alkylation of 1-iodooctane onto the MWCNT sidewalls.[17]

3.4.2 Microwave Setup

A variable power control (10 – 100 W) Opthos microwave generator operating at 2.45 GHz was used in these experiments. The generator was connected via coaxial cable to a waveguide launcher that directs the microwaves onto the sample (Figure 3.9). The nanotube/SMP-10 composites were inserted into the waveguide through a 1 cm hole positioned 10 cm away from the launcher. In all experiments the output power was set to 100 W; however, the forward power was on average 30% greater than the reflected power. Therefore, the actual microwave power that reached the samples was 30 – 40 W, defined as the forward minus reflected power. The unabsorbed microwaves were collected at the distal end of the waveguide by an impedance matched resistive load.

To prevent the ignition of the SMP-10 caused by the rapid heating of the sample, a stream of argon was applied directly onto the surface of the matrix. The temperature of the sample was monitored by inserting a stainless steel thermocouple (K-type, Omega Model KMQSS, ungrounded, 0.032 in diameter)

directly into the sample. The thermocouple was connected to a digital thermometer whose reading was recorded in real-time. Any possible microwave-absorbing properties of the thermocouple were taken into account by measuring the temperature increase recorded (40 – 50 °C) when the thermocouple alone was exposed to microwave radiation in the absence of nanotube-SMP-10 composites.

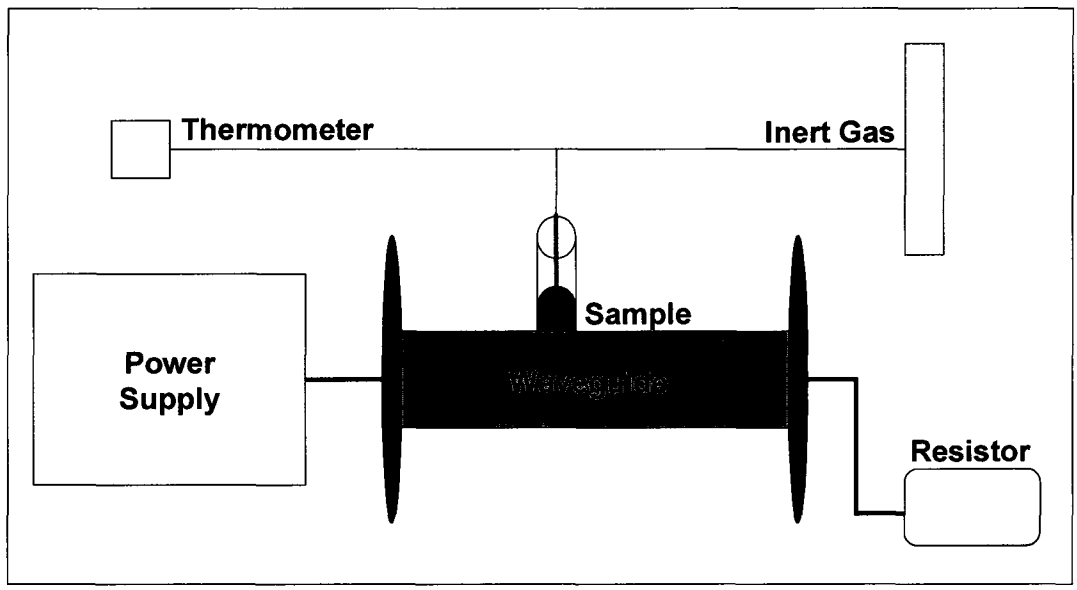

Figure 3.9. Schematic diagram depicting the major components of the microwave setup used.

3.5 References

1. Zhou, S.; Hawley, M. C. *International SAMPE Symposium and Exhibition* **2001**, *46*, 2243-2251.
2. Bai, S. L.; Djafari, V.; Andreani, M.; Francois, D. *Proceedings of the International Conference on Composite Materials and Energy, Montreal, May 8-10, 1995* **1995**, 383-388.
3. Wang, T.; Liu, J. *J. of Electronics Manufacturing* **2000**, *10*, 181-189.
4. Tanrattanakul, V.; Jaroendee, D. *J. Appl. Poly. Sci.* **2006**, *102*, 1059-1070.
5. Chaowasakoo, T.; Sombatsompop, N. *Comp. Sci. and Tech.* **2007**, *67*, 2282-2291.
6. Imholt, T. J.; Dyke, C. A.; Hasslacher, B.; Perez, J. M.; Price, D. W.; Roberts, J. A.; Scott, J. B.; Wadhawan, A.; Ye, Z.; Tour, J. M. *Chem. Mater.* **2003**, *15*, 3969-3970.
7. Wang, C. Y.; Chen, T. H.; Chang, S. C.; Chin, T. S.; Cheng, S. Y. *Appl. Phys. Lett.* **2007**, *90*, 103111-103113.
8. Ye, Z.; Deering, W. D.; Krokhin, A.; Roberts, J. A. *Phys. Rev. B* **2006**, *74*, 075425/075421-075425/075425.
9. Peng, Z.; Peng, J.; Ou, Y. *Phys. Lett. A* **2006**, *359*, 56-60.
10. Anand, A.; Roberts, J. A.; Naab, F.; Dahiya, J. N.; Holland, O. W.; McDaniel, F. D. *Nucl. Instr. and Meth. in Phys. Res. B* **2005**, *241*, 511-516.
11. Macdonald, L. *Ceramic Trans.* **2002**, *144*, 87-95.

12. Puerta, A. R.; Remsen, E. E.; Bradley, M. G.; Sherwood, W.; Sneddon, L. G. *Chem. Mater.* **2003**, *15*, 478-485.

13. Yang, Y.; Gupta, M. C.; Dudley, K. L.; Lawrence, R. W. *J. Nanosci. Nanotechnol.* **2005**, *5*, 927-931.

14. Potschke, P.; Dudkin, S. M.; Alig, I. *Polymer* **2003**, *44*, 5023-5030.

15. Hu, G.; Zhao, C.; Zhang, S.; Yang, M.; Wang, Z. *Polymer* **2006**, *47*, 480-488.

16. Liang, F.; Sadana, A. K.; Peera, A.; Chattopadhyay, J.; Gu, Z.; Hauge, R. H.; Billups, W. E. *Nano Lett.* **2004**, *4*, 1257-1260.

17. Stephenson, J. J.; Sadana, A. K.; Higginbotham, A. L.; Tour, J. M. *Chem. Mater.* **2006**, *18*, 4658-4661.

18. Rao, A. M.; Richter, E.; Bandow, S.; Chase, B.; Eklund, P. C.; Williams, K. A.; Fang, S.; Subbaswamy, K. R.; Menon, M.; Thess, A.; Smalley, R. E.; Dresselhaus, G.; Dresselhaus, M. S. *Science* **1997**, *275*, 187-191.

19. Rao, A. M.; Bandow, S.; Richter, E.; Eklund, P. C. *Thin Solid Films* **1998**, *331*, 141-147.

20. Saito, R.; Takeya, T.; Kimura, T.; Dresselhaus, G.; Dresselhaus, M. S. *Phys. Rev. B* **1998**, *57*, 4145-4153.

21. Nghiem, Q. D.; Pham, A. T.; Kim, D.-P. *Mater. Sci. Forum* **2006**, *510-511*, 774-777.

22. Kotani, M.; Kato, Y.; Kohyama, A.; Narisawa, M. *J. Ceram. Soc. Japan* **2003**, *111*, 300-307.

23. Oberlin, A.; Endo, M.; Koyama, T. *J. Crystal Growth* **1976**, *32*, 335-349.

24. Endo, M. *Chemtech* **1988**, *18*, 568-576.

25. Nikolaev, P.; Bronikowski, M. J.; Bradley, R. K.; Rohmund, F.; Colbert, D. T.; Smith, K. A.; Smalley, R. E. *Chem. Phys. Lett.* **1999**, *313*, 91-97.

26. Chiang, I. W.; Brinson, B. E.; Huang, A. Y.; Willis, P. A.; Bronikowski, M. J.; Margrave, J. L.; Smalley, R. E.; Hauge, R. H. *J. Phys. Chem. B.* **2001**, *105*, 8297-8301.

3.6 Experimental Contributions

My contribution to the experimental work in this chapter is the following: experiment design and preparation of the composites, including SWCNT and MWCNT functionalization. I collected all of the time/temperature heating data and performed optical microscopy, Raman, TGA, SEM, and TEM. Assistance in experimental design and building of MW setup was received from Padraig G. Moloney, Michael C. Waid, Juan G. Duque, Carter Kittrell, and Howard K. Schmidt. Padraig G. Moloney also participated in some time/temperature heating experiments and collected SEM data (not shown).

Chapter 4

Graphite Oxide Flame Retardant Polymer Nanocomposites

4.1 Introduction

Although the prevention and control of fires is an important issue that has been addressed by many researchers, the problem is still prevalent and improvements are needed. It is estimated that each year death tolls related to fires exceed 4000 in the United States and 5000 in Europe, with costs totaling ~1% of the gross domestic product.[1,2] The cause of fires can range between a wide combination of factors including flammability of the generated volatiles, amount of heat released on burning, rate of heat release, ignitability of the material, etc.; therefore, it is critical to develop flame retardant materials that are able to decrease both fire risks and hazards.[1]

Polymers are the class of material often targeted for flammability reduction in product fabrication due to their desirable mechanical, thermal, and electrical properties. Some inherently flame retardant polymers such as poly(vinyl chloride) (PVC) or fluoropolymers may be replaced by a more flammable polymer (such as a non-halogenated polyolefin) due to cost constraints, recycle requirements, or regulations regarding the elimination of certain compounds (such as halogen or heavy metals) in waste electronic equipment, such as in the WEEE and RoHS protocols.[3,4] Alternative methods for decreasing the flammability of polymers without halogenated flame retardants involve the incorporation of additives such as alumina trihydrate and magnesium hydroxide. However, these additives must be used in very large quantities (> 60 wt% for mineral fillers) for flame retarding benefits to be realized, and this often has deleterious effects on the host polymer's mechanical and electrical properties.[1]

Phosphorus-based flame retardant additives are another alternative, but these materials have their limitations as well including cost and plasticizing effect (depending upon structure) on polymer mechanical properties.[5]

Formation of polymer nanocomposites has become a recent solution to improving the flammability of polymers via an additive approach. A nanocomposite in this context can be defined as a two-phase material whose filler is dispersed throughout the polymer on a nanometer scale. A significant advantage of nanoadditives is that they can be used in a much smaller amount (2-10 wt%) than inorganic additives with marked observed improvement in properties including enhanced mechanical properties, solvent resistance, and conductivity.[2,6] Lower filler requirements result in materials that are less expensive and easier to process. Carbon nanoadditives, including graphite and carbon nanotubes, have been extensively explored because of their ability to increase both mechanical strength and electronic conductivity of the native polymer.[7-9] In addition, carbon nanoadditives have begun to be explored for enhancement of the flame retardant properties of various polymer systems. For example, expandable graphite has been used as an intumescent flame retardant in polyisocyanurate-polyurethane foams[10] and high-density rigid polyurethane foams[11] with overall improvement of fire behavior and no worsening of mechanical properties. Incorporation of single-walled carbon nanotubes (SWCNTs) and multi-walled carbon nanotubes (MWCNTs) into polymers have demonstrated a decrease in heat release rate, slower combustion process,

delayed time to ignition, and even enhancement in mechanical properties such as Young's modulus and storage modulus.[12-14]

One other carbon nanoadditive of interest is graphite oxide. Graphite oxide (GO) is the product obtained when bulk graphite is exposed to strong oxidizers such as sulfuric acid, nitric acid, potassium chlorate, or potassium permanganate. These introduce oxygen-containing functional groups, including hydroxyl and epoxy groups;[15] the process is often employed to exfoliate or expand the graphene layers and to impart water solubility. The oxidation prevents graphene stacking and affords easy dispersion in both aqueous and polar organic media. The enhanced processability of GO allows it to be incorporated into polymer matrices, and the scalability and low cost of this process makes it attractive for industrial applications.[16] Chemical or thermal reduction can then be employed for partial recovery of the graphite structure; it has been shown that heating to only 200 °C will begin decomposition of the oxygen-containing functional groups to form thermally converted graphene.[17] The flammability of graphite oxide has been studied in styrene-butyl acrylate and melamine poly(metaphosphate) copolymers; the addition of GO was found to reduce the peak heat release rate by as much as 45% with only 1 wt% GO content.[18,19] Though these results are promising, the use of GO as a nanofiller for reducing the flammability of widely used commodity polymers is still lacking. Here we report the effect of graphite oxide addition into polycarbonate (PC), acrylonitrile butadiene styrene (ABS), and high-impact polystyrene (HIPS) on the mechanical strength and flammability of the resulting nanocomposites.

4.2 Results and Discussion

The nanocomposites of GO were solvent blended with PC, ABS, and HIPS in varying wt%; the resins were chosen because of their use in many engineering plastics applications; PC is inherently somewhat flame retardant due to its ability to form polyaromatics and release CO_2 upon ignition, while ABS and HIPS are considerably more flammable.[20] Therefore, the wide-range of properties between the resins will allow for a broad evaluation of the ability of GO to reduce the flammability of commodity polymers. In order to determine the quality of the composites, the overall morphology and dispersion of GO were studied by scanning electron microscopy (SEM) and optical microscopy. In addition, mechanical properties of the composites were evaluated using dynamic mechanical analysis (DMA); the storage modulus and glass transition temperature (T_g) were measured. To evaluate the thermal properties and flammability of the materials, microcombustion calorimetry (MCC), thermogravimetric analysis (TGA), and vertical open flame testing were performed.

4.2.1 Sample imaging

SEM images (Figure 4.1) taken of the composites at their fracture surface reveal that overall, the GO flakes do not agglomerate into dense regions. GO flakes were present throughout, and no large, noticeable features were found, suggesting good dispersion. The images shown in Figure 4.1 are for HIPS, ABS, and PC composites containing 10 wt% GO. Flakes of GO, several microns in

size, were found protruding from the polymer matrix and are indicated by the white arrows. Optical microscopy supports the SEM data but points to adequate dispersions at the microscale (Figure 4.1, inset) due to the observation of dark regions, presumed to be GO, present in all parts of the sample. Although the concentration of the dark regions is not always evenly distributed, this may be attributed to the manner in which the optical samples were prepared; the polymer samples were heated to the point of softening and flattened on a glass microscope slide before imaging so that the light passing through the sample was maximized. Many regions were completely filled with GO and thus unable to be optically imaged.

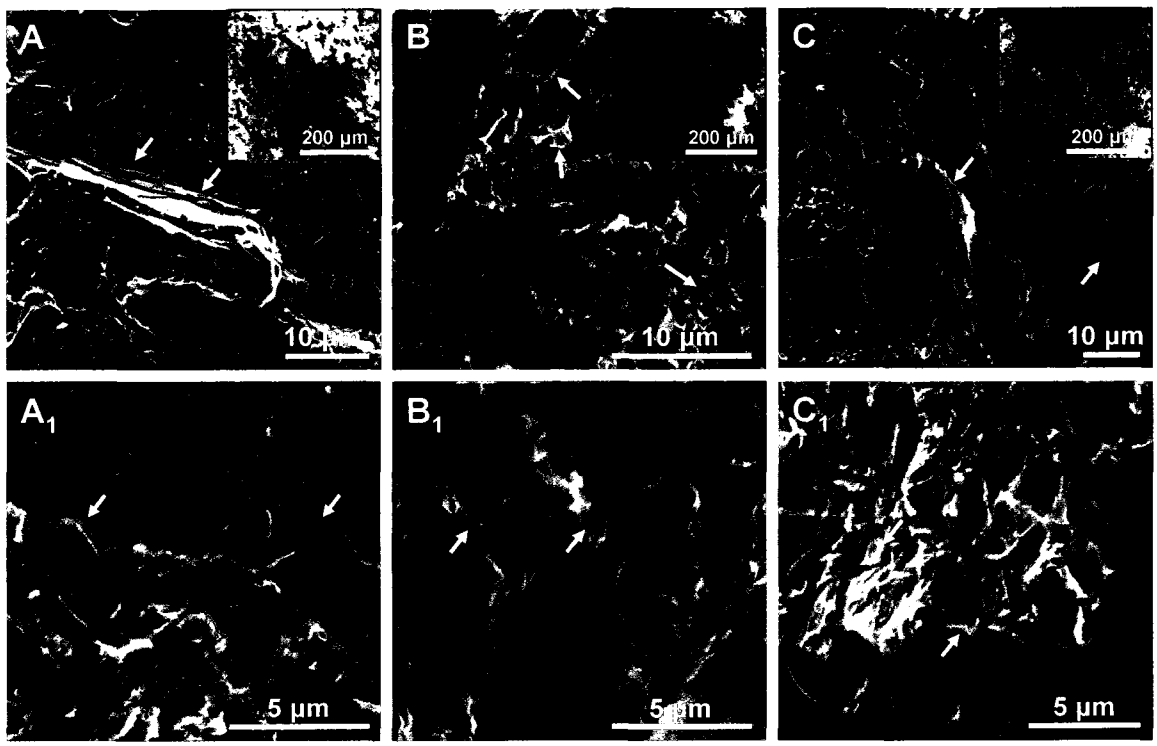

Figure 4.1. SEM and optical microscopy images (inset) of 10 wt% GO loaded in HIPS (A), ABS (B), and PC (C) composites. The bottom row of images shows zoomed-in regions of the sample directly above. White arrows highlight some of the areas which contain GO flakes. For all samples, it is apparent that the GO flakes do not form large agglomerates and are dispersed throughout all sample regions imaged.

4.2.2 Mechanical Properties

To study the effects of GO addition on the mechanical properties of the polymers, the storage modulus of the composites was measured using DMA. Not only is this of interest to determine the physical properties of the material, it may give insight to the flammability properties as well. One recent study has indicated a direct relationship between viscoelastic measurement (storage

modulus) and reduction in heat release rate.[12] A dual cantilever clamp was used on sample bars measuring 1.3 cm wide, 7.6 cm long, and 0.3 cm thick; the samples were heated in air at 3 °C/min to 150 °C (ABS and HIPS) or 180 °C (PC). It was observed with all three polymers that the storage modulus increased with increasing GO content over the entire temperature range (Figure 4.2). Though the increase in strength is not proportional to the amount of GO added, it is apparent that incorporation of the nanofiller did not deteriorate the mechanical properties of the polymer. The most distinct increase in storage moduli with increasing GO content was observed for HIPS, while PC showed only a small increase with 5 wt% and 10 wt% GO samples having almost identical storage modulus across the entire temperature range. The T_g was extrapolated from the storage modulus data and found to not vary significantly with increased GO content. In general, the T_g increased slightly with increasing GO, implying that GO addition increases the stiffness of the composites. The T_g for each sample is given in the inset of Figure 4.2.

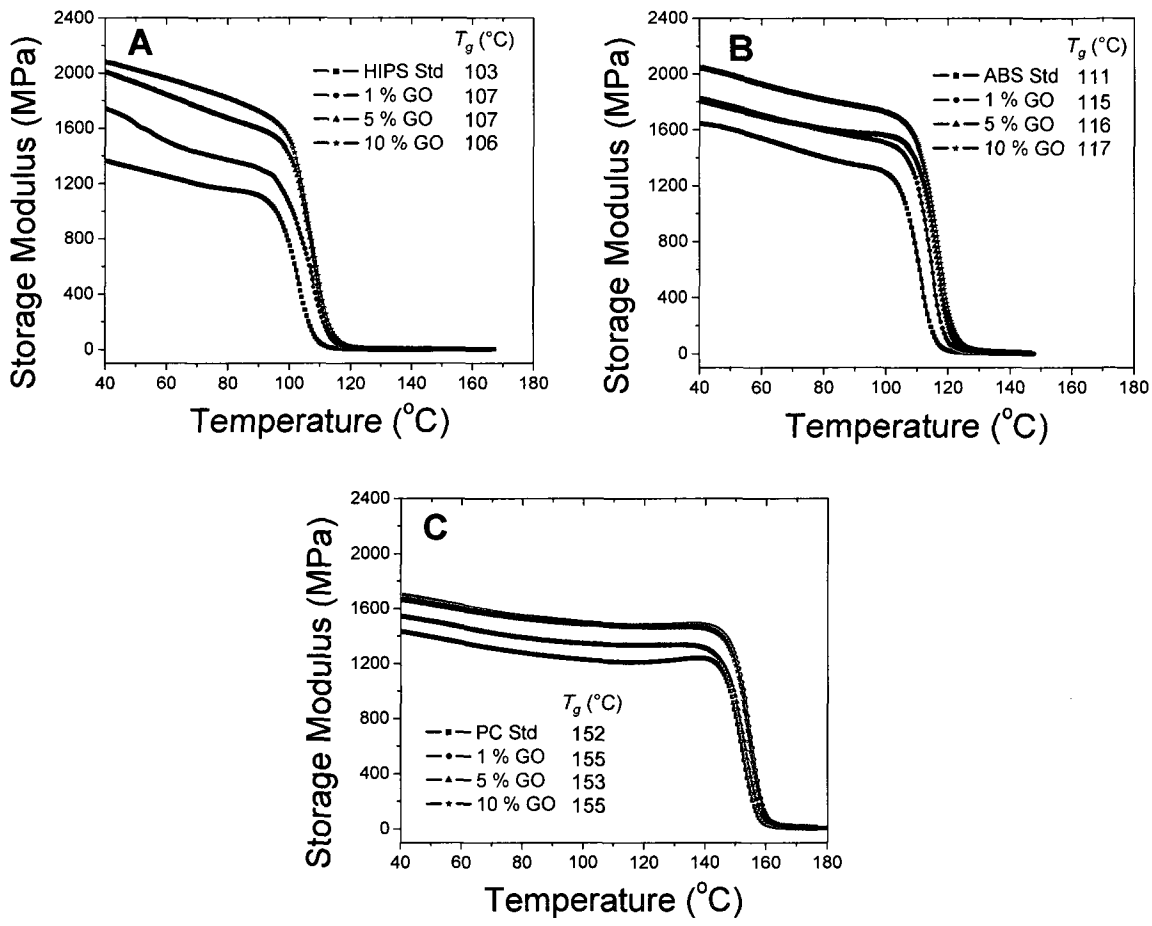

Figure 4.2. DMA storage modulus with increasing temperature for GO composites made with HIPS (A), ABS (B), and PC (C) systems. The T_g for each sample are shown in the inset. For all systems, the storage modulus increases with addition of graphite over a wide temperature range.

4.2.3 Thermal and Flammability Properties

Several techniques were employed to assess the thermal and flammability properties of the GO-polymer composites including MCC, TGA, and vertical open flame testing. The MCC is a small-scale instrument which measures the heat release of a material by oxygen consumption calorimetry, and has been recently employed as a small-scale alternative to cone calorimetry when sample supply is limited.[21] The heat of combustion of pyrolysis products is measured, and the heat release can be used to predict the flammability of the material.[22] Using this technique, the samples are exposed to a fast heating rate to mimic fire-type conditions. The experiment consists of first pyrolyzing the sample under an inert atmosphere (nitrogen in this case) at a heating rate of 1 °C/s from 250 to 750 °C (using method A of ASTM D7309) then pushing the pyrolysis products into a 900 °C combustion furnace where they are mixed with oxygen. The combustion gases from the furnace area then flow to an oxygen sensor, and the heat release is calculated based on the amount of oxygen consumed during the combustion process.

The results of the MCC testing are summarized in Figure 4.3; there is a clear trend that as GO content increases, the total heat release and peak heat release capacity decreases. The one exception to this trend is for PC. PC is known to be sensitive to acids and bases such that the presence of acid or base can have negative effects on flame retardancy.[23-25] At low loading (1 wt%) the effects of GO on heat release are minimal, but at 5 wt%, one sees a negative effect on flammability in both peak heat release and in total heat release, likely

caused by the acidic groups at high enough concentration to result in PC molecular weight degradation and therefore a higher heat release (less PC polymer structure converts to char). At 10 wt% GO, enough of a network structure has been formed such that the GO can lower heat release/mass loss and counter the effects of the acidic groups on the GO surface. So perhaps with the exception of PC, it appears the GO has therefore effectively decreased the flammability of the materials tested. However, while char yield increases as GO is increased, the collected char yields do not appear to be more than additive effects. In fact, it appears that about half of the GO is consumed during the experiment, otherwise the char yields would be even higher assuming 10 wt% GO is thermally stable up to 900 °C. An additional effect noted is that at 10 wt% GO loadings, the polymer sample stops melting and flowing before becoming a char. The appearance of small black dots/char "lumps" roughly in the shape of the starting sample was noted in the 10 wt% GO samples, which is a behavior also seen in carbon nanotube, carbon nanofiber, and clay nanocomposites with good nanoparticle dispersion and low heat release behavior.[26] It is also a feature of a material with anti-dripping behavior (high melt viscosity) during burning.[12,13] Additionally, the heat release rate curve shape (see Appendix 1, Figure 4.4) is unchanged when comparing the control sample to the GO-containing samples. This indicates that the GO is only slowing down the rates of mass loss/fuel pyrolysis and is most likely not changing the thermal decomposition profile/chemistry of the sample.

TGA was performed to assess the general thermal stability of the GO composites compared to the as-received material. In general the thermal profile of the GO composites did not change significantly from that of the starting material. Table 4.1 gives the results of the decomposition onset temperature, defined as the temperature at which 5 wt% weight loss occurred, and the temperature of maximum weight loss rate (peak of the derivative curve). The TGA thermograms and corresponding derivative curves may be found in Appendix 1, Figure 4.5. For the HIPS systems, the temperatures remained fairly constant, except for the 5 wt% GO sample, which increased both the decomposition onset and maximum weight loss rate temperatures (384 °C to 399 °C and 423 °C to 426 °C, respectively). For the ABS systems, both temperatures decreased slightly with increasing GO addition (381 °C to 371 °C and 424 °C to 411 °C for the 10 wt% GO sample), indicating a slight decrease in thermal stability. Both temperatures for the PC systems remained constant for all GO loadings. Therefore, it can be concluded that addition of GO does not significantly alter the thermal stability of the polymer resins to which it is added.

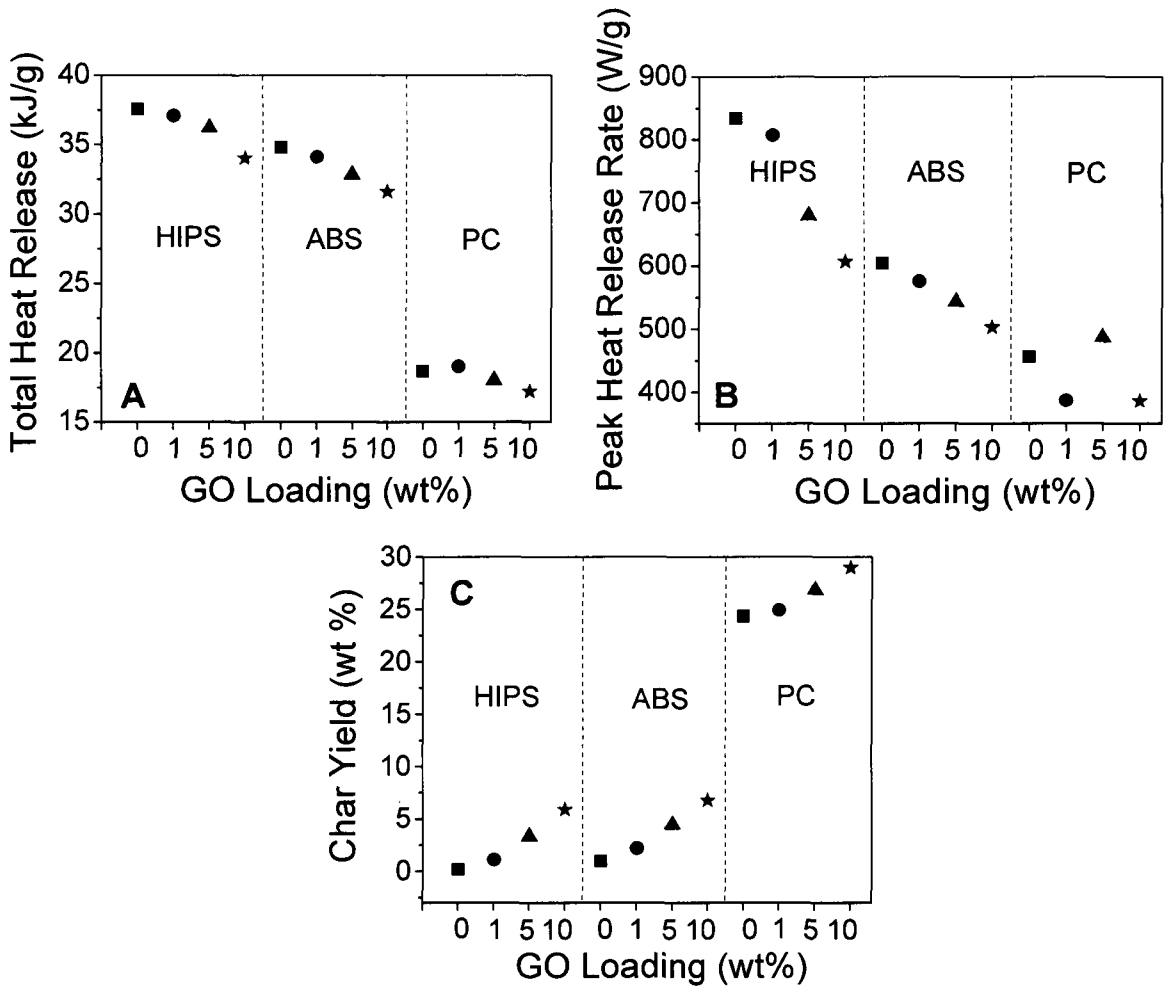

Figure 4.3. MCC results for GO-HIPS, GO-ABS, and GO-PC nanocomposite systems. There is a clear trend that the total heat release (A) and peak heat release rate (B) both decrease as GO content is increased in all polymers. The char yield (C) also increases for all polymer systems as GO is increased, but this seems to be an additive effect.

To further assess material flammability, especially the ability of a molten polymer to drip and spread flame in a fire, vertical open flame testing was performed on a plastic sample, molded into the shape of a rectangular bar (1.3 cm wide, 7.6 cm long, and 0.3 cm thick) that is suspended above a cotton patch. The plastic bar is exposed to a 10 s ignition with a methane-fueled flame that is contained in a flame-testing hood free of passing air currents. After the 10 s ignition period, the flame is removed and the time for the polymer to self-extinguish is recorded. Sample dripping and cotton ignition are also noted. The test performed was a modified version of ASTM D3801; based on the actual flame height that was used, the test method can be classified as being between the UL-V0 (ASTM D3801) and UL-94 5V (ASTM D5048) tests in severity.[27] These methods typically give ratings of V-0, V-1, V-2 to materials based on self-extinguishing time and dripping behavior; however, since the method used was not an exact match to the UL-94 specifications, such assignments cannot be made. Unlike MCC, this type of testing can provide a general assessment as to how GO affects the material's drip behavior in a flaming drip fire risk scenario, which is important to industrial fire safety applications. The vertical fire test results for all composites are summarized in Table 4.1. As expected, the GO-PC composites displayed the best results; the self-extinguishing times for 5 and 10 wt% GO in PC were immediate after removal of the flame. Although the self-extinguishing times of ABS systems were considerably longer, the behavior of the burning material suggests flame retarding behavior with increasing GO content. The ABS standard (no GO present) began elongating almost

immediately after removal of the flame until almost the entire sample dripped after 68 s. With only 1 wt% GO in ABS, the sample did not elongate as drastically. After ~20 s, a small portion of the sample dripped (and ignited the cotton), but most of the sample remained and extinguished immediately after the drip occurred. Similar behavior was observed for 5 and 10 wt% GO in ABS; elongation was diminished such that dripping was only limited to a small portion of the sample and the remaining sample self-extinguished. As expected, the HIPS samples, being the most flammable starting material, performed worst in the flame tests. The standard dripped several times (the first time only 12 s after the flame was removed) and never self-extinguished. The addition of GO to HIPS only increased the amount of time until the first drip; all samples continued burning, even after portions had dripped, until all of the sample was completely consumed.

Despite the poor flame test results for ABS and HIPS, it appears that GO is still an effective additive for lowering the flammability of host polymers. In fact, it has been shown that nanocomposites may display good flame retardant properties while failing flammability tests similar to UL-94.[28] Further, the behavior of heat release and vertical fire tests do not correlate since they are two very different tests.[29] This is important to note since open flame tests alone cannot measure absolute flammability performance, nor does it suggest that the material will provide a high level of fire safety in all fire risk scenarios. However the observations of the sample behavior on burning with this open flame test

combined with MCC and TGA data demonstrate the ability of GO to act as a flame retardant additive.

4.2.4 Flame Retardant Mechanism

The origin of the flame retarding behavior of GO is thought to be its ability to form a continuous, protective char layer which acts as a thermal insulator and a mass transport barrier.[30] This heat-shielding layer slows down the escape of volatile products generated from the degrading polymer. The reductions in mass loss rate observed by TGA, the increases in char yield (less polymer is being pyrolyzed), and increases in melt viscosity all suggest that for GO nanocomposites, the mechanism of flame retardancy is likely a condensed phase phenomena due to formation of a thermal protection/mass loss barrier. The key to achieving this sort of behavior with GO, as with all nanocomposites, is having good dispersion of the nanofiller within the host matrix. The solvent blending and mechanical mixing techniques employed to prepare the samples presented here result in well-dispersed GO within PC, ABS, and HIPS, such that flammability of the composites was significantly decreased with additions of GO as little as 1 wt%. However, to truly elucidate the mechanism of how the GO particles are forming this barrier will require additional research, including rheology studies, melt viscosity measurements, and SEM/TEM work of samples in different states of thermal decomposition (pre- and post-ignition samples as well as post-fire samples).

Table 4.1. Selected Results from TGA and Vertical Fire Test

	TGA		Vertical Fire Test			
Sample	Decomp. Onset (°C)*	Temp. at max wt. loss rate (°C)*	Time to self-extinguish (s)	Observed Dripping	Time Before First Drip (s)	Sample Remaining
HIPS Standard	384	423	n/a	Yes	12	No
1% GO in HIPS	384	418	n/a	Yes	14	No
5% GO in HIPS	399	426	n/a	Yes	17	No
10% GO in HIPS	386	421	n/a	Yes	24	No
ABS Standard	381	424	68	Yes	68	Yes
1% GO in ABS	374	413	21	Yes	68	Yes
5% GO in ABS	366	406	33	Yes	33	Yes
10% GO in ABS	371	411	79	Yes	79	No
PC Standard	475	508	14	Yes	14	Yes
1% GO in PC	471	505	4	No	n/a	Yes
5% GO in PC	475	508	0	No	n/a	Yes
10% GO in PC	477	507	0	No	n/a	Yes

*The temperature of decomposition onset is defined as the temperature at which 5 wt% weight loss occurred. The temperature at the maximum weight loss rate is the temperature at the maximum of the derivative curve.

4.3 Conclusions

GO was blended at 1, 5, and 10 wt% into the commodity polymers HIPS, ABS, and PC to serve as a flame retarding nano-additive. MCC, TGA, and vertical open flame testing demonstrated the diminished flammability of the material as the amount of GO was increased; the total heat release and peak heat release rate decreased while the char yield increased. In addition, SEM and optical microscopy showed that the GO was well dispersed throughout the composite. DMA revealed that the storage modulus increases as the GO loading is increased, and the T_g of the polymer increases slightly. This work reveals that GO shows some promise towards the fabrication of polymer nanocomposites where decreased flammability is desired.

4.4 Experimental

4.4.1 Synthesis of GO

GO was synthesized from expanded graphite obtained from SupraCarbonics, LLC using the Staudenmaier procedure.[17,31] Briefly, 5 g (416.7 mmol C) of expanded graphite was added in five portions to a stirred mixture of concentrated H_2SO_4 (87.5 mL) and fuming HNO_3 (45 mL) while cooling in an ice-water bath. To the mixture was added $KClO_3$ (55 g, 0.45 mol) in eleven separate and equal portions, each added to the reaction mixture 15 min apart while ensuring sufficient venting using nitrogen gas to reduce the risk of explosion upon generation of chlorine dioxide gas. *[Caution: protective equipment including face shield, acid-resistant gloves, and blast shield must be used at all times.]* The resulting slurry was stirred at room temperature for 96 h. The green slurry was poured into 4 L of ice water, and the mixture was filtered and subsequently washed with 5 L of 5% HCl. The filter cake was then rinsed thoroughly with water until the filtrate was neutral. The filter cake was then dispersed in methanol (300 mL, vigorous stirring) and precipitated with diethyl ether (350 mL) followed by a final, thorough rinse with diethyl ether to yield 4.1 g of a fine brown powder of GO.

4.4.2 Formation of GO/PC nanocomposites

The PC resin (10 g, Dow Calibre 301-10) was soaked overnight in 200 mL of tetrahydrofuran (THF) to expand the polymer and begin dissolution. Complete dissolution was achieved the next day by vigorous stirring with a metal spatula

and/or applying heat to the system. In a separate container, GO (in the amount to reach the overall desired weight percentage in the system) was high shear mixed (IKA T-25 digital ULTRA-TURRAX® disperser with 18 G dispersing element, 7000 rpm) for 30 min in ~100 mL THF. The GO/THF suspension was then poured into the dissolved PC/THF solution and high shear mixed for 30 min. To precipitate the GO/PC polymer composite, the mixture was *slowly* added to a 5× volume of methanol (~1500 mL) with vigorous stirring. The GO/PC composite was isolated by filtering over a PTFE membrane (5 μm pore size), washed with methanol, and allowed to dry completely. Sample bars suitable for open flame testing and dynamic mechanical analysis were prepared via melt extrusion (CSI-183MMX Mini Max extruding system). The GO/PC composite was heated until molten and then extruded into a heated stainless steel mold (80 °C, width 1.3 cm, length 7.6 cm, thickness 0.3 cm) at a processing temperature of 270 °C.

4.4.3 Formation of GO/ABS nanocomposites

The ABS resin (10 g, Dow Magnum 9010) was soaked overnight in 200 mL of chloroform ($CHCl_3$) to expand and dissolve the polymer. Complete dissolution was achieved the next day by vigorous stirring with a metal spatula. In a separate container, GO (in the amount to reach the overall desired weight percentage in the system) was high shear mixed for 30 min in ~100 mL $CHCl_3$. The GO/$CHCl_3$ suspension was then poured into the dissolved ABS/$CHCl_3$ solution and high shear mixed for 30 min. To precipitate the ABS/GO polymer composite, the mixture was *slowly* added to a 5× volume of diethyl ether (~1500

mL) with vigorous stirring. The GO/ABS composite was isolated by filtering over a PTFE membrane (5 μm pore size), washed with diethyl ether, and allowed to dry in air. Sample bars suitable for open flame testing and dynamic mechanical analysis were prepared via melt extrusion (CSI-183MMX Mini Max extruding system). The GO/ABS composite was heated until molten and then extruded into a heated stainless steel mold (80 °C, width 1.3 cm, length 7.6 cm, thickness 0.3 cm) at a processing temperature of 240 °C.

4.4.4 Formation of GO/HIPS nanocomposites

The HIPS resin (10 g, Dow Styron 478) was soaked overnight in 200 mL of THF to expand and dissolve the polymer. Complete dissolution was achieved the next day by vigorous stirring with a metal spatula. In a separate container, GO (in the amount to reach the overall desired weight percentage in the system) was high shear mixed for 30 min in ~100 mL THF. The GO/THF suspension was then poured into the dissolved HIPS/THF solution and high shear mixed for 30 min. To precipitate the GO/HIPS polymer composite, the mixture was *slowly* added to a 5× volume of methanol (~1500 mL) with vigorous stirring. The GO/HIPS composite was isolated by filtering over a PTFE membrane (5 μm pore size), washed with methanol, and allowed to dry in air. Sample bars suitable for open flame testing and dynamic mechanical analysis were prepared via melt extrusion (CSI-183MMX Mini Max extruding system). The GO/HIPS composite was heated until molten and then extruded into a heated stainless steel mold

(80 °C, width 1.3 cm, length 7.6 cm, thickness 0.3 cm) at a processing temperature of 250 °C.

4.4.5 Vertical Open Flame Testing

The method used was a modified version of ASTM D3801. Rectangular bars measuring 1.3 cm wide, 7.6 cm long, and 0.3 cm thick were used, and all tests were done in an Atlas Electric HVUL-94 flame-test station. The methane tank pressure regulator was set to 23 psi; the pressure regulator on the HVUL-94 test station was set to 5 psi. The Bunsen burner flame height was 55 mm, and the height from the top of the Bunsen burner to the bottom of the test bar was 40 mm; therefore the sample overlapped with the flame by ~15 mm. All test bars underwent one trial, where the bar was exposed to a 10 s ignition followed by flame removal and the time to self-extinguishing recorded.

4.4.6 Instrumental Testing

MCC Testing. MCC tests (MCC-1, Govmark) were run under nitrogen at a heating rate of 1 °C/s from 250 to 750 °C using method A of ASTM D7309 (pyrolysis under nitrogen). Each sample was run in triplicate to evaluate reproducibility of the flammability measurements.

TGA. TGA analysis (Q50, TA Instruments) was conducted from room temperature to 950 °C at 10 °C/min under argon.

DMA. DMA analysis (Q800, TA Instruments) was performed with a dual cantilever clamp on sample bars measuring 1.3 cm wide, 7.6 cm long, and 0.3

cm thick. A temperature ramp experiment (3 °C/min) was conducted under air from room temperature to 150 °C (ABS and HIPS systems) or 180 °C (PC systems) at a constant frequency of 1 Hz.

SEM. SEM images were obtained at 5.0 kV on freeze fractured cross sections of the respective GO/polymer composite sample bar. Before imaging, the samples were coated with a 20 nm layer of gold to minimize charging.

Optical microscopy. The samples were imaged using a polarizing optical microscope (Zeiss Axioplan-2) by first melting a small portion of the polymer composite by heating in an oven, and then pressing a thin layer onto a glass microscope slide.

4.5 References

1. Beyer, G. In *Flame Retardant Polymer Nanocomposites*, Morgan, A. B., Wilkie, C. A., Eds.; John Wiley & Sons, Inc.: Hoboken, 2007; p 163-190.
2. Vaia, R. A.; Maguire, J. F. *Chem. Mater.* **2007**, *19*, 2736-2751.
3. Blomqvist, P.; Rosell, L.; Simonson, M. *Fire Technol.* **2004**, *40*, 39-58.
4. Blomqvist, P.; Rosell, L.; Simonson, M. *Fire Technol.* **2004**, *40*, 59-73.
5. Levchik, S. V.; Weil, E. D. *J. Fire Sci.* **2006**, *24*, 345-364.
6. Paul, D. R.; Robeson, L. M. *Polymer* **2008**, *49*, 3187-3204.
7. Winey, K. I.; Vaia, R. A. *MRS Bull.* **2007**, *32*, 314-322.
8. Bredeau, S.; Peeterbroeck, S.; Bonduel, D.; Alexandre, M.; Dubois, P. *Polym. Int.* **2008**, *57*, 547-553.

9. Jang, B. Z.; Zhamu, A. *J. Mater. Sci.* **2008**, *43*, 5092-5101.

10. Modesti, M.; Lorenzetti, A.; Simioni, F.; Camino, G. *Polym. Degrad. Stab.* **2002**, *77*, 195-202.

11. Shi, L.; Li, Z.-M.; Xie, B.-H.; Wang, J.-H.; Tian, C.-R.; Yang, M.-B. *Polym. Int.* **2006**, *55*, 862-871.

12. Kashiwagi, T.; Du, F.; Douglas, J. F.; Winey, K. I.; Harris, R. H.; Shields, J. R. *Nat. Mater.* **2005**, *4*, 928-933.

13. Kashiwagi, T.; Du, F.; Winey, K. I.; Groth, K. M.; Shields, J. R.; Bellayer, S. P.; Kim, H.; Douglas, J. F. *Polymer* **2005**, *46*, 471-481.

14. Song, P. a.; Xu, L.; Guo, Z.; Zhang, Y.; Fang, Z. *J. Mater. Chem.* **2008**, *18*, 5083-5091.

15. Lerf, A.; He, H.; Forster, M.; Klinowski, J. *J. Phys. Chem. B* **1998**, *102*, 4477-4482.

16. Steurer, P.; Wissert, R.; Thomann, R.; Mülhaupt, R. *Macromol. Rapid Commun.* **2009**, *30*, 316-327.

17. McAllister, M. J.; Li, J.-L.; Adamson, D. H.; Schniepp, H. C.; Abdala, A. A.; Liu, J.; Herrera-Alonso, M.; Milius, D. L.; Car, R.; Prud'homme, R. K.; Aksay, I. A. *Chem. Mater.* **2007**, *19*, 4396-4404.

18. Zhang, R.; Hu, Y.; Xu, J.; Fan, W.; Chen, Z. *Polym. Degrad. Stab.* **2004**, *85*, 583-588.

19. Zhang, R.; Hu, Y.; Xu, J.; Fan, W.; Chen, Z.; Wang, Q. *Macromol. Mater. Eng.* **2004**, *289*, 355-359.

20. Lyon, R. E.; Takemori, M. T.; Safronava, N.; Stoliarov, S. I.; Walters, R. N. *Polymer* **2009**, *50*, 2608-2617.

21. Morgan, A. B.; Galaska, M. *Polym. Adv. Technol.* **2008**, *19*, 530-546.

22. Lyon, R. E.; Walters, R. N. *J. Anal. Appl. Pyrolysis* **2004**, *71*, 27-46.

23. Grause, G.; Sugawara, K.; Mizoguchi, T.; Yoshioka, T. *Polym. Degrad. Stab.* **2009**, *94*, 1119-1124.

24. Levchik, S. V.; Weil, E. D. *Polym. Int.* **2005**, *54*, 981-998.

25. Levchik, S. V.; Weil, E. D. *J. Fire Sci.* **2006**, *24*, 137-151.

26. Morgan, A. B. *Polym. Adv. Technol.* **2006**, *17*, 206-217.

27. UL 94: Standard for Tests for Flammability of Plastic Materials for Parts in Devices and Appliances. 5th ed.; Underwriters Laboratories, Inc.: Research Triangle Park, NC, 1996.

28. Bourbigot, S.; Duquesne, S.; Fontaine, G.; Bellayer, S.; Turf, T.; Samyn, F. *Mol. Cryst. Liq. Cryst.* **2008**, *486*, 325-339.

29. Morgan, A. B.; Bundy, M. *Fire Mater.* **2007**, *31*, 257-283.

30. Kashiwagi, T. In *Flame Retardant Polymer Nanocomposites*, Morgan, A. B., Wilkie, C. A., Eds.; John Wiley & Sons, Inc.: Hoboken, 2007; p 285-324.

31. Staudenmaier, L. *Ber. Dtsch. Chem. Ges.* **1898**, *31*, 1481-1487.

4.6 Experimental Contributions

My contribution to the experimental work in this chapter is the following: synthesis of GO and nanocomposite fabrication. I also performed the vertical flame testing, TGA, DMA, SEM, and optical microscopy analysis. Jay R. Lomeda assisted in the GO synthesis, and gave advice on sample preparation and analysis. Alex B. Morgan (University of Dayton Research Institute) gave experimental advice, performed the MCC testing, and wrote portions of the discussion of the MCC results.

4.7 Appendix 1

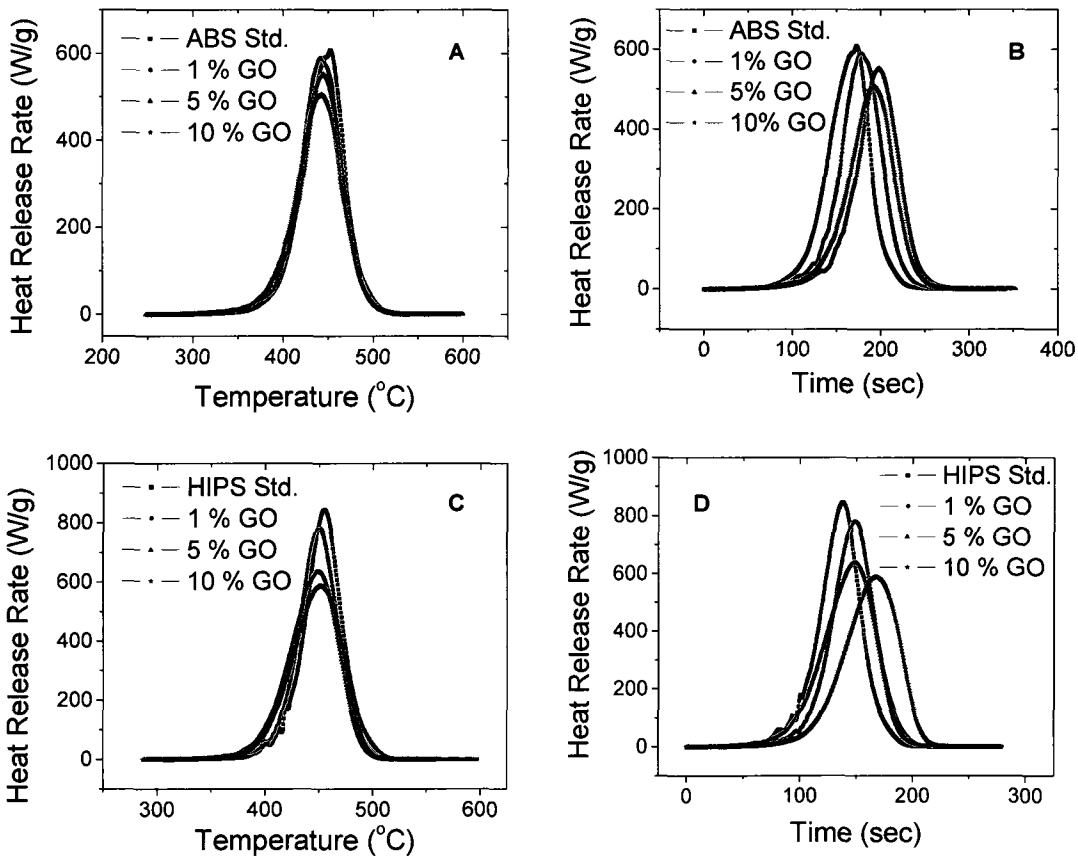

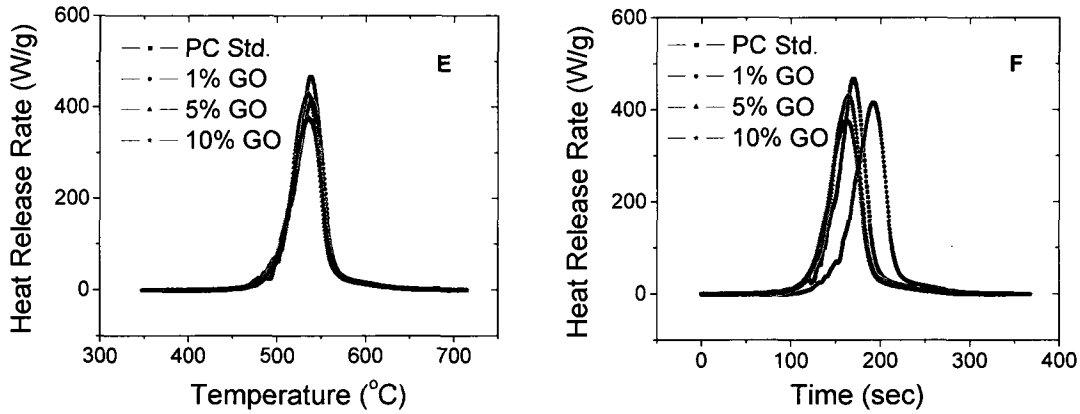

Figure 4.4. Heat release rate curves versus temperature (A, C, E) and time (B, D, F) for ABS (A, B), HIPS (C, D), and PC (E, F) systems. After incorporation of GO, the overall shape of the curve does not change which implies the GO is only slowing down the rates of mass loss/fuel pyrolysis and is most likely not changing the thermal decomposition profile/chemistry of the sample.

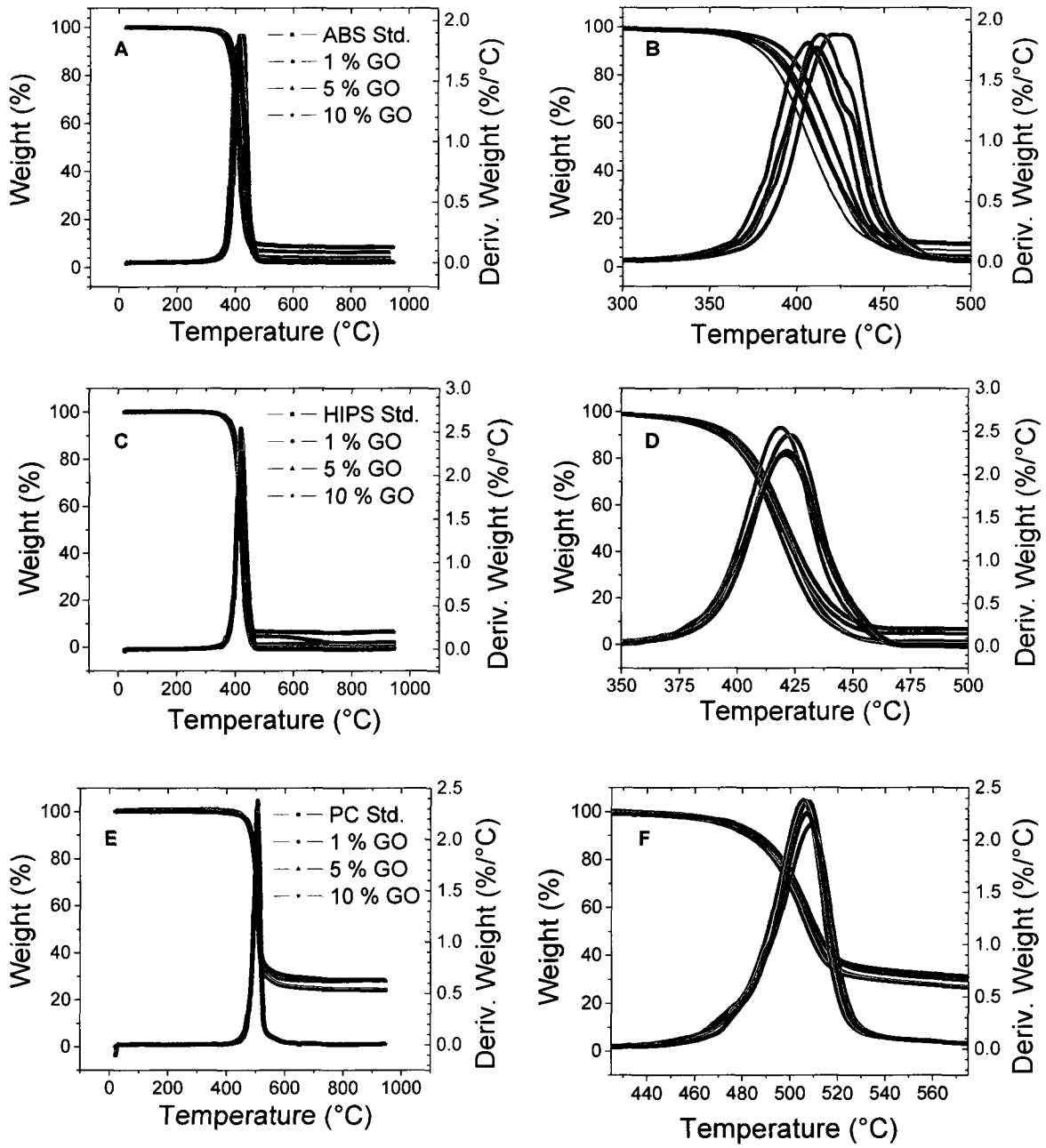

Figure 4.5. TGA thermograms and derivative curves for ABS (A, B), HIPS (C, D), and PC (E, F) systems. The curves shown in the right-hand column are exactly the same as the curve directly to the left, but it is zoomed in at the temperature region in which the major weight loss transition is taking place.

Chapter 5

Longitudinal Unzipping of Carbon Nanotubes to Form Graphene Nanoribbons

5.1 Introduction

Graphene, or single layered graphite, with its high crystallinity and interesting semi-metal electronic properties, has emerged as an exciting 2-D material showing great promise for the fabrication of nanoscale devices.[1-3] Thin, elongated strips of graphene that possess straight edges, termed graphene ribbons, gradually transform from semiconducting to semi-metals as their width increases[4-7] and represent a particularly versatile variety of graphene. Several lithographic,[7,8] chemical,[9-11] plasma-etching,[12] and synthetic[13] procedures have been reported to produce microscopic samples of graphene nanoribbons while one chemical vapor deposition process[14] has successfully produced macroscopic quantities of nanoribbons at 950 °C.

This chapter describes a simple solution-based oxidative process for producing nearly 100% yield of nanoribbon structures via lengthwise cutting and unraveling of multi-walled carbon nanotube (MWCNT) sidewalls. Although oxidative shortening of MWCNTs has been reported previously,[15] lengthwise cutting is heretofore unreported. The same process was also applied to single-walled carbon nanotubes (SWCNTs), and preliminary results show that lengthwise unzipping occurs. However, SWCNT-derived "narrow" ribbons are more difficult to study due to their smaller size (3 – 5 nm width) and tendency to aggregate and entangle.

Theoretical studies predict that the high surface energy of single atomic layer nanoribbons would cause them to stack or fold to produce carbon nanotubes, thus hindering direct growth from the gas phase.[16] However, this

does not apply in liquid media. The excess surface energy of an individual graphene nanoribbon is compensated by solvation, and folding into a nanotube structure then becomes an endothermic process.[17] Therefore, the reverse process – cleaving of a nanotube into a graphene nanoribbon – is favorable in an appropriate solvent system.

The oxidized graphene nanoribbons (GONRs) obtained from the *longitudinal opening of MWCNTs are highly soluble in water.* Subsequent chemical reduction of the GONRs produces graphene nanoribbons (GNRs) with restoration of electrical conductivity. These early-stage results affording nanoribbons could eventually lead to applications in fields of electronics and composite materials when bulk quantities of nanoribbons are required.[18-20]

5.2 Results and Discussion

5.2.1 Reaction Protocol and Proposed Mechanism

GONRs were obtained by suspending MWCNTs in concentrated sulfuric acid followed by treatment with 500 wt% potassium permanganate ($KMnO_4$) for 1 h at room temperature and 1 h at 55 – 70 °C (see Experimental for full description). After isolation, the resulting GONRs were highly soluble in water (12 mg/mL), ethanol, and other polar organic solvents. The opening of the nanotubes appears to occur within a line, similar to the "unzipping" of graphite oxide,[21,22] affording straight-edge ribbons. This could occur in a linear longitudinal cut (Figure 5.1a) or in a spiraling manner, depending upon the initial site of attack and the chiral angle of the nanotube. Although depicted in Figure

5.1a as initiating internally rather than at one end, the location of initial attack is not known and most likely varies.

The mechanism for the opening is based upon literature precedent for the oxidation of alkenes by permanganate in acid. The proposed first step in the process is manganate ester formation (**2** in Figure 5.1b) as the rate-determining step, and further oxidation is possible to afford the dione (**3**) in the dehydrating medium.[23] Juxtaposition of the buttressing ketones distorts the β,γ-alkenes (red in **3**) making them more prone to the next attack by permanganate. As the process continues, the buttressing-induced strain on the β,γ-alkenes lessens since there is more space for carbonyl projection; however, the bond-angle strain induced by the enlarging hole (or tear if originating from the end of the nanotube) would make the β,γ-alkenes (**4** in Figure 5.1b) increasingly reactive. Hence, once an opening is initiated, its further opening is enhanced relative to an unopened tube or to an uninitiated site on the same tube. The ketones can be further converted, through their O-protonated forms, to the carboxylic acids[24] that will line the edges of the nanoribbons. Finally, relief of the bond-angle strain when the nanotube opens to the graphene ribbon (**5** in Figure 5.1b) slows further dione formation and cutting.[23] Thus, the preference for sequential bond cleavage over random opening and subsequent cutting, as occurs with nitric acid oxidation, can be explained by concerted attachment to neighboring carbon atoms by permanganate while the nitronium species from nitric acid does not concertedly attack neighboring carbons. The surface of the now less strained nanoribbon remains prone to 1,2-diol formation which leads to the overall highly oxidized

ribbon, but this is less likely to result in further oxidative cutting to the dione due to relief of the tubular strain on the double bonds.

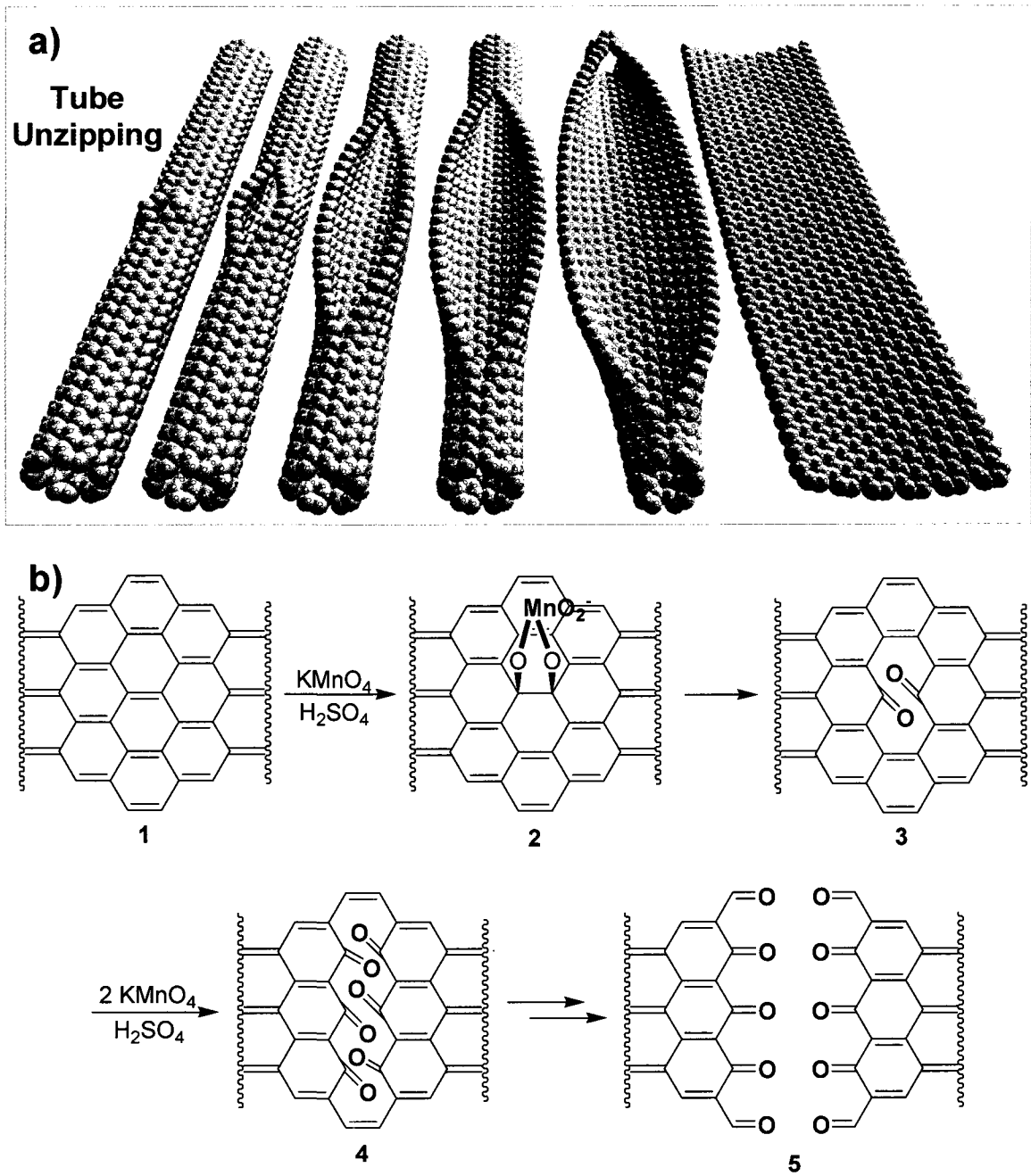

Figure 5.1. a) Schematic representation of the gradual unzipping of one wall of a carbon nanotube to form a GONR. Oxygenated sites are not shown. b) The

proposed chemical mechanism of nanotube unzipping. The manganate ester in **2** could also be protonated. The β,γ-alkenes (red in **3** and **4**) are distorted due to the buttressing ketones; the resulting bond-angle strain promotes further reaction at these sites.

5.2.2 GONR Imaging

Transmission electron microscopy (TEM), atomic force microscopy (AFM), and scanning electron microscopy (SEM) were used to image the GONRs. TEM analysis shows nanoribbons (Figure 5.2a) produced from MWCNTs with a starting diameter of 40 – 80 nm and approximately ~30 inner nanotube layers (additional TEM images of untreated MWCNTs may be found in Appendix 2, Figure 5.10a-b). After reaction, the width of the carbon nanostructures increased to >100 nm and had linear edges with little pristine MWCNT sidewall structure remaining (see Appendix 2, Figures 5.8c-d and 5.9a-d for additional TEM and SEM images). The MWCNTs used were produced from a CVD process;[25] the same $H_2SO_4/KMnO_4$ treatment was attempted on a singular sample of laser-oven produced MWCNTs but less nanoribbon-like structures were detected. AFM imaging (Figure 5.2b) shows the presence of single atomic layers after the solution is tip-sonicated for 30 min to yield well dispersed and sonication-shortened GONRs suitable for imaging. SEM imaging (Figure 5.2c) of GONRs on a silicon surface reveals that the ribbons remain long (~4 μm in this image) when not tip-sonication cut; they can be dispersed as single or thin layers and they display uniform widths and straight edges over their entire length.

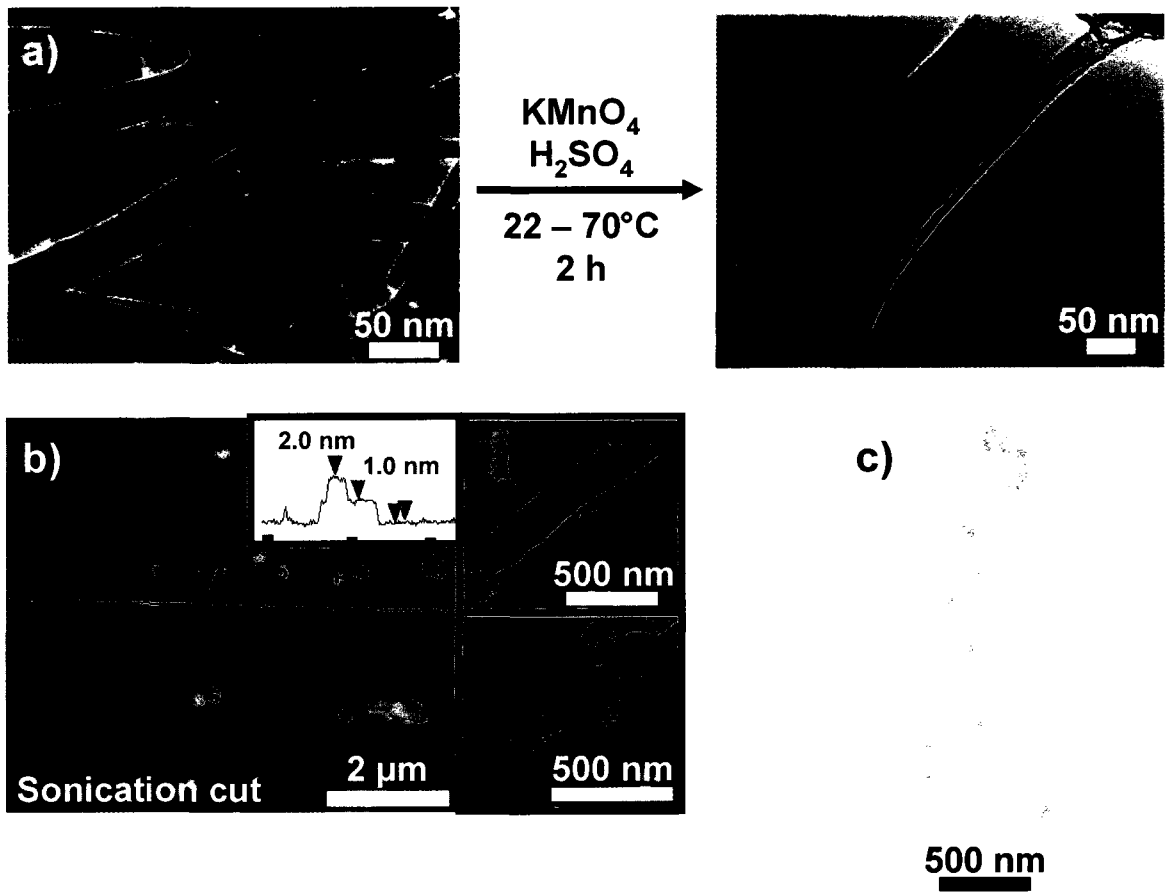

Figure 5.2. a) TEM images depicting the transformation of MWCNTs (left) into GONRs (right). The right side of the ribbon is partially folded onto itself. The dark structures are part of the carbon imaging grid. b) AFM images of partially stacked multiple short fragments of nanoribbons that were horizontally cut by tip-ultrasonic treatment of the original oxidation product to facilitate spin-casting onto the mica surface. From the height data (inset), the ribbons are generally single-layered. The two smaller figures to the right show some other characteristic nanoribbons. c) SEM image of a folded 4 μm-long single-layer GONR on a silicon surface.

5.2.3 Stepwise Oxidation of MWCNTs

The degree of consecutive tube opening in the MWCNTs can also be controlled by the amount of oxidizing agent introduced into the system; it was found using TEM as a probe that 80-100% of MWCNTs present had completely unraveled sidewalls to form GONRs when 500 wt% $KMnO_4$ was used. The successive opening reaction was demonstrated in five iterations, each containing a step-wise increase in the amount of $KMnO_4$. The first iteration with 100 wt% $KMnO_4$ (sample I), second iteration with 200 wt% $KMnO_4$ (sample II), etc. until the final iteration with 500 wt% $KMnO_4$ (sample V). This results in consecutive unencapsulating of the different layers by unzipping of the successive MWCNTs (see Experimental for details). It is evident from TEM images (Figure 5.3a-e) that the walls of the MWCNTs are opened to a higher degree with less MWCNT inner tube remaining as the level of oxidation increases. This is highlighted in Figure 5.3f with a statistical plot showing the decrease of the average remaining MWCNT diameter from ~65 nm to ~20 nm as the amount of $KMnO_4$ exposure is increased. The smaller diameter tubes that remain after treatment with 500 wt% $KMnO_4$ are exposed to the reaction conditions for less time than the larger diameter tubes and thus may not have had the chance to fully react; no difference in the rate of unzipping between small and large diameter nanotubes can be inferred from these data.

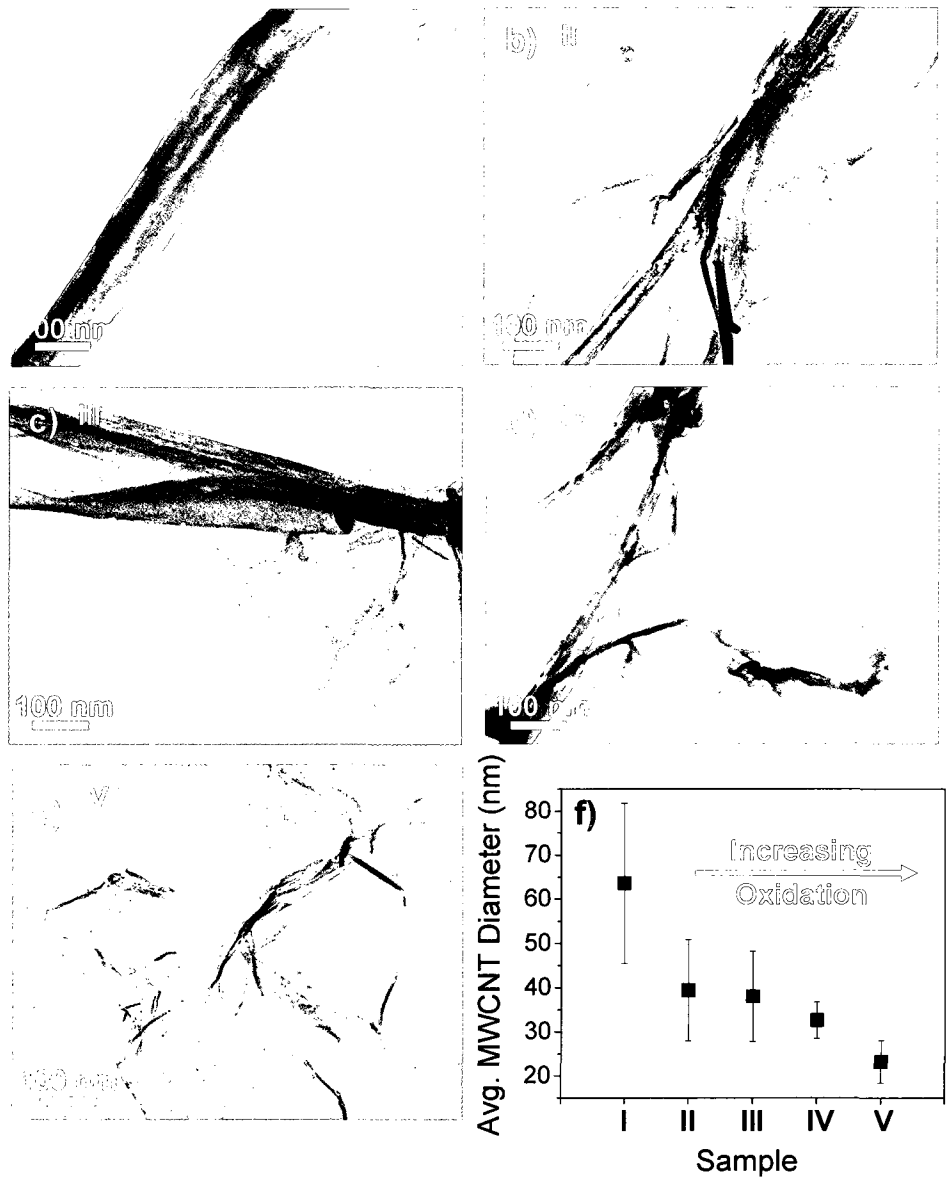

Figure 5.3. a-e) TEM images of the stepwise opening of MWCNTs representing the incremental exposure of $KMnO_4$ to the system, with a) the least oxidized sample (sample I) and e) the most oxidized (sample V). f) A scatter plot showing how the average MWCNT diameter (detected by studying 15-20 TEM images per sample, each with ~5 MWCNTs per image) changes with increasing exposure to $KMnO_4$. Error bars give the standard deviation of the average MWCNT diameter across the sample.

The degree of oxidation of the product formed (partially and/or completely unraveled MWCNTs) from each of the five iterative $KMnO_4$ treatment steps was monitored by attenuated total-reflectance infrared (ATR-IR) spectroscopy and thermogravimetric analysis (TGA). ATR-IR (Figure 5.4a) reveals the appearance of a C=O stretch (purple region, Figure 5.4a) increasing from 1690 cm^{-1} in sample III (green line) to 1710 cm^{-1} in sample V (black line), consistent with declining conjugation. The COO–H/O–H stretch (~3600-2800 cm^{-1}, yellow region, Figure 5.4a) appears with sample III and continues to increase through the series indicating increasing number of carboxyl and hydroxyl functionalities as well as the possible presence of trapped water. TGA shows an increase in the total weight loss (20% and 49% in samples I and V, respectively) with increasing exposure to $KMnO_4$, implying an increase in the number of volatile sidewall functionalities present which correlates with a higher degree of oxidation (Figure 5.4c). Furthermore, Raman spectroscopy (Figure 5.4d) shows an increasing level of disorder (appearance of D-band at 1321-1328 cm^{-1}) with increasing oxidation, consistent with ATR-IR and TGA observations.

XRD analysis (Figure 5.4b) was also performed to further investigate the structure of the partially and completely unzipped MWCNT-GONR structures. The graphite (002) spacing increases with the level of oxidation. Samples I-III all have 2-θ values of ~25.8° corresponding to a d-spacing of 3.4 Å. Sample IV shows two peaks, one at 10.8° and one at 25.4° with d-spacing 8.2 Å and 3.5 Å, respectively. Sample V shows predominantly a peak at 10.6°, corresponding to

8.3 Å, with minimal signal contributed by MWCNTs (2-θ 25.8°), a spectrum very similar to that of GO.

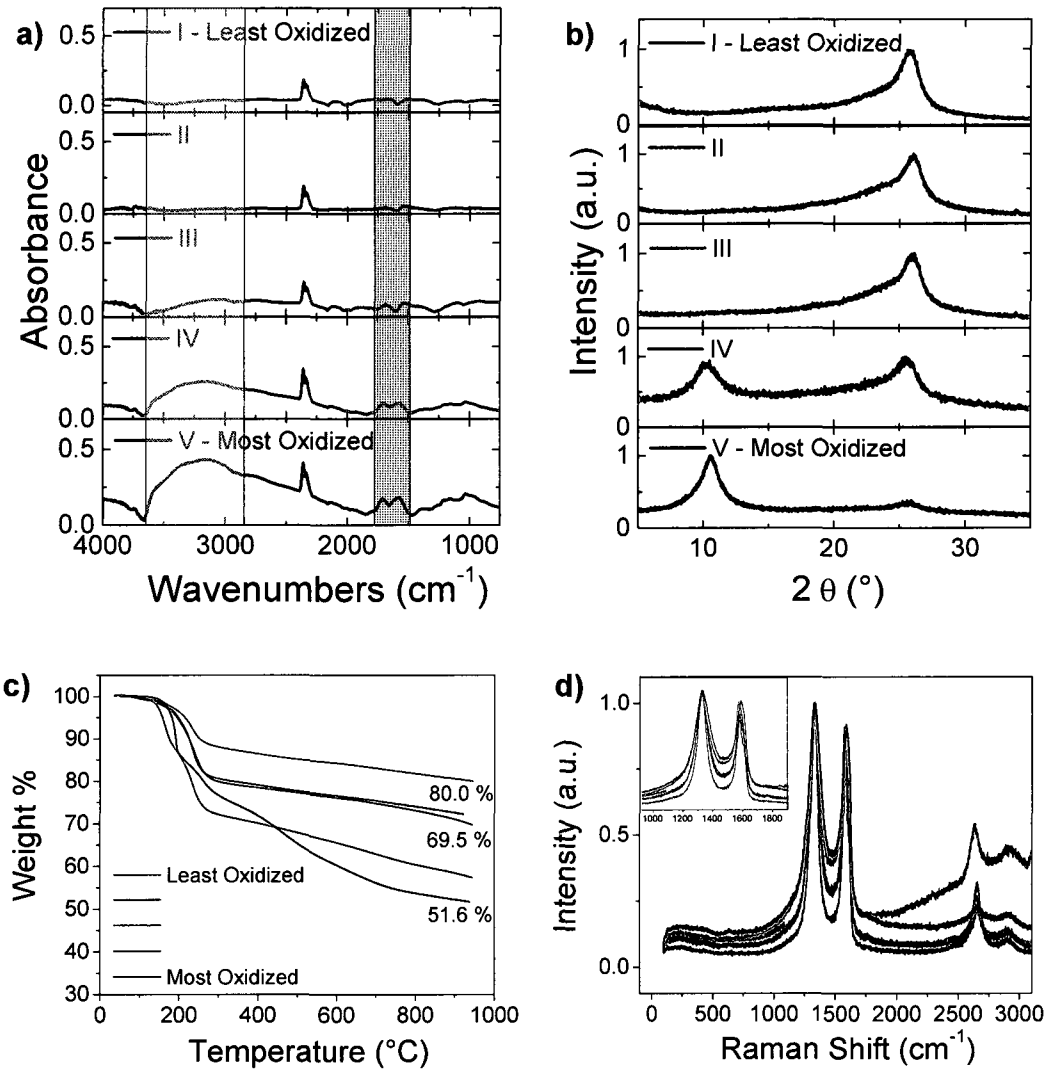

Figure 5.4. a) ATR-IR of stepwise opening/oxidation of MWCNTs. b) XRD analysis of the stepwise nanotube opening. c) TGA weight loss curves of samples I-V; as the level of oxidation increases, the total amount of weight loss is increased. d) The Raman spectra of samples I-V; as the level of oxidation increases, the ratio of the D:G bands increases and becomes less resolved. Inset shows enlargement of D and G bands.

5.2.4 Chemical Reduction of GONRs

The structure of GONRs formed from the oxidative unzipping of MWCNTs resembles that of graphite-oxide (GO), as confirmed by comparing the XRD diffraction patterns (Figure 5.5a). In addition, both GONRs and GO possess oxygen-containing functionalities such as carbonyls, carboxyls and hydroxyls[26] which have been shown to exist at the edges and the surface.[27] The surface oxidation disrupts the π-conjugated network, rendering the GONRs and GO poorly conductive. Hydrazine (N_2H_4) reduction of GO[28] is known to provide a means for restoring conjugation and thus some of the conductivity to form chemically converted graphene (CCG).[28-31] The structure of CCG is thought to be a patchwork of intact graphene islands interspersed with regions of tetrahedral sp^3-hybridized carbon atoms due to incomplete reduction and incomplete rearomatization; therefore, the electrical conductivity is not as high as that found in the original graphite.[29] The carboxyl groups, which are found predominately at the edges,[28] are not reduced by N_2H_4 and remain in the product, further disrupting the π-network.[7,8] Furthermore, as the number of oxygen-containing functionalities decrease during the reduction process, the tendency to aggregate due to π-stacking increases.

The reduction of oxidized nanoribbons was carried out with aqueous N_2H_4 in the presence of ammonia. In order to prevent reaggregation during the reduction procedure, the nanoribbons were first dispersed in aqueous surfactant solution, sodium dodecyl sulfate (SDS), to produce stable dispersions of reduced nanoribbons that retained their straight-edge structure (Figure 5.5b). The

reaction progress was monitored by UV absorption (Figure 5.5c); the bathochromic shift of λ_{max} and the hyperchromicity over the entire range (>230 nm) indicates that electronic conjugation of the ribbons was restored.[28]

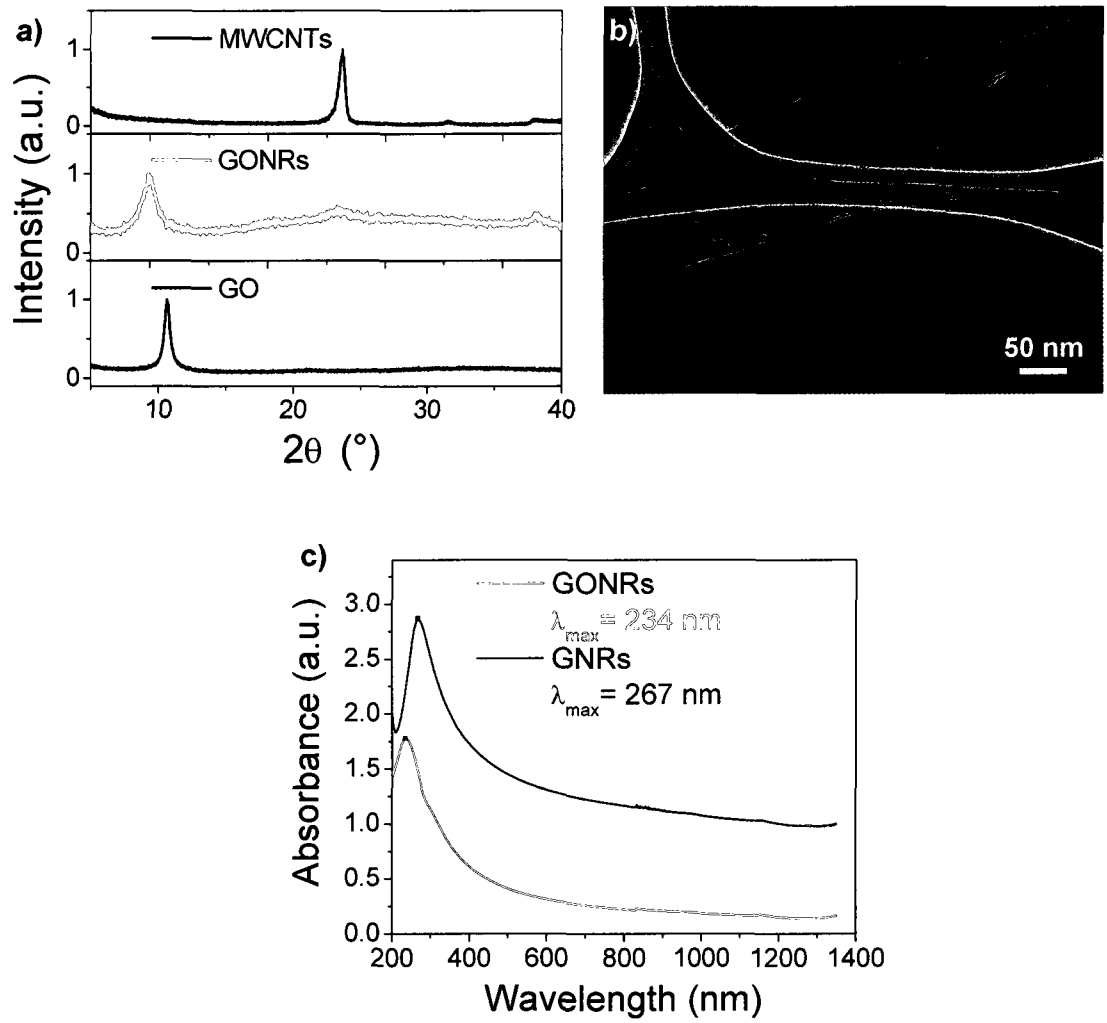

Figure 5.5. a) XRD analysis showing the structure of the GONRs (red trace) in contrast to the MWCNT starting material (black trace) and the similarity in structure to GO (violet trace prepared by the Hummers method[26] is shown with 2-θ ~10.6°). Comparing the XRD patterns of MWCNT and the GONRs, the (002) spacing shifted from 26° to 10° after oxidation, making it GO-like. b) TEM image

of GNRs obtained by treatment of GONRs with N_2H_4. Detailed examination of the image reveals 2-3 ribbons are stacked with apparent buckling. The dark structures are part of the carbon imaging grid. c) Changes in the UV spectrum of an aqueous solution of GONRs (red) and GNRs after treatment with N_2H_4 (blue).

To further support the notion that the reduction procedure decreased the number of oxygen-containing functionalities from the nanoribbon surface, ATR-IR, X-ray photoelectron spectroscopy (XPS), and TGA were employed (Figure 5.6a-c). In the ATR-IR spectrum, the GNRs (blue line, Figure 5.6a) show almost complete elimination of the COO-H/O-H stretching region (~3600-2800 cm^{-1}, yellow region, Figure 5.6a) and a significant decrease in the C=O stretching region (~1710 cm^{-1}, purple region, Figure 5.6a) compared to the intense COO-H/O-H and C=O stretches observed for the GONRs (red line, Figure 5.6a). Edge carboxylic acids will remain. In the XPS C1s spectra of the GONRs and GNRs (Figure 5.6b), the signals at 286 eV and 287 eV correspond to C-O and C=O, respectively. The shoulder at 289 eV is assigned to carboxyl groups. After reduction (blue line), the 286 and 287 eV peaks are diminished to a shoulder of the C-C peak (284.4 eV) indicating significant deoxygenation of the nanoribbons by N_2H_4. As reported for CCG, the most dominant peak after reduction is the C-C peak at 284.8 eV.[32] In addition, the XPS-determined atomic concentration of oxygen (complete table found in Appendix 2, Figure 5.10a) is decreased from 42% to 16% after reduction, but is still higher than the oxygen content of MWCNTs (2.1%) due, in large part, to the edge carboxylic acid moieties. The

TGA weight loss of the reduced nanoribbons was ~33% less than that of the oxidized starting material, which also indicates that fewer oxygen-containing functionalities are present on the nanoribbon surface (Figure 5.6c). The oxidized sample experiences a sharp drop at ~200 °C due to dehydration and possible decarboxylation of the oxygen-containing functional groups yielding CO_x.[27,33] The absence of such groups in the post-reduction sample increases the thermal stability and results in the weight loss curve to be more gradual.[29] Nitrogen adsorption measurements of GONRs and GNRs give BET surface areas of 445 and 436 m^2/g, respectively, after pre-outgassing at 400 °C for 12 h.[14] The density of the GONRs was found to be 2.0 g/cm^3 via solution density match (bromotrichloromethane). When considering the overall conversion of MWCNTs to GNRs, the material weight yield is 99% (see Experimental), underscoring the efficiency of the overall process.

Recent interest in graphene nanoribbons has focused on the study of the reactive edges having zigzag or armchair morphologies which dominate their electronic and magnetic behavior.[5] Although zigzag-edged structures are presumed by the mechanism described here,[34] we were unable to achieve the needed edge resolution for confirmation (see Appendix 2, Figure 5.11). This is due, in part, to edge folding, and could be further attributed to the extensive edge oxidation which might be removed only upon treatment at ≥ 2000 °C, whereupon reconstruction and modified electronic properties would result. Additionally, use of an aberration-corrected TEM microscope to achieve higher resolution might solve this problem; however, one is not currently available at Rice University.

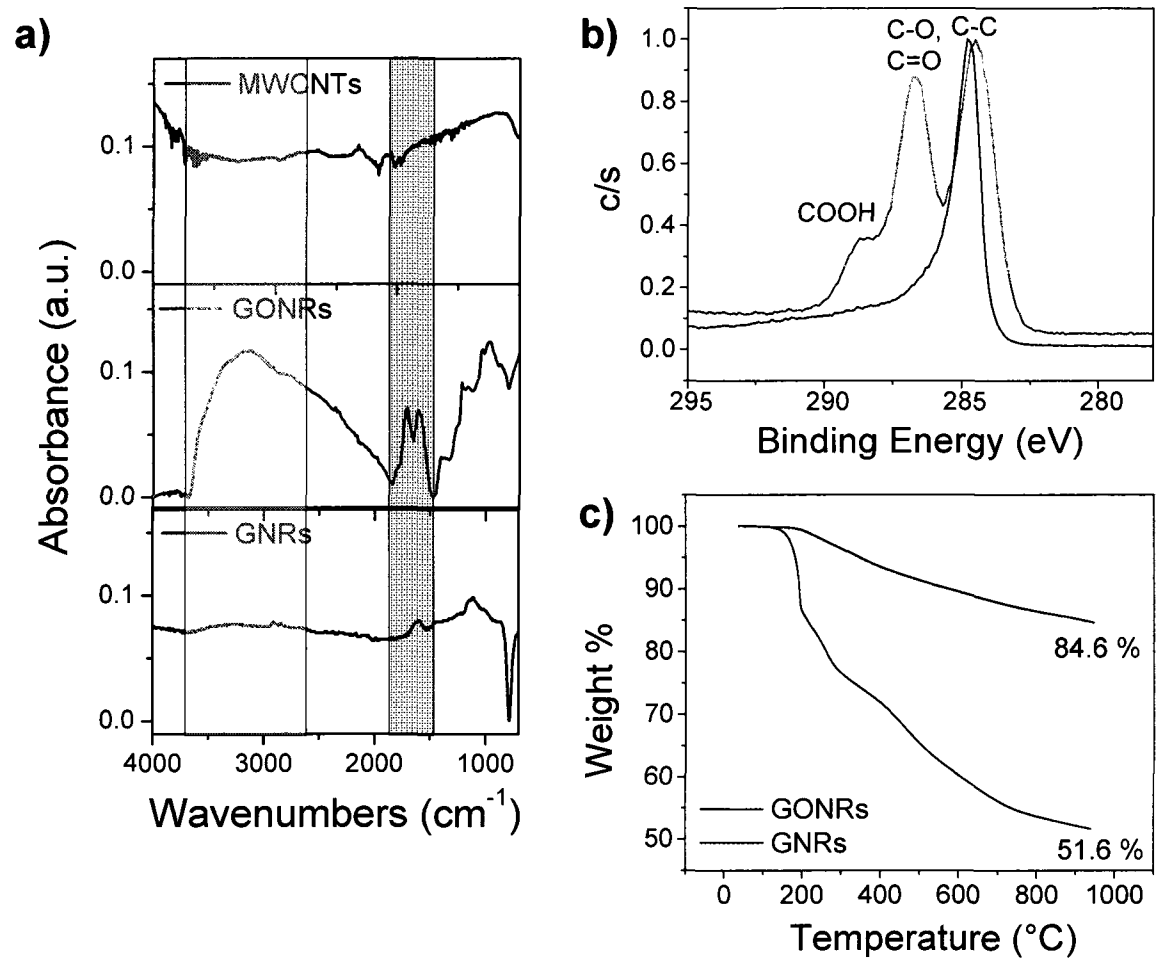

Figure 5.6. a) ATR-IR of GONRs (red) and hydrazine-reduced GNRs (blue) compared to MWCNT starting material (black). b) Normalized superimposed XPS C1s spectra of GONRs (red) and GNRs (blue). c) TGA of GONRs (red) and GNRs (blue) (10°C/min to 950°C under argon). Before reduction, the oxidized sample loses more total weight (49%) than after reduction (15%).

5.2.5 Device Fabrication and Electrical Properties of GNRs on SiO_2/Si

Even though the oxidized edges and planes of the GONRs derived from this bulk process are expected to have diminished performance, the electronic properties of the nanoribbons before and after chemical reduction were studied by building 3-terminal devices on Si/SiO_2 substrates. The long lengths of the GNRs make them easily adapted structures for device fabrication (Figure 5.7a); e-beam-patterned Pt-electrodes were evaporated atop the GNR stack. As-prepared GONRs are poor conductors due to the high number of oxygen-containing functionalities present on the surface; however, their conductivity can be dramatically increased by either chemical reduction using N_2H_4 or by annealing in H_2 (Figure 5.7b). Thick GNR stacks exhibit little gate effect, which is in accord with previously reported data.[35] Conversely, bilayers of GNRs exhibit field effect properties with a minimum conductivity at zero gate voltage, which is as expected for undoped field-effect devices made from exfoliated graphene sheets and superior to CCGs (Figure 5.7c-d).[2,35] The conductivities obtained from these GNRs are analogous to device properties obtained from other reported CVD-grown or exfoliated wide nanoribbons.[2,35] Although the preparative route described here can have the advantage of large-scale nanoribbon access, these unzipping-derived GNRs, with their residual oxidized defect sites, possess inferior electronic characteristics when compared to wide mechanically peeled sheets of graphene.[2,35] However, more recent advances in our laboratory are showing electronic behaviors from these MWCNT-derived GNRs that are approaching those of exfoliated graphite GNRs.

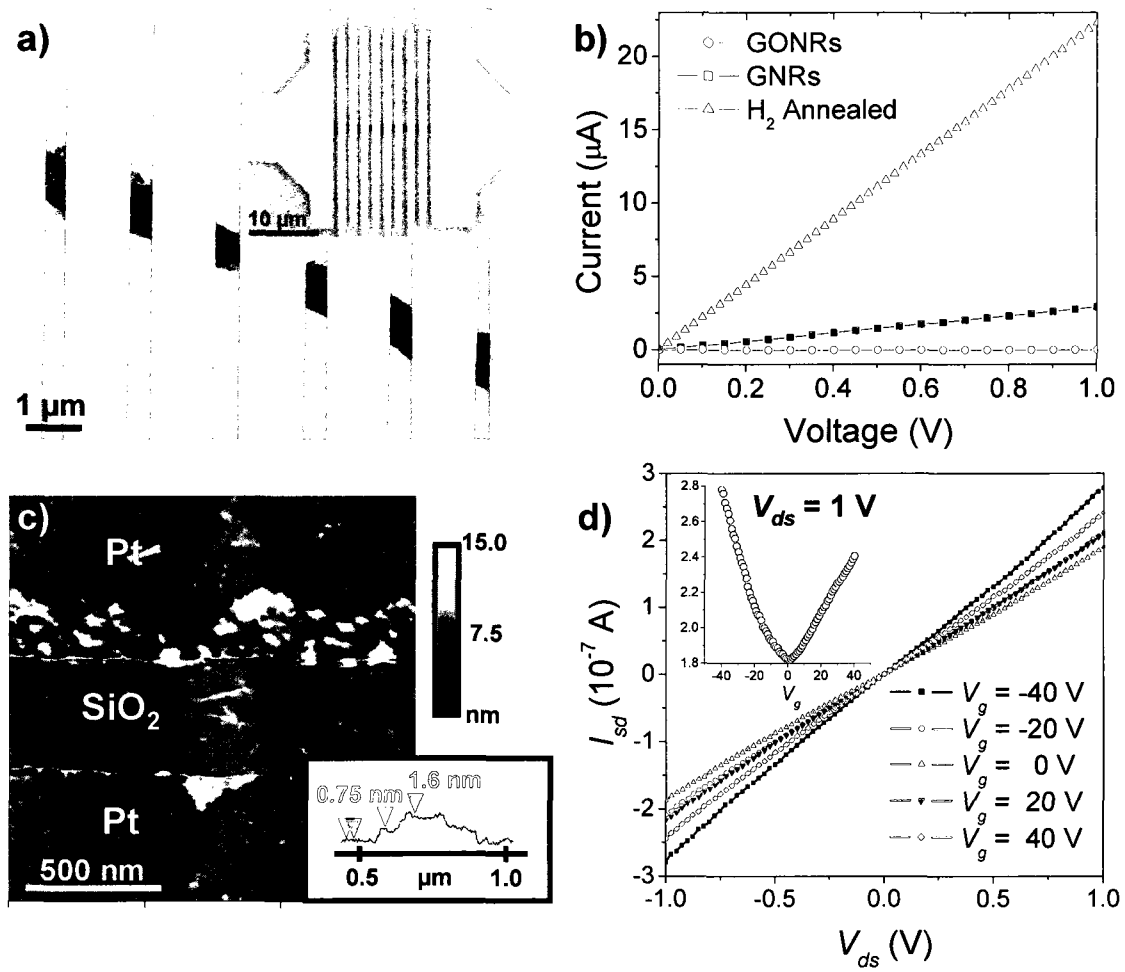

Figure 5.7. a) SEM image of a multi-terminal device based on a multilayer (~10-nm-thick) stack of GNRs with Pt electrodes. Inset is a larger image of a similar device. b) *I-V* curves for three different types of devices: GONRs, GNRs and H_2-annealed GNRs (~300 nm wide, 10 nm thick (AFM) with a channel length ~500 nm; characteristic of the >10 devices measured for each of the three states). c) AFM image of another device based on a N_2H_4-reduced and annealed (H_2/Ar at 300 °C for 10 min) bilayer GNR which shows that the ribbon consists of two overlapping nanoribbons in the SiO_2 channel region. Typical height profile (inset) across this GNR shows steps of about 0.75 nm, which correspond to individual graphene sheets. These sheets overlap in the middle resulting in a height of

~1.6 nm. d) Source-drain current (I_{sd}), source-drain voltage (V_{ds}) and gate voltage (V_g) dependencies for the device shown in (c); p-doped Si was used as a back gate.

5.2.6 Preparation of Narrow GONRs from SWCNTs

$KMnO_4$ treatment of single-walled carbon nanotubes (SWCNTs) yielded similar results as those from MWCNTs – "narrow" nanoribbons appear to be produced via longitudinal unzipping, though they may also be shortened in the process (see AFM image, Figure 5.8b). The SWCNTs were purified (pSWCNTs) before use to lower the catalyst content.[36] The pSWCNTs were subjected to the same conditions as MWCNTs to bring about ribbon formation with the following exceptions: 25 vol% oleum (H_2SO_4, 20% fuming SO_3) was used to suspend pSWCNTs prior to oxidation, and the reaction was typically complete after heating at 55 °C for an additional 45 min.

TEM and AFM images of narrow GONRs produced with $KMnO_4$ in H_2SO_4 are given in Figure 5.8. Compared to the starting SWCNTs (Figure 5.8a) with their 1-2 nm heights as individuals and 5-10 nm heights when bundled, the resulting nanoribbon structures appear to be flatter, less bundled, and with larger widths. The narrow GONRs from SWCNTs appear more twisted and aggregated than the MWCNT-derived samples.

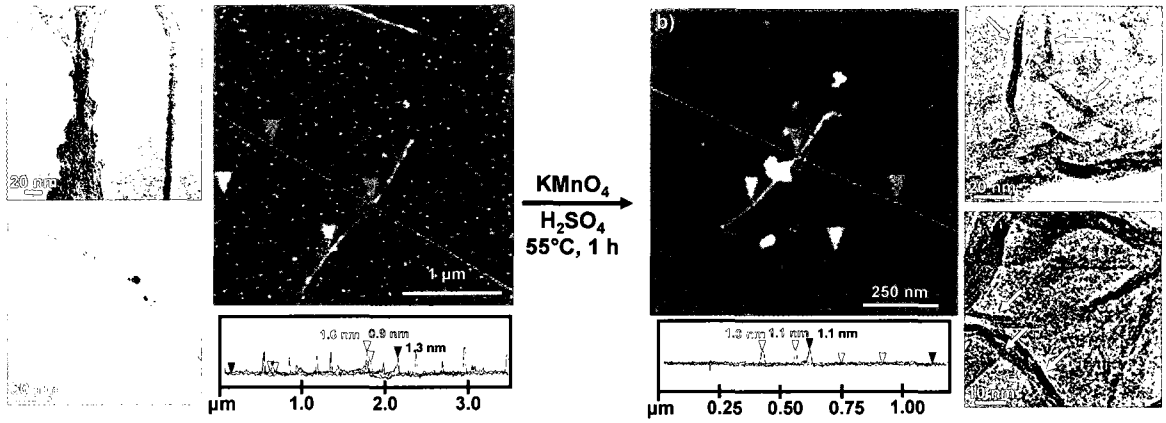

Figure 5.8. a) Starting material pSWCNTs produced via the HiPco process. The TEM images (left) consist of bundled pSWCNT structures that are 5-10 nm in diameter with residual Fe catalyst particles. The SWCNT sample used in the AFM image (right) was taken from the same HiPco batch and suspended as individuals in SDS surfactant (via previously reported procedures)[37] so that accurate height data could be obtained on single tubes. The average height of the single SWCNT shown is ~1.3 nm. The dot structures are traces of surfactant; most of the surfactant was removed with isopropanol during spin-coating of the AFM sample. b) Material resulting after treatment with $KMnO_4$ in sulfuric acid at 55 °C for 45 min. The AFM image (left) with a decreased average height (~1 nm). TEM images (right) reveal that the GONRs remain closely associated to one another, intertwined and mostly stacked in a "bowl of noodles" arrangement. Flat narrow nanoribbons, stacked and unstacked, with diameters of ~3-5 nm (noted by white arrows) and lengths < 1 μm, can be identified.

Characterization of the narrow GONRs before and after chemical reduction with N_2H_4 (as described in Section 5.4.3) to form narrow GNRs was carried out with UV-vis, ATR-IR, XPS, and Raman spectroscopy (Figure 5.9). The UV absorption spectrum (Figure 5.9a) of narrow GNRs shows a similar bathochromic shift of the absorption maximum and hyperchromicity in the absorption across the entire spectral range after reduction as the wide GNRs formed from MWCNTs (see Figure 5.5c), but is less pronounced. The ATR-IR spectra of narrow GONRs and GNRs compared to the starting material pSWCNTs is given in Figure 5.9b. It is apparent that the narrow GONRs retain water as demonstrated in the broad –OH absorption. After reduction, water retention and the amount of functionality is decreased, but not eliminated as observed for the MWCNT-derived ribbons due to much higher proportion of carboxylic acids to total carbon atoms contained on the edges of the narrow nanoribbons as compared to the wider nanoribbons.

The XPS C1s spectra of narrow GONRs and GNRs compared to the starting material pSWCNTs is given in Figure 5.9c with the corresponding atomic concentrations in Figure 5.9d. The signals at 286 eV and 287 eV correspond to C-O and C=O, respectively. The shoulder at 289 eV is assigned to carboxy groups. After reduction, the 286 eV and 287 eV peaks become much smaller demonstrating significant deoxygenation of the nanoribbons by N_2H_4. As reported for CCG, the most dominant peak after chemical reduction is the C-C peak (284.8 eV).[32] The atomic concentration values support this, as oxygen loss is observed upon reduction (34 to 23%). The Raman spectra of narrow GONRs,

GNRs, and pSWCNTs are shown in Figure 5.9e. Both GONRs and GNRs have a high D:G ratio compared to the starting material pSWCNTs, and is consistent with declining sp^2 conjugation and addition of oxygen-containing functionalities. The high D:G ratio remains after hydrazine reduction and heating to 950 °C under argon, and can be attributed to the large effect of the edges (which contain oxygen-functionalities not eliminated upon reduction) in narrow GNRs. The enlarged radial breathing mode region (RBMs, Figure 5.9e bottom right) illustrates that such SWCNT-characteristic peaks are not present after exposure to the oxidizing conditions which indicates no tube structures remain.[38]

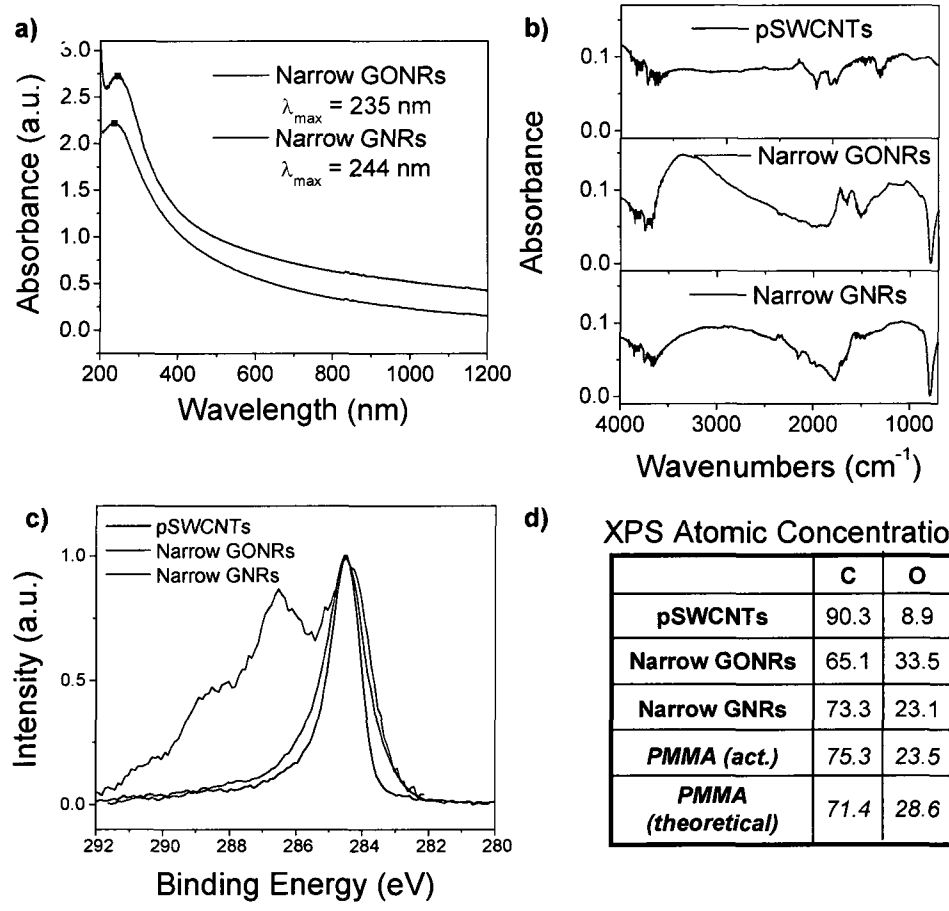

XPS Atomic Concentrations (%)

	C	O	N
pSWCNTs	90.3	8.9	0.8
Narrow GONRs	65.1	33.5	1.3
Narrow GNRs	73.3	23.1	3.5
PMMA (act.)	*75.3*	*23.5*	*1.2*
PMMA (theoretical)	*71.4*	*28.6*	*0*

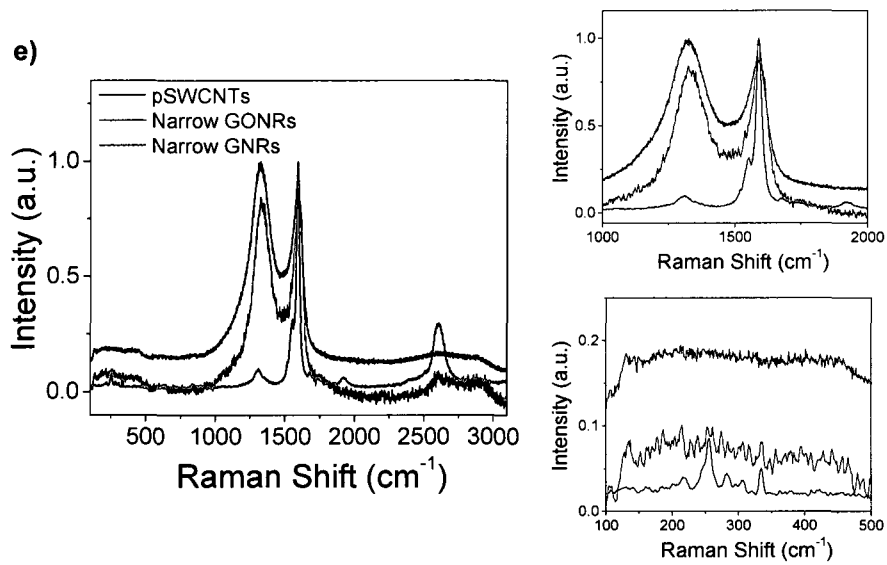

Figure 5.9. a) Changes in the UV spectrum of an aqueous solution of narrow GONRs (red) before and after reduction with N_2H_4 (narrow GNRs, blue). b) ATR-IR of narrow GONRs (red), GNRs (blue) compared to SWCNT starting material (black). c) Superimposed XPS C1s spectra of the narrow GONRs (red) and GNRs (blue) compared to pSWCNTs (black). d) XPS-determined atomic concentrations of narrow GONRs and GNRs compared to the pSWCNTs. A poly(methyl methacrylate) (PMMA) standard was employed to determine the accuracy of the measurement. The nitrogen content can be due to hydrazine adducts and physisorbed N_2.[39] e) The Raman spectra (633 nm laser excitation) of narrow GONRs (red) and GNRs (blue) compared to pSWCNTs (black). Enlarged portions of the D and G bands (upper right) and radial breathing modes (RBMs, bottom right) are also given.

5.3 Conclusions

A bulk method for producing high aspect ratio, straight-edge GNRs from longitudinally unzipping the sidewalls of MWCNTs via solution-based oxidation was presented. The level of oxidation and MWCNT sidewall exfoliation can be controlled with the amount of $KMnO_4$ oxidizing agent added to the reaction mixture. The chemical structure of as-produced GONRs resembles that of GO, and can be effectively reduced to GNRs upon treatment with N_2H_4 with restoration of electrical conductivity. Preliminary results also indicate that the ribbon-formation process can be extended to SWCNTs, though further investigation is needed. The high yield production of GNRs using this simple, scalable technique is envisioned for applications in composite materials, sensors, catalysts, and electronic components.

5.4 Experimental

MWCNTs, were used as received from Mitsui & Co., Ltd. (Lot No. 05072001K28). SWCNTs used were produced via the HiPco process[40] (batch number 187.4) by the Carbon Nanotechnology Laboratory at Rice University. The remaining chemicals were purchased from Sigma-Aldrich and used as received, except for the concentrated sulfuric acid (Fisher Scientific) and oleum (Alfa Aesar). Deionized (DI) water (18 MΩ resistivity) obtained from a NanoPure system (Barnstead, Dubuque, IA USA) was used throughout this work.

5.4.1 GONR Synthesis

In a typical procedure, MWCNTs or SWCNTs (150 mg, 12.5 mequiv of carbon) were suspended in 150 mL conc H_2SO_4 for a minimum of 1 h up to 12 h. $KMnO_4$ (750 mg, 4.75 mmol) was then added and the mixture allowed to stir for 1 h at room temperature. For SWCNTs, ~30 mL oleum was also added to aid in exfoliation of the SWCNT bundles and stirred at room temperature overnight. The reaction was then heated in an oil bath at 55 °C for 30 min. The progress of the reaction was monitored by preparing 2 test tubes, one containing 1 mL of DI water and 2-3 drops of hydrogen peroxide (30%), and one containing 1 mL water only. 4-5 drops of the reaction mixture were added to the test tubes and bath sonicated for 3 min. The color and dispersibility of the solution in the test tube containing the hydrogen peroxide was noted; if the solution was yellow/brown and the solid broke up into very small pieces, the reaction was complete. The other test tube was used to check the level of permanganate consumption; if a dark purple/blue hue was observed (like that seen when $KMnO_4$ is dissolved in water), the reaction was not complete. Alternatively, a solution with a red hue signified the presence of manganese (IV), indicating permanganate consumption and a complete reaction. It was also important to note the color of the reaction mixture itself; the color went from black to dark brown with the green color of permanganate in acid disappearing by reaction completion. If the reaction had not completed after 30 min at 55 °C, the temperature was increased to 65 °C. When the reaction temperature stabilized at 65 °C, the reaction status was checked again via the above test tube procedure. Continued heating at 65 °C

was needed if the permanganate was not entirely consumed. When the reaction appeared nearly complete or complete, the temperature was increased to 70 °C and the solution was allowed to stabilize. Upon stabilization at 70 °C, the flask was removed from the heat source, the mixture was allowed to cool to room temperature and was then poured onto 400 mL of ice containing 5 mL of 30% H_2O_2 (to prevent precipitation of insoluble MnO_2). After vacuum filtration through a PTFE membrane (5.0 μm pore size), the solid was removed and stirred in 150 mL water for 30 min, followed by bath sonication (Cole Parmer ultrasonic cleaner, Model 08849-00) for 15 min. The material was then flocculated by addition of 20 vol% concentrated HCl (30 mL). The suspension was then filtered through a PTFE membrane (0.45 μm pore size). The filter cake product was removed and stirred in 150 mL ethanol for 30 min, followed by bath-sonication (Cole Parmer ultrasonic cleaner, Model 08849-00) for 15 min. The material was flocculated by addition of 100 vol% ether (150 mL) followed by filtration through a PTFE membrane (0.45 μm pore size). The filter cake product was washed 2× with ether (50 mL each) and dried in vacuo to afford 321 mg of GONRs. Shortened ribbons (Figure 5.1b) were formed from an aqueous solution of washed nanoribbons that were tip-sonicated at 30 W power (Misonix Sonicator 3000) for a total of 30 min (2 min on, 1 min off so that the on time totaled 30 min).

5.4.2 Stepwise Oxidation

The stepwise oxidation of MWCNTs was performed by first running the reaction, under the conditions specified above, with a 1:1 mass ratio of

$KMnO_4$:MWCNT (denoted sample I, least oxidized). After 1 h at 55 °C, approximately 1/5 volume of the reaction mixture was separated and worked up as outlined above. The remaining portion was then treated with 100 wt% $KMnO_4$ (relative to the portion of MWCNTs remaining) and allowed to react another 1 h at 55 °C. After separating 1/4 volume of the reaction mixture to be worked up, the rest was subjected to another portion of 100 wt% $KMnO_4$. The process was repeated until the final batch of ribbons was exposed to a total of 500 wt% $KMnO_4$ (denoted sample V, most oxidized, Figure 5.3e).

5.4.3 Reduction of GONRs

Reduction in aqueous N_2H_4 can be done with or without SDS surfactant. To introduce the SDS surfactant, 50 mg of the GONRs were homogenized (IKA T-25 digital ULTRA-TURRAX® disperser with 18 G dispersing element, 7000 rpm) in 250 mL of 1 wt% aqueous SDS solution for 1 h. The suspension was then cup sonicated (Cole Parmer Ultrasonic Processer, 75% power) for 10 min and filtered through a 5 cm plug of glass wool. If SDS is not present, 50 mg of GONRs were dissolved in 250 mL nanopure water. In both cases, 150 mL of the nanoribbon solution was covered by a 5 mm layer of silicone oil in an Erlenmeyer flask. To this solution, 150 µL of concentrated NH_4OH (2.22 mmol) was added followed by 150 µL of $N_2H_4 \cdot H_2O$ (98%, 3.03 mmol). The oil was added to eliminate the air-water interface that causes agglomeration of the reduced ribbons as water evaporates.[28] The reaction mixture was heated at 95 °C for 1 h in a gently boiling water bath (no stirring). Excess N_2H_4 was removed by dialysis

(CelluSep H1 regenerated cellulose tubular membrane, nominal molecular weight 5000, 400 mm width) for 24 h in 1% NH_4OH. Filtering and drying in vacuo afforded 23.2 mg of GNRs. Therefore the overall weight conversion efficiency from MWCNTs to the GNRs is 215% and 46% for the two steps yielding 99%.

5.4.4 Device Fabrication

Fabrication of graphene devices was performed by tracking individual GNRs on the surface of 200 nm-thick dielectric SiO_2-covered, highly-doped Si substrates by scanning electron microscopy (JEOL-6500 microscope) followed by patterning 20-nm-thick Pt contacts via standard e-beam lithography. Prior to testing, the devices used to produce the data in Figure 5.7d were annealed in H_2/Ar (1:1, <1 atm) atmosphere at 300 °C for 10 min. The electrical properties were tested using a probe station (Desert Cryogenics TT-probe 6 system) under vacuum with a chamber base pressure below $1x10^{-5}$ mm Hg. The *IV* data were collected using an Agilent 4155C semiconductor parameter analyzer.

5.4.5 Sample Analysis

TEM imaging was performed on a JEOL 2010. Samples were prepared by dispersing the nanoribbons in a 1:1 mixture of ethanol:water and dropped onto 300 mesh holey lacey carbon grids on copper support (Ted Pella, Inc.). AFM images were obtained with a Nanoscope IIIa (Digital Instruments/Veeco Metrology, Inc.), operating in tapping mode, using 1-10 Ohm-cm phosphorus (n) doped Si tips (Veeco, MPP-11100-140) at a scan rate of 2 Hz and 512 x 512

resolution. Samples for AFM analysis were prepared by spin coating aqueous solutions of GONRs at 3000 RPM onto a freshly cleaved mica surface (Ted Pella, Inc.) and rinsed with DI water and 2-isopropanol.

UV-vis spectra were obtained on a Shimadzu UV-3101 PC with samples contained in 1 mL quartz cuvettes. FT-IR was acquired on a Nicolet FTIR Infrared Microscope with an Attenuated Total Reflectance (ATR) attachment. XPS was performed on a PHI Quantera SXM Scanning X-ray Microprobe with a pass energy of 26.00 eV, 45° takeoff angle and a 100 μm beam size. TGA (Q50, TA Instruments) was performed from room temperature to 950 °C at 10 °C/min under argon. Raman spectroscopy was performed on a Renishaw Raman scope using a 633 nm He-Ne laser. The XRD measurements were carried out with a Rigaku diffractometer (Cu $K\alpha$ radiation, X-ray wavelength λ = 1.5406 Å, operating at 40 keV, cathode current of 40 mA and scan rate of 1 deg/min). BET surface area analysis was performed at 77 K on a Quantachrome Autosorb-1 Physisorption system using N_2 as the sorption gas.

5.5 References

1. Geim, A. K.; Novoselov, K. S. *Nature Mater.* **2007**, *6*, 183-191.
2. Novoselov, K. S.; Geim, A. K.; Morozov, S. V.; Jiang, D.; Katsnelson, M. I.; Grigorieva, I. V.; Dubonos, S. V.; Firsov, A. A. *Nature* **2005**, *438*, 197-200.
3. Zhang, Y.; Tan, Y.-W.; Stormer, H. L.; Kim, P. *Nature* **2005**, *438*, 201-204.
4. Areshkin, D. A.; Gunlycke, D.; White, C. T. *Nano Lett.* **2007**, *7*, 204-210.

5. Nakada, K.; Fujita, M.; Dresselhaus, G.; Dresselhaus, M. S. *Phys. Rev. B: Condens. Matter* **1996**, *54*, 17954-17961.

6. Son, Y.-W.; Cohen, M. L.; Louie, S. G. *Phys. Rev. Lett.* **2006**, *97*, 216803/216801-216803/216804.

7. Han, M. Y.; Oezyilmaz, B.; Zhang, Y.; Kim, P. *Phys. Rev. Lett.* **2007**, *98*, 206805/206801-206805/206804.

8. Chen, Z.; Lin, Y.-M.; Rooks, M. J.; Avouris, P. *Physica E* **2007**, *40*, 228-232.

9. Schniepp, H. C.; Li, J.-L.; McAllister, M. J.; Sai, H.; Herrera-Alonso, M.; Adamson, D. H.; Prud'homme, R. K.; Car, R.; Saville, D. A.; Aksay, I. A. *J. Phys. Chem. B* **2006**, *110*, 8535-8539.

10. Rollings, E.; Gweon, G. H.; Zhou, S. Y.; Mun, B. S.; McChesney, J. L.; Hussain, B. S.; Fedorov, A. V.; First, P. N.; de Heer, W. A.; Lanzara, A. *J. Phys. Chem. Solids* **2006**, *67*, 2172-2177.

11. Li, X.; Wang, X.; Zhang, L.; Lee, S.; Dai, H. *Science* **2008**, *319*, 1229-1232.

12. Jiao, L.; Zhang, L.; Wang, X.; Diankov, G.; Dai, H. *Nature* **2009**, *458*, 877-880.

13. Yang, X.; Dou, X.; Rouhanipour, A.; Zhi, L.; Raeder, H. J.; Muellen, K. *J. Am. Chem. Soc.* **2008**, *130*, 4216-4217.

14. Campos-Delgado, J.; Romo-Herrera, J. M.; Jia, X.; Cullen, D. A.; Muramatsu, H.; Kim, Y. A.; Hayashi, T.; Ren, Z.; Smith, D. J.; Okuno, Y.;

Ohba, T.; Kanoh, H.; Kaneko, K.; Endo, M.; Terrones, H.; Dresselhaus, M. S.; Terrones, M. *Nano Lett.* **2008**, *8*, 2773-2778.

15. Saito, T.; Matsushige, K.; Tanaka, K. *Physica B* **2002**, *323*, 280-283.
16. Barone, V.; Hod, O.; Scuseria, G. E. *Nano Lett.* **2006**, *6*, 2748-2754.
17. Hernandez, Y.; Nicolosi, V.; Lotya, M.; Blighe, F. M.; Sun, Z. Y.; De, S.; McGovern, I. T.; Holland, B.; Byrne, M.; Gun'ko, Y. K.; Boland, J. J.; Niraj, P.; Duesberg, G.; Krishnamurthy, S.; Goodhue, R.; Hutchison, J.; Scardaci, V.; Ferrari, A. C.; Coleman, J. N. *Nature Nanotech.* **2008**, *3*, 563-568.
18. Son, Y.-W.; Cohen, M. L.; Louie, S. G. *Nature* **2006**, *444*, 347-349.
19. Liang, G.; Neophytou, N.; Nikonov, D. E.; Lundstrom, M. S. *IEEE Trans. Electron Devices* **2007**, *54*, 677-682.
20. Wang, X.; Ouyang, Y.; Li, X.; Wang, H.; Guo, J.; Dai, H. *Phys. Rev. Lett.* **2008**, *100*, 206803/206801-206803/206804.
21. Li, J.-L.; Kudin, K. N.; McAllister, M. J.; Prud'homme, R. K.; Aksay, I. A.; Car, R. *Phys. Rev. Lett.* **2006**, *96*, 176101/176101-176101/176104.
22. Ajayan, P. M.; Yakobson, B. I. *Nature* **2006**, *441*, 818-819.
23. Wolfe, S.; Ingold, C. F.; Lemieux, R. U. *J. Am. Chem. Soc.* **1981**, *103*, 938-939.
24. Banoo, F.; Stewart, R. *Can. J. Chem.* **1969**, *47*, 3199-3205.
25. Endo, M. *Chemtech* **1988**, *18*, 568-576.
26. Hummers, W. S., Jr.; Offeman, R. E. *J. Am. Chem. Soc.* **1958**, *80*, 1339.
27. Lerf, A.; He, H.; Forster, M.; Klinowski, J. *J. Phys. Chem. B* **1998**, *102*, 4477-4482.

28. Li, D.; Mueller, M. B.; Gilje, S.; Kaner, R. B.; Wallace, G. G. *Nature Nanotech.* **2008**, *3*, 101-105.

29. Stankovich, S.; Dikin, D. A.; Piner, R. D.; Kohlhaas, K. A.; Kleinhammes, A.; Jia, Y.; Wu, Y.; Nguyen, S. T.; Ruoff, R. S. *Carbon* **2007**, *45*, 1558-1565.

30. Bourlinos, A. B.; Gournis, D.; Petridis, D.; Szabo, T.; Szeri, A.; Dekany, I. *Langmuir* **2003**, *19*, 6050-6055.

31. Eda, G.; Fanchini, G.; Chhowalla, M. *Nature Nanotech.* **2008**, *3*, 270-274.

32. Stankovich, S.; Piner, R. D.; Chen, X.; Wu, N.; Nguyen, S. T.; Ruoff, R. S. *J. Mater. Chem.* **2006**, *16*, 155-158.

33. Hung, C.-c.; Corbin, J. *Carbon* **1999**, *37*, 701-705.

34. Rangel, N. L.; Sotelo, J. C.; Seminario, J. M. *J. Chem. Phys.* **2009**, *131*, 031105.

35. Novoselov, K. S.; Geim, A. K.; Morozov, S. V.; Jiang, D.; Zhang, Y.; Dubonos, S. V.; Grigorieva, I. V.; Firsov, A. A. *Science* **2004**, *306*, 666-669.

36. Chiang, I. W.; Brinson, B. E.; Huang, A. Y.; Willis, P. A.; Bronikowski, M. J.; Margrave, J. L.; Smalley, R. E.; Hauge, R. H. *J. Phys. Chem. B* **2001**, *105*, 8297-8301.

37. O'Connell, M. J.; Bachilo, S. M.; Huffman, C. B.; Moore, V. C.; Strano, M. S.; Haroz, E. H.; Rialon, K. L.; Boul, P. J.; Noon, W. H.; Kittrell, C.; Ma, J.; Hauge, R. H.; Weisman, R. B.; Smalley, R. E. *Science* **2002**, *297*, 593-596.

38. Saito, R.; Takeya, T.; Kimura, T.; Dresselhaus, G.; Dresselhaus, M. S. *Phys. Rev. B* **1998**, *57*, 4145-4153.

39. Kang, E. T.; Neoh, K. G.; Tan, K. L. *Adv. Polym. Sci.* **1993**, *106*, 135-190.

40. Nikolaev, P.; Bronikowski, M. J.; Bradley, R. K.; Rohmund, F.; Colbert, D. T.; Smith, K. A.; Smalley, R. E. *Chem. Phys. Lett.* **1999**, *313*, 91-97.

5.6 Experimental Contributions

My contribution to the work presented in this chapter is as follows: assisted in synthesis of the GONRs and GNRs, characterization of the material by TEM, AFM, ATR-IR, TGA, UV-vis, and Raman spectroscopy. Dmitry Kosynkin developed the synthesis of the GONRs and assisted in interpretation of the data analysis. Alexander Sinitskii fabricated and tested the GNR electronic devices and prepared Figure 5.7. Jay Lomeda collected the XRD data and was involved in many discussions of this work. Ayrat Dimiev took the SEM images, and B. Katherine Price assisted in AFM imaging. Wenhua Guo assisted in collecting HR-TEM images and FFT diffractograms of the GNR edges.

5.7 Appendix 2

5.7.1 Additional Imaging

Supplementary TEM and SEM images of the MWCNT starting material and GONRs are shown in Figures 5.10 and 5.11. Additionally, Figures 5.11a-b highlight the high yield of the nanoribbon-formation process; Figure 5.11a is a low resolution TEM image which shows single- and few-layer GONRs overlaid with little MWCNT structure remaining while Figure 5.11b is an SEM image of the bulk powder sample which also corroborates high MWCNT to nanoribbon conversion.

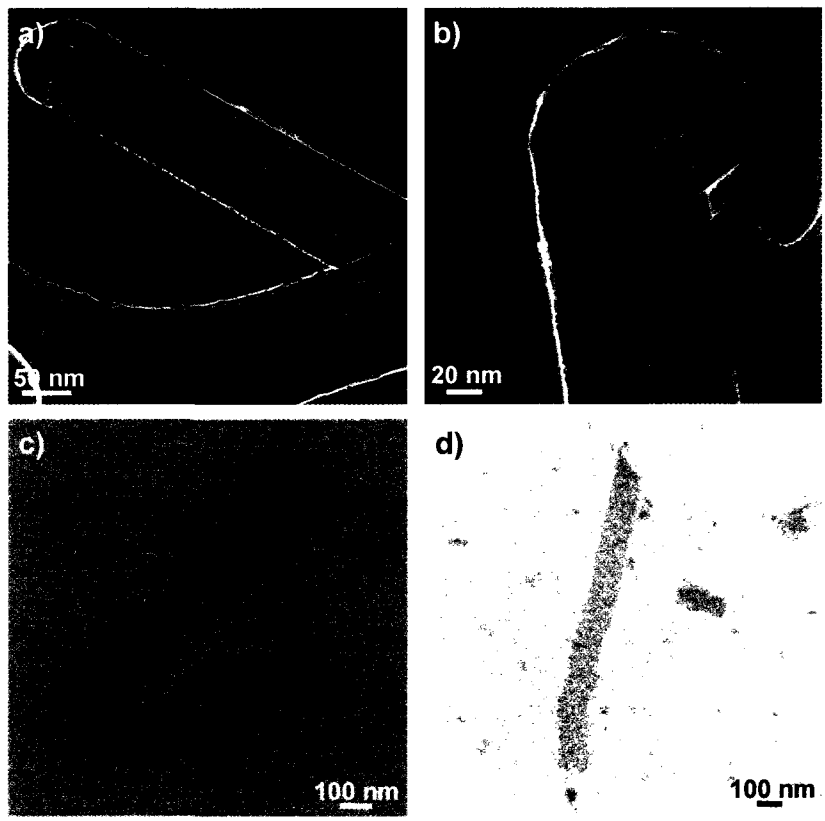

Figure 5.10. a-b) TEM images of MWCNTs as-received from Mitsui, Inc. The average diameter is 40-80 nm with ~30 inner tube walls; the tips do not contain catalyst particles. c-d) SEM images of GONRs on a silicon surface.

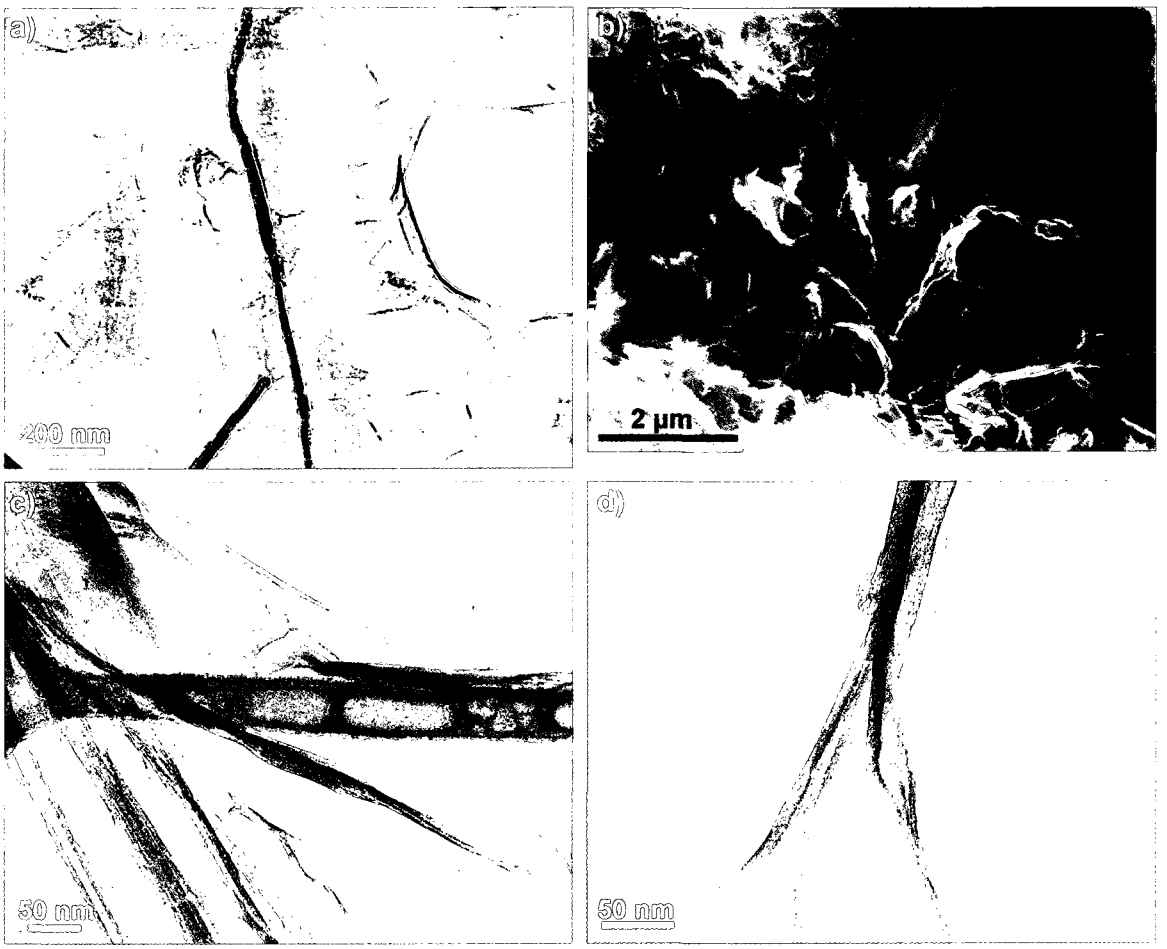

Figure 5.11. a) Overview TEM image that highlights the high yield of the process. Very little MWCNT remains; the majority of the sample is overlaid GONRs with straight edges. b) SEM image of a bulk GONR sample which also illustrates the high yield of the process by demonstrating nanotube-free material. c) GONRs; the bottom left portion shows some remaining MWCNT. d) A MWCNT in the process of unzipping.

5.7.2 Additional Analysis of GONRs and GNRs

a) XPS Atomic Concentrations (%)

	C	O	N
MWCNT	97.9	2.1	0
GONRs	58.0	41.8	0.2
GNRs	81.7	16.1	2.1
PMMA (act.)	*74.2*	*25.2*	*0.6*
PMMA (theoretical)	*71.4*	*28.6*	*0*

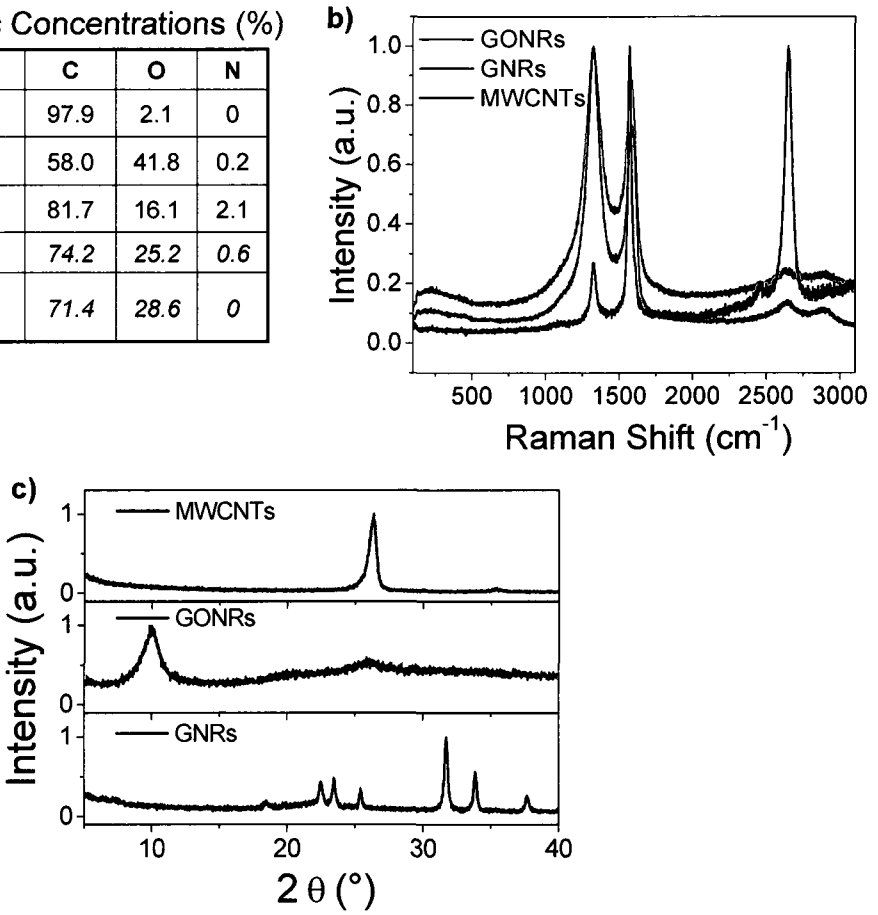

Figure 5.12. a) XPS determined atomic concentrations of GONRs and GNRs compared to the MWCNT starting material which corresponds to the data shown in Figure 5.6b. A large loss of oxygen upon reduction (from 42 to 16%) is evident. A poly(methyl methacrylate) (PMMA) standard was employed to determine the accuracy of the measurement. The nitrogen content of the GNRs (2.1%) can be attributed to hydrazine adducts and physisorbed N_2.[35] b) The Raman spectra of GONRs before (red) and after reduction (blue) compared to the MWCNT starting material (black). The behavior is very similar to that observed for GO and

reduced GO[29] with a broadened G peak (1594 cm^{-1}) after oxidation along with the appearance of the D band at 1363 cm^{-1}. This indicates the reduction in size of the in-plane sp^2 carbon domains due to the oxidation. After reduction, both G and D bands are still prominent, but are better resolved, with an increased D:G intensity ratio compared to that of the oxidized form. This is expected and is caused by a decrease in the average size of the sp^2 domains upon reduction compared to the pristine material, but are more numerous in number than the GO sample.[29] c) XRD analysis showing the structure of the GNRs (blue trace) compared to the GONRs (red trace) and MWCNT starting material (black trace). The d spacing of MWCNT is ~3.4 Å (calculated using the Bragg equation with a program in the XRD software) which closely resembles graphite. Upon oxidation to GONRs, the d spacing increased to 8.8 Å which is close to values obtained for GO. The GNRs, however, exhibit several peaks which are probably due to the presence of multiple crystalline orientations that form upon aggregation.

5.7.3 HR-TEM Edge Analysis of GNRs

In order to determine the arrangement of the carbon atoms at the edge of the ribbons (i.e. armchair or zigzag), HR-TEM imaging was used to study GNRs at high magnification. It is hypothesized that both edge configurations are present, with jagged lines in some areas. The criteria for choosing GNR edges to image were that they be single- or double-layered and exhibit minimal folding along the edges. To determine the arrangement of the carbon atoms at the edge, a clear hexagonal Fourier transform diffractogram (FFT) with six distinct spots (characteristic of graphene) must be obtained so that the inverse FFT will result in an accurate carbon atom map. As shown in Figure 5.13a, such FFTs (inset) are readily obtained for inner regions of the GNRs because these areas are more graphene-like with fewer defects. It is more difficult, however, to obtain concise FFTs near the edges (Figure 5.13b) due to the increased number of defects and edge-folding. This may be alleviated by annealing the sample (~900 °C under Ar/H_2) once deposited onto a TEM grid inert to high temperatures.

An example of a straight GNR edge with a suitable double-layer FFT for inverse FFT atom mapping is shown in Figure 5.13c-d. Unfortunately, the resolution was not high enough to unambiguously determine the edge state of the region. As shown in Figures 5.13e-f, zigzag or armchair configuration cannot be differentiated. An aberration-corrected TEM microscope is necessary to achieve the level of detailed imaging that is required for mapping the atomic arrangement of GNR edges.

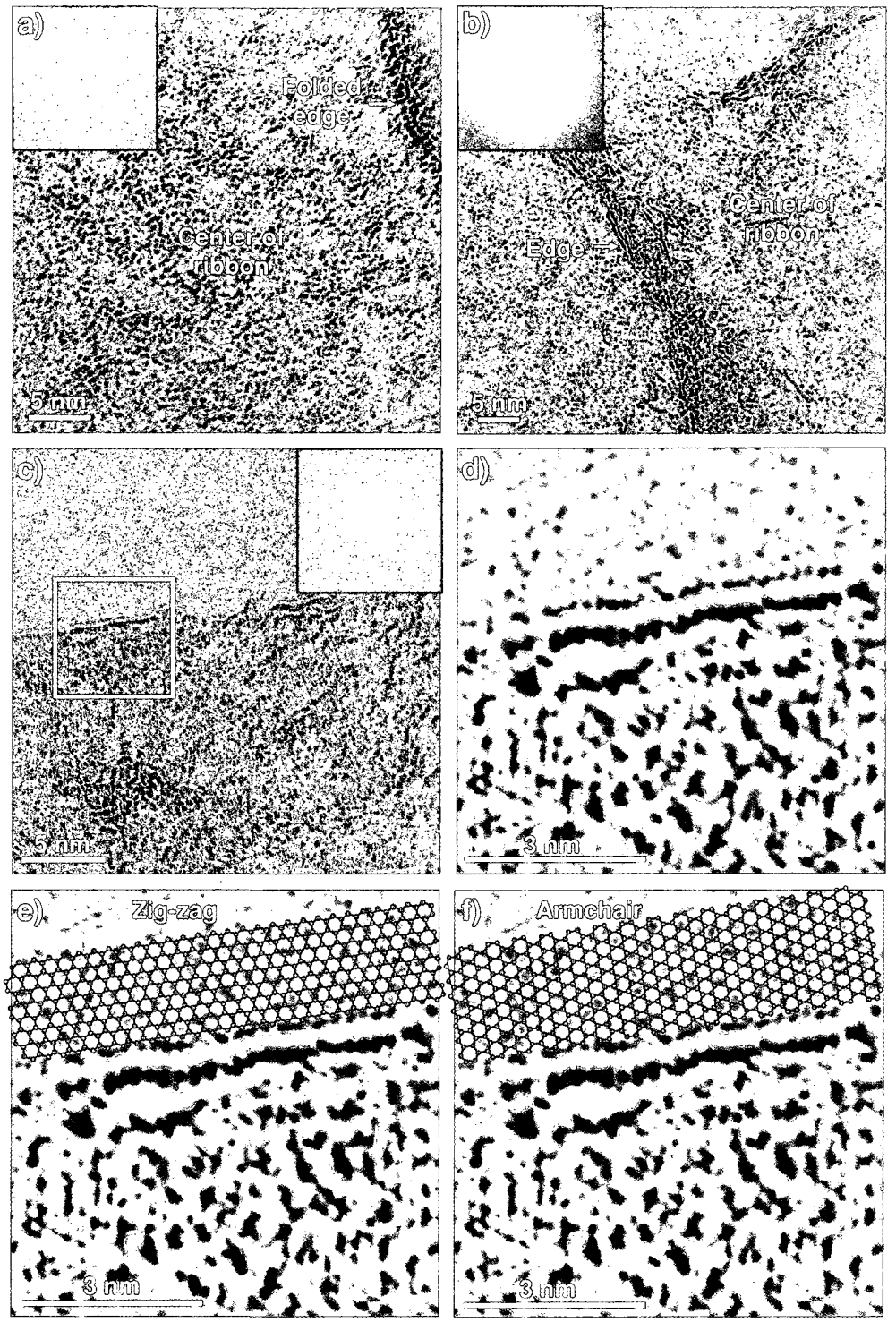

Figure 5.13. a) HRTEM image of a GNR center near a folded edge. The FFT (inset) shows a hexagonal pattern with six distinct spots, characteristic of

graphene. b) HRTEM image of a GNR edge with a more diffuse FFT pattern (inset). This is due the presence of edge defects. c) A GNR edge with a linear region (boxed). The FFT of the boxed region is shown in the inset; a double-hexagon pattern is given because two GNR layers are present. d) Inverse FFT image of the boxed region in (c). With concise FFT patterns, the inverse FFT should give an accurate atomic map of a crystalline structure based on changes in electron density. e-f) Zigzag and armchair graphene edges (sized-to-scale) are aligned with the edge mapped in (d). The resolution is not high enough to accurately determine the atomic configuration of this particular edge.

Chapter 6

Synthesis and Optimization of Low-Defect Graphene Oxide Nanoribbons from MWCNTs

6.1 Introduction

Chapter 5 presented a high-yielding procedure for production of large quantities of single and few-layer graphene nanoribbons (GNRs) through oxidative longitudinal unzipping of multi-walled carbon nanotubes (MWCNTs) in sulfuric acid.[1] It was found that potassium permanganate ($KMnO_4$) is an unusually selective oxidant for longitudinal cleavage of MWCNTs; however, other strong oxidants based on high oxidation states of transition metals that give *cis*-oxidation of double bonds (i.e. OsO_4 and FeO_4^{2-}) are expected to affect the same longitudinal unzipping.[1] The GNRs obtained from MWCNTs possess straight edges and high aspect ratios with no significant shortening of the parent tubes. Since the unzipping process is oxidative, the composition is similar to graphene oxide (GO), therefore these nanoribbons are termed graphene oxide nanoribbons (GONRs). Both GO and GONRs possess oxygen-containing functionalities such as carbonyls, carboxyls, epoxides, and hydroxyls at the edges and surface[2] and are highly soluble in water and polar organic solvents. It was also found that the degree of permanganate-induced cleavage can be controlled by adjusting the amount of oxidant used in the reaction. As with GO, the GONRs can be chemically reduced with hydrazine (N_2H_4) resulting in significantly lower oxygen content and restoration of much of the π-π conjugation, noted by recovery of electrical conductivity and a dramatic increase in absorption intensity across the entire UV-Vis region.

Among the GONRs produced using the previously described method,[1] it was observed that ribbons <100 nm wide were rarely observed in the product.

Since a high yield of MWCNT opening and subsequent exfoliation of the GONR layers is obtained, narrow GONRs <100 nm wide are most likely oxidatively consumed during the oxidation process. Excessive oxidation must occur that not only destroys the more reactive, narrow ribbons derived from the inner tubes, but also disrupts contiguous regions of the basal plane of the wider ribbons, causing holes of various shapes and sizes. These holes, which also form during the oxidation of graphite, have been identified as lattice distortions in the atomic structure after oxidation of graphite.[3] Upon chemical reduction of the oxygen functionalities (i.e. hydrazine treatment), the lattice distortions (such as holes) remain and cause substantially lower conductance and carrier mobilities in the reduction product of GO, termed chemically converted graphene (CCG), when compared to the conductance and mobility in exfoliation-derived graphene.[4] In addition, holes in the basal planes could be deleterious for applications relying on the tensile strength or gas impermeability of the material.

In this chapter, an improved method is described for the production of GONRs via longitudinal unzipping of MWCNTs that results in GONRs with fewer defects and/or holes on the basal plane, as well as maintaining narrow ribbons <100 nm wide and maximizing the high aspect ratio. Changes in the reaction conditions such as acid content, time, and temperature were investigated. The new, optimized method improves the selectivity of the oxidative unzipping presumably by in situ protection of the vicinal diols formed on the basal plane of graphene during the oxidation, and thereby prevents their over-oxidation to

diketones and the subsequent hole generation. The new material is termed extreme graphene oxide nanoribbons, or XGONRs.

6.2 Results and Discussion

6.2.1 Variations of Reaction Conditions for Nanoribbon Formation

In an effort to further understand the reaction mechanism and study the importance of each variable, a series of reactions was carried out with variations in the acid medium, temperature and time of the reaction. The reaction conditions and results are summarized in Table 6.1. Listed in the Table are the yield of the isolated product (wt%, relative to the weight of the starting MWCNTs), representative transmission electron microscopy (TEM) and scanning electron microscopy (SEM) images, C:O atomic concentration ratio determined by XPS, TGA wt% remaining at 250 and 950 °C under inert gas, λ_{max} as determined by UV of a dilute aqueous solution, and overall conclusions. The weight gain of the product, C:O XPS ratio, and TGA wt% together give an indication of the degree of oxidation; a highly oxidized sample will have an increase in weight of 50 – 140%, a low C:O ratio, and less weight remaining upon heating in the TGA, all due to the presence of oxygen-containing functional groups on the edges and basal plane. The UV λ_{max} indicates the level of π-conjugation remaining in the system, and hence relative degree of oxidation; highly conjugated graphene-like material will have a higher λ_{max} (~275 nm) while material with a disrupted π-network and greater number of sp^3 carbons will be hypsochromically shifted (λ_{max} ~235 nm).

All reactions used $KMnO_4$ as the oxidizing agent. Reaction **1** was carried out using the method previously published,[1] and is given as a reference for comparison. Reactions **2** – **5** were prepared under similar conditions with variations in the reaction time and temperature. Reactions **6** – **12** varied the acid medium, as well as the time or temperature.

Table 6.1. Summary of Reaction Conditions and Results

Reaction	Prep. Conditions[b]	Wt%[c]	TEM[d]	SEM[d]	C:O Ratio (XPS)	TGA[e] Wt% @ 250 °C	TGA[f] Wt% @ 950 °C	UV λ_{max}[g] (nm)	Conclusions
1[a]	5x $KMnO_4$ in H_2SO_4 22 °C → 70 °C 2 h	240	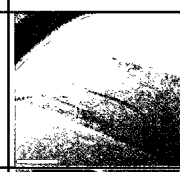	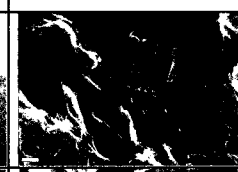	1.5:1	84	52	234	**Exfoliated Ribbons** Fully opened, high oxidation
2	5x $KMnO_4$ in H_2SO_4 22 °C, 2 h	126	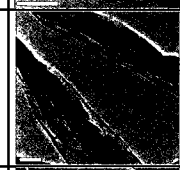		2.6:1	66	44	262	**Stacked Ribbons** Partially opened, light oxidation
3	5x $KMnO_4$ in H_2SO_4 60 °C, 2 h	205		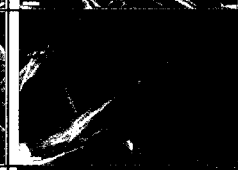	1.4:1	67	40	237	**Exfoliated Ribbons** Fully opened, high oxidation
4	5x $KMnO_4$ in H_2SO_4 85 °C, 2 h	195			1.5:1	63	31	233	**Exfoliated Ribbons** Fully opened, high oxidation
5	5x $KMnO_4$ in H_2SO_4 100 °C, 2 h	136	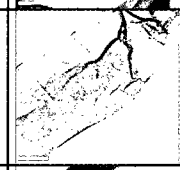		1.7:1	72	42	235	**Exfoliated Ribbons** Fully opened, high oxidation
6	5x $KMnO_4$ in 10% oleum 22 °C, 24 h	100			16.1:1	99	90	278	**Stacked Ribbons & Tubes** Partially opened, no oxidation
7	5x $KMnO_4$ in TFA/TFAA 22 °C, 24 h	100		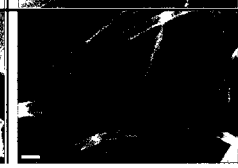	7.6:1	100	94	270	**Stacked Ribbons & Tubes** Minor unzipping, low oxidation

Reaction	Prep. Conditions[b]	Wt%[c]	TEM[d]	SEM[d]	C:O Ratio (XPS)	TGA[e] Wt% @ 250 °C	TGA[f] Wt% @ 950 °C	UV λ_{max}[g] (nm)	Conclusions
8	5× $KMnO_4$ in 1:1 H_2SO_4:TFA 22 °C, 24 h	134			4.0:1	89	74	265	**Stacked Ribbons & Tubes** Partial unzipping, low oxidation
9	5× $KMnO_4$ in 9:1 H_2SO_4:TFA 22 °C, 24 h	160	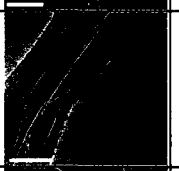		1.5:1	71	49	236	**Stacked Ribbons** Opened, high oxidation, not exfoliated
10	5× $KMnO_4$ in 9:1 H_2SO_4:TFA 65 °C, 2 h	165			1.8:1	66	43	245	**Exfoliated Ribbons** Fully opened, *high oxidation* with low defects
11	5× $KMnO_4$ in 9:1 H_2SO_4:H_3PO_4 65 °C, 2 h	178			1.6:1	63	42	235	**Exfoliated Ribbons** Fully opened, high oxidation with low defects
12	8× $KMnO_4$ in 9:1 H_2SO_4:H_3PO_4 65 °C, 2 h	143		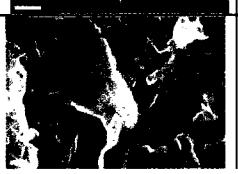	1.4:1	55	18	227	**Exfoliated Ribbons & Sheets** Fully opened, high oxidation

[a]Previously published conditions and results.[1]
[b]Weight equivalents of $KMnO_4$ relative to MWCNT weight in the starting material.
[c]100 signifies the product had no additional weight gain nor loss upon isolation, relative to starting weight of MWCNTs.
[d]All scale bars are 100 nm.
[e]Weight percent remaining at 250 °C by TGA at 10 °C/min under Ar.
[f]Weight percent remaining at 950 °C
[g]Recorded in water.
[h]The darker portion in the TEM micrograph is part of the lacey carbon grid.

Reactions **1** – **5** used concentrated H_2SO_4, 5 weight equivalents of $KMnO_4$ relative to the weight of MWCNTs (5× $KMnO_4$) and varied the reaction temperature from 22 °C to 100 °C. A moderate excess of $KMnO_4$ is used relative to the theoretical limit of 4.4× $KMnO_4$ for complete oxidation of all alkenes in the case of infinite size graphite crystals. The results indicate that elevated

temperatures are necessary for formation of GONRs when the reaction is run for 1 – 2 h. Exfoliated and highly oxidized GONRs are formed in all reactions where the temperature is maintained above 60 °C; however, ≥60 °C, the actual reaction temperature did not appear to have a significant effect on the resulting GONR properties. The products of reaction **1** and **3** – **4** all had ~100 wt% increase upon isolation of the product, a C:O ratio of ~1.5:1, and a TGA weight loss of 50 – 60 wt% at 950 °C. Reaction **2,** which was conducted at room temperature, resulted in stacked ribbons and partially opened tubes with lower levels of oxidation; the weight increase was only 26 wt%, and the C:O ratio nearly doubled at 2.6:1. In addition, the UV λ_{max} was bathochromically shifted from the other four reactions (262 nm compared to ~235 nm for the more exfoliated ribbons). Therefore, the necessity for heat to complete the exfoliation and oxidation is highlighted in this set of experiments.

Reaction **6** used 10% fuming sulfuric acid (oleum at 10% SO_3 content in H_2SO_4). The reaction was run with 5× $KMnO_4$ at room temperature for 24 h, but failed to produce exfoliated ribbons. It is hypothesized that the oleum decomposes $KMnO_4$ before it reacts with the MWCNTs. Strong acid environments, especially in the presence of SO_3, will cause decomposition of permanganate to afford ozone and oxygen.[5] SEM and TEM imaging reveal partially opened MWCNTs for the product of reaction **6** with minimal oxidation: no weight gain upon isolation, high C:O ratio of 16:1, TGA weight loss of 10 wt% at 950 °C, and a UV bathochromic shift (λ_{max} 278 nm) were observed.

Reaction **7** used a second acid, trifluoroacetic acid (TFA) in the presence of trifluoroacetic anhydride (TFAA, to scavenge traces of water) with 5× $KMnO_4$ at room temperature for 24 h. The resulting product was similar to that of reaction **6** – stacked ribbons with minor unzipping of the MWCNTs and low levels of oxidation. There was no weight gain upon isolation of the product, the C:O ratio was high (7.6:1), and the TGA weight loss low at only 6 wt%.

Reactions **8** – **11** used a series of conditions which varied the ratio of second acid as well as the reaction temperature; all reactions used 5× $KMnO_4$. Reactions **8** – **10** used TFA as the second acid while reaction **11** substituted phosphoric acid (H_3PO_4) as the second acid. Reaction **8**, carried out with a 1:1 ratio of H_2SO_4:TFA at room temperature for 24 h, produced stacked ribbons and partially unzipped MWCNTs with moderate levels of oxidation. The incomplete oxidation and exfoliation was supported by the small weight gain (34 wt%), C:O ratio of 4:1, TGA weight loss of 26 wt% at 950 °C, and UV λ_{max} of 265 nm.

Increasing the concentration of H_2SO_4 so that the H_2SO_4:second acid ratio is 9:1 results in nanoribbon formation and effective oxidation. This also confirms the necessity of ~90% H_2SO_4 for complete exfoliation of GONRs. Reactions **9** – **11** all underwent ~65 wt% gain upon isolation, had a C:O ratio of ~1.5:1, and a TGA weight loss of ~55 wt% at 950 °C. Reaction **9**, however, was run at room temperature and TEM and SEM imaging reveal that while ribbon formation occurred, the GONRs remained stacked and did not completely exfoliate. When heat is applied to the reaction (65 °C for 2 h as in reactions **10** and **11**), the GONRs were more exfoliated as identified by the presence of single ribbons by

TEM and larger graphene-like networks observed with bulk SEM imaging (few tube structures were identified). Because reactions **10** and **11** produced exfoliated GONRs with similar properties, the identity of the second acid is not specific to TFA and may be extended to other more convenient and less expensive reagents such as H_3PO_4. These optimized and less defective GONRs are termed here as extreme graphene oxide nanoribbons, or XGONRs.

Reaction **12** *used the same conditions as reaction* **11** (9:1 H_2SO_4:H_3PO_4 65 °C for 2 h) but increased the amount of $KMnO_4$ to 8×. This was performed to monitor the oxidation of the GONRs with increasing oxidizing agent. The product appeared to be more highly oxidized than that of reaction **11**; while the isolated weight gain and C:O ratios were comparable, more weight was lost in the TGA (82% versus 58% at 950 °C) and the UV λ_{max} of the product of reaction **12** is hypsochromically shifted further than any other sample studied (227 nm). Most striking, however, was the light brown color of the product of reaction **12**; while all samples thus far classified as "highly oxidized" were a brown-black color, the color of the product of reaction **12** was a significantly lighter brown (similar to peanut butter) than the others. This confirms the results previously found[1] that the degree of oxidation can be controlled by the level of oxidizing agent, even above the limit which is needed to obtain highly oxidized and exfoliated GONRs.

6.2.2 Physical and Chemical Properties of GONRs Produced in the Presence of a Second Acid

The XGONRs that were prepared in the presence of a second acid were further examined. Reactions **10** and **11** revealed striking differences compared to those prepared by the original method with H_2SO_4 only (reactions **1** – **5**, GONRs). When 10% of a second acid (TFA or H_3PO_4) is added to the reaction mixture, XPS confirms that a significantly larger proportion of oxygen exists in the form of hydroxyl groups, and fewer oxygen is attributed to C=O and COOH functionalities. The XPS C1s spectra of six selected products from Table 6.1 are shown in Figure 6.1, and a clear difference in shape and peak identity is evident. The C1s spectra of GONRs from reactions **1** and **4** are shown in Figure 6.1a and 1b, respectively. A distinct shoulder at 289 eV, assigned to carboxyl groups, is present in both products. The signals at 286-287 eV correspond to C-O, the intensity of which correlates to the level of oxidation within the sample while the signal at 284.9 corresponds to C-C bonds and is the most dominant peak in nonoxidized carbon species. The C1s spectra of the XGONRs from reactions **8**, **9**, **10**, and **11** are given in Figure 6.1c, d, e, and f, respectively. The low intensity of the C-O peak at 286 eV in Figure 6.1c (corresponding to reaction **8** prepared with 1:1 H_2SO_4:TFA) confirms that the ribbons are not as highly oxidized as those prepared with 90 – 100% H_2SO_4. Another important observation is the low intensity of the COOH shoulder at 289 eV for the XGONRs prepared in the presence of the second acid; it is significantly less pronounced than in the C1s

spectra of the GONRs (Figure 6.1a, b). This correlates to fewer COOH and C=O functionalities present in the XGONRs prepared with the second acid present.

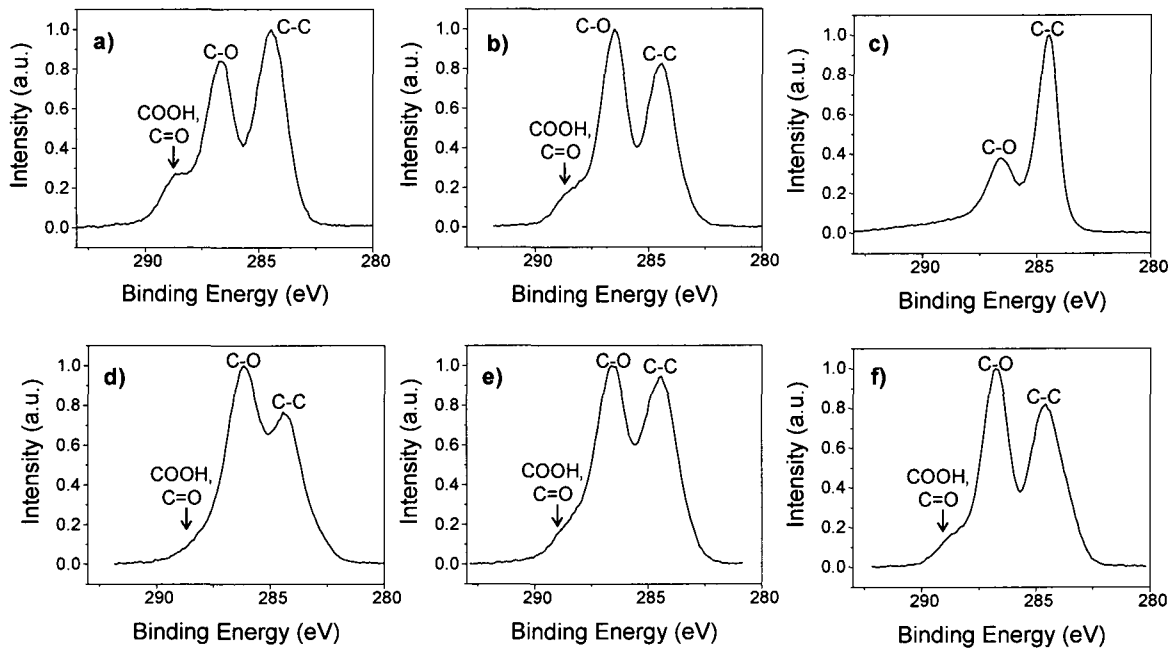

Figure 6.1. The XPS C1s spectra of the GONRs formed from reaction a) **1**, b) **4**, and XGONRs prepared from reaction c) **8**, d) **9**, e) **10**, and f) **11**. The COOH shoulder at 289 eV is significantly less pronounced for XGONRs (c-f) than GONRs (a,b) and can be attributed to fewer COOH and C=O functionalities present in the XGONRs prepared with a second weaker acid present.

Raman spectroscopy (633 nm laser excitation) was used to further evaluate the structure of XGONRs before and after chemical reduction by treatment with hydrazine to form extreme graphene nanoribbons (XGNRs). Hydrazine has previously been shown to be an effective agent for deoxygenation of GONRs and GO resulting in an increase in electrical conductivity.[1,4,6,7] Similar

to what has been reported, the G band (1594 cm^{-1}) broadens after oxidation with appearance of the D band at 1363 cm^{-1}. Upon reduction, aromaticity is restored to the system and it is initially expected for the G peak to increase in intensity accordingly. However, in agreement with previous reports for chemically reduced GONRs and GO,[1,6] the D:G ratio of XGONRs increases after reduction to XGNRs. It is hypothesized that reduction increases the number of small domains of aromaticity responsible for the D peak, but not necessarily their overall size, which is responsible for the G peak.[6] In addition, the increased edge effects due to the narrow width of ribbons versus graphene could enhance this observation.

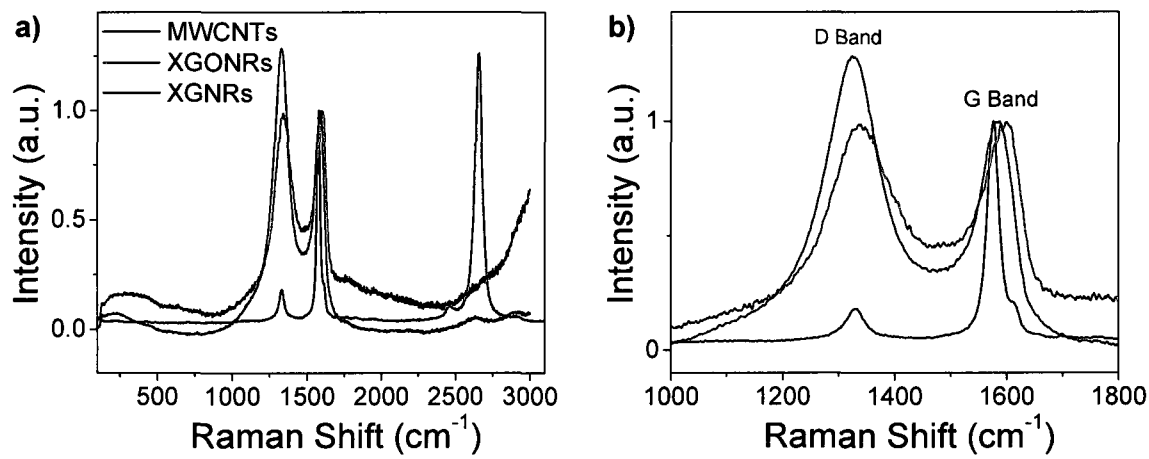

Figure 6.2. a) The Raman spectra (633 nm excitation) of XGONRs before (red) and after reduction (blue) compared to the MWCNT starting material (black). The behavior is very similar to that observed for GONRs and GNRs previously reported.[1] After chemical reduction with hydrazine, the D:G peak ratio increases, as previously reported for chemically converted graphene.[6,7] b) Expanded region

of D and G bands from (a). The peak intensities have been normalized to the G band.

The overall morphology and physical structure of the XGONRs, specifically the product of reaction **11**, was investigated using SEM and atomic force microscopy (AFM). It was found that compared to the GONRs prepared without the second acid, the XGONRs are longer with higher edge linearity.[1] AFM imaging, such as the representative image shown in Figure 6.3a, revealed long ribbons (> 5 μm) with straight, even edges and widths ranging from 75 – 200 nm. SEM imaging (Figure 6.3b-d) of XGONRs on a SiO_2 surface reveal mono- and few-layered ribbons several microns in length, with straight edges and uniform width. Also significant is the width of the ribbons observed in the agglomerate in Figure 6.3b; the majority of ribbons identified have widths < 100 nm, confirming that addition of 10% of a second acid prevents oxidative consumption of the narrow-width ribbons. Monolayer XGONRs, as shown in Figure 6.3c-d, as well as few-layered XGONRs (Figure 6.3a) were present. The height of ~1.5 nm for a bilayer GONR is double the theoretically calculated height of 0.75 nm for a monolayer of GO, as the oxygen-containing functionalities on each side add additional height over that of the parent graphene.[8]

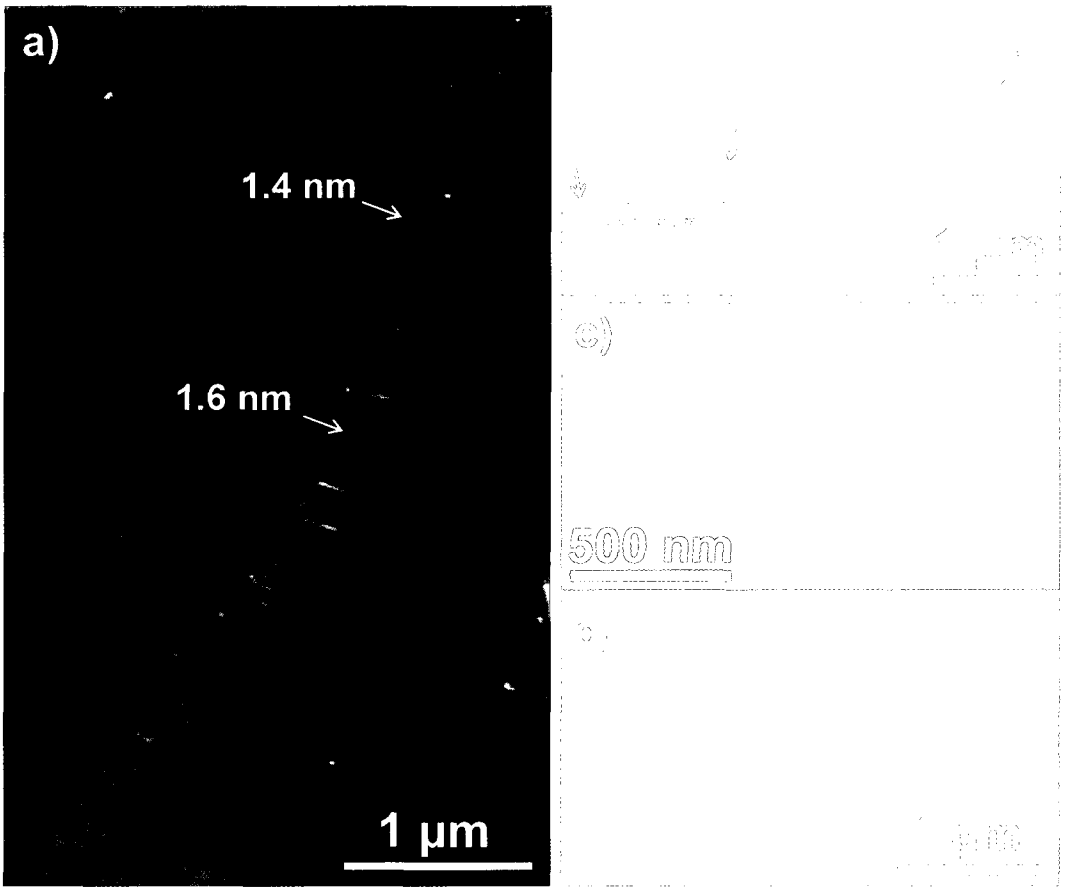

Figure 6.3. a) AFM image of a bilayer XGONR that is ~5 μm long prepared under the conditions of reaction **11**. 1.4 and 1.6 nm are the heights at the locations indicated; the horizontal lines in the XGONRs are buckles. b-c) SEM images of XGONRs (from reaction **11**) on a silicon surface. The width of the XGONRs indicated in the agglomerate of (b) are all <100 nm. The images in (c) and (d) also show what are probably monolayer XGONRs, based on studying the transparency to the electron beam of many samples.[9]

In order to study the quality and integrity of the nanoribbon surface, i.e. to determine if there are holes present in the basal plane, high resolution TEM (HR-TEM) imaging and high angle annular dark-field (HAADF) TEM imaging was

performed on both GONRs and XGONRs. TEM images obtained with a HAADF detector are very sensitive to changes in specimen composition with the intensity varying monotonically with composition and specimen thickness.[10] Thus, HAADF imaging is highly sensitive to variations in the atomic structure of the sample and should effectively identify regions of defects and/or interruptions in the carbon plane. Figure 6.4a shows a bright field HR-TEM image of a portion of a ribbon from reaction **11** with its corresponding electron diffraction pattern. The sample appears to be uniform and smooth over the entire region, and the hexagonal diffraction pattern corresponds to a crystalline graphite structure. Figures 6.4b – d show three HAADF images, each taken of the same region of a ribbon at increasing magnification. The atomic structure of the ribbon appears uniform, with little disruption in the contrast indicating few defects. This is further confirmed by comparing HAADF and HRTEM images (Figure 6.5a–d) of GONRs prepared without a second acid (reaction **1**) to XGONRs prepared with 10% H_3PO_4 (reaction **11**); there is a clear difference in the structural uniformity. The HAADF of GONRs (Figure 6.5a) shows changes in contrast throughout the entire imaged area; dark "spotty" patches corresponding to disruptions, including holes in the basal plane, can be identified. Comparison of the bright field TEM images in Figure 6.5c–e of GONRs and XGONRs show similar observations. At comparable magnification, the XGONRs have a smoother surface with fewer defects and/or holes than the GONRs. Electronic devices are currently being constructed by other lab members to test the improvement in electrical conductivity upon chemical reduction.

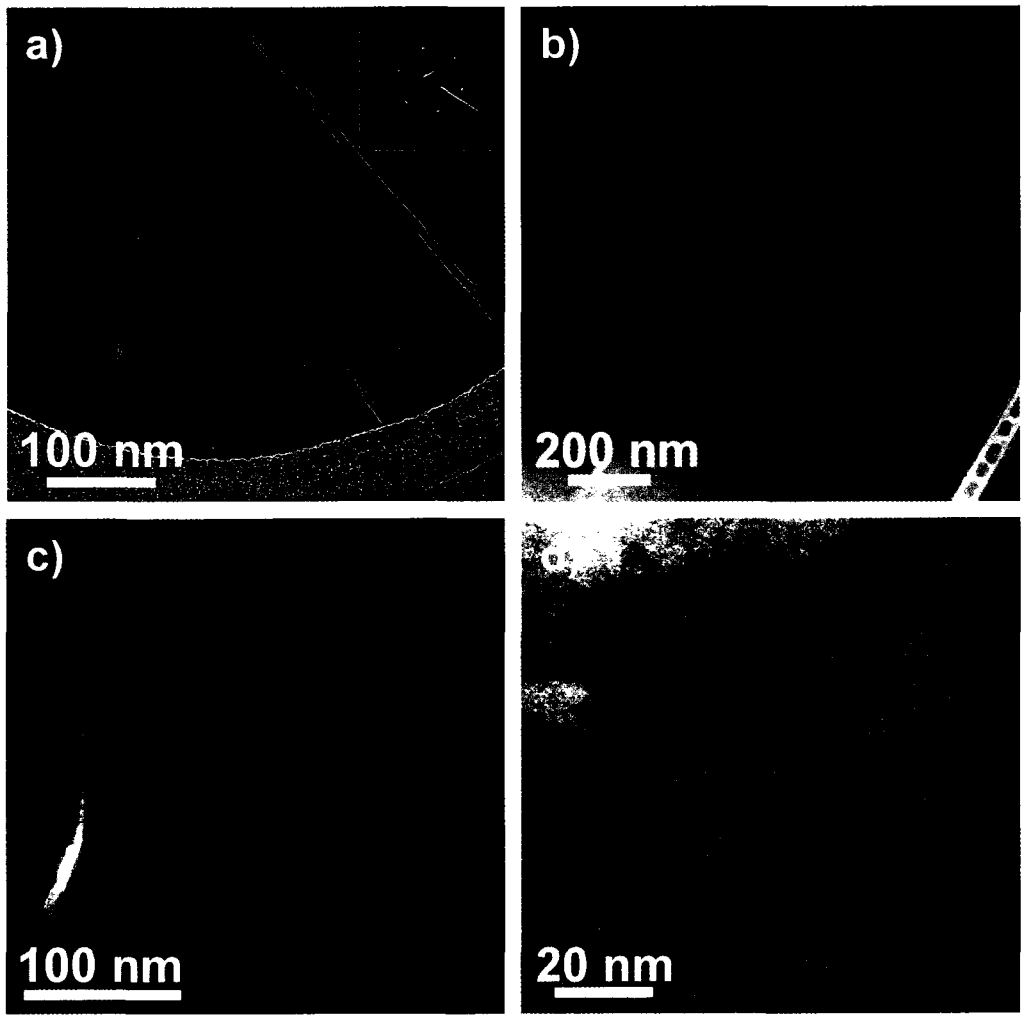

Figure 6.4. a) Bright field TEM image of a XGONR prepared from reaction **11** with corresponding electron diffraction pattern (inset). The smooth ribbon surface and sharp, hexagonal diffraction pattern indicate the high-quality of the ribbons formed. The black curved structure at the bottom is part of the lacey carbon grid. b-d) HAADF TEM images on one XGONR at increasing magnification from (b) to (d). The uniformity of the atomic structure is apparent in that there are few instances of disruption in the contrast.

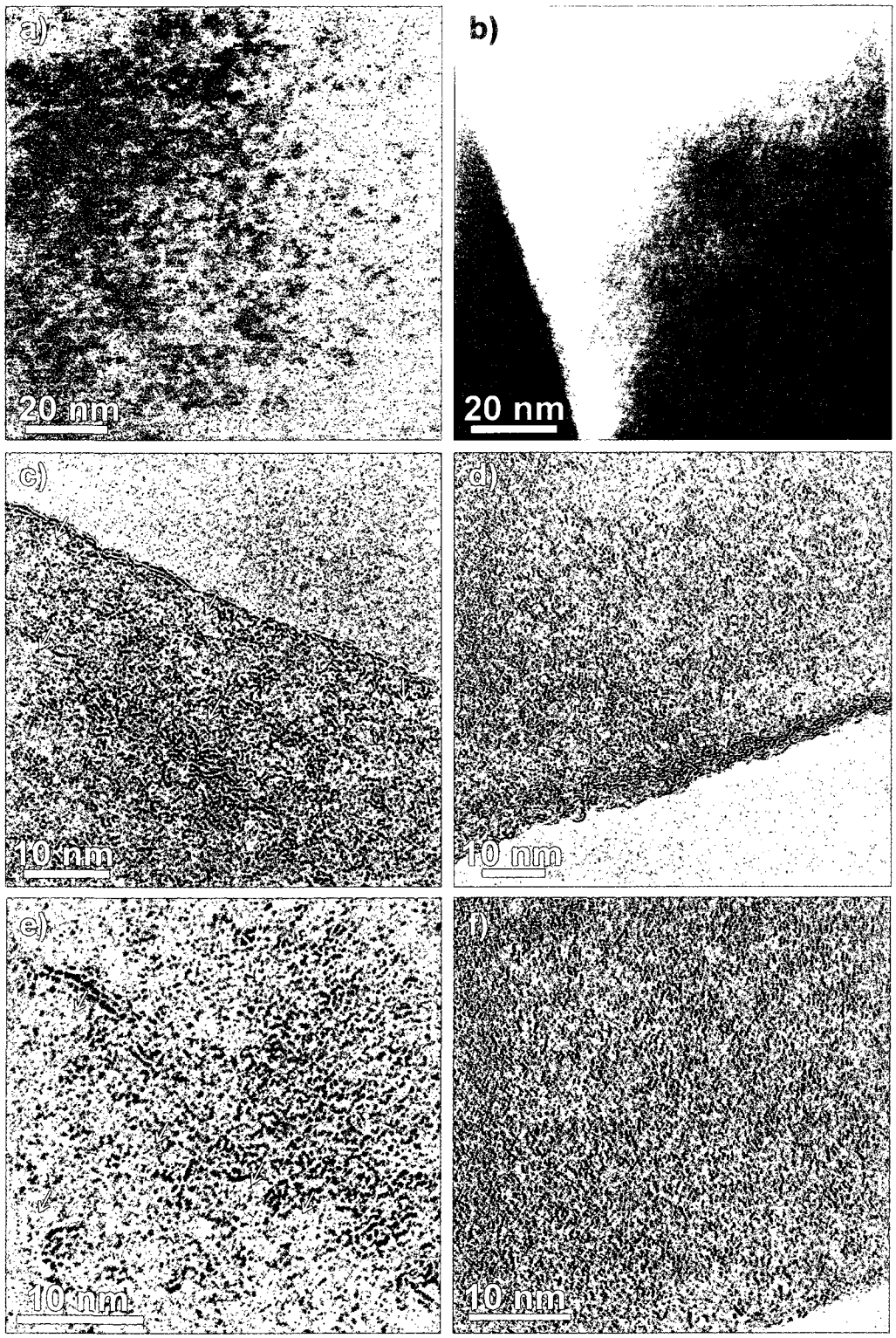

Figure 6.5. TEM images comparing the surface quality of GONRs (a, c, e) and XGONRs (b, d, f). HAADF TEM images of a) GONR and b) XGONR. The

smooth surface of the XGONR is apparent by uniform contrast over the entire area; the GONR has changing contrast with a spotty appearance indicative of nonuniformity in the atomic structure.[3] c-e) Bright field HRTEM images of GONRs (c, e) and XGONRs (d, f). Close examination of the GONR images reveals small holes and defects (a few indicated by white arrows) that make the surface appear roughened. The XGONR surface, on the other hand, is smoother in appearance with very few features that indicate defects.

6.2.3 Proposed Reaction Mechanism

A proposed mechanism for the participation of the second acid in the oxidization of MWCNTs that results in XGONRs is given in Scheme 6.1. It is thought that the second acid improves the chemoselectivity of the oxidation process. After initial manganate ester formation (**2** in Scheme 6.1), the vicinal diols that are formed will eventually cleave at the carbon-carbon bond between them, giving diketones and a new hole in the nanoribbon. Destructive oxidation throughout the structure then occurs and leads to defects and irreversible changes in the basal planes that cannot be repaired with chemical reduction. However, when an acid such as H_3PO_4 is present, it will protect the vicinal diols by forming esters (**5** or **6**), thus preventing or retarding over-oxidation to the diketones. We have carried out this higher-selective process using not only TFA and H_3PO_4, but also polyphosphoric ($HO(PO_2OH)_xH$), metaphosphoric ($(HPO_3)_x$) and boric acid (H_3BO_3). These latter three additives gave similar selectivity effects. Any reagent convertible to these acids under the reaction conditions

such as corresponding salts, anhydrides, mixed anhydrides and esters is expected to afford similar protection. The general requirements and desires for the protective group are high rate of introduction, redox inactivity under the reaction conditions, and ease of removal during the subsequent work-up. It is also important to note that the presence of a second acid does not change the overall process through which unzipping of the MWCNT occurs. As previously reported,[1] the kinetics of unzipping resembles that of chain-reaction polymerization – propagation must occur faster than initiation, otherwise such straight and even edges would not be observed due to numerous initiation sites on the MWCNT sidewall. The rate-limiting step is formation of the manganate ester species (**2**); once this occurs, the oxidative unzipping happens on a faster time scale, and due to the subsequent bond strain, takes place at the moment of initiation.

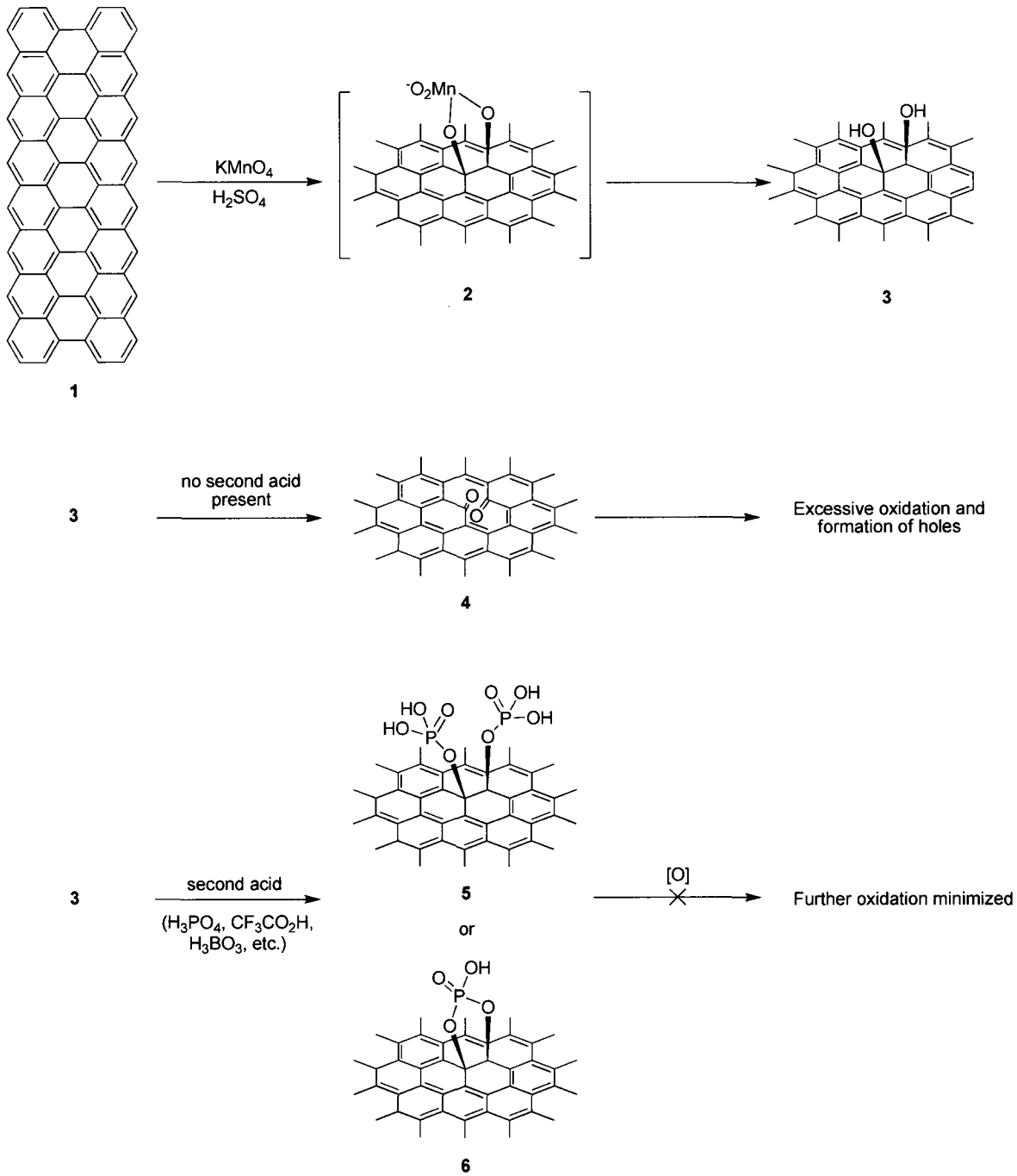

Scheme 6.1. Proposed mechanism for the effect of the second acid in preventing over-oxidation of the nanoribbons once they form from a MWCNT. The manganate ester in **2** could also be protonated. The key step is formation of

ester intermediates, **5** or **6**, resulting in protection of the vicinal diols (**3**) formed during the oxidation.

6.2.4 Preparation of Narrow GONRs from SWCNTs

Treatment of single-walled carbon nanotubes (SWCNTs) with $KMnO_4$ in H_2SO_4 resulted in formation of narrow GONRs that were shortened in length, as reported in Chapter 5, section 5.2.6. All SWCNTs used were purified (pSWCNTs) before use to lower the catalyst content.[11] Further studies were conducted by treating pSWCNTs with $KMnO_4$ in the presence of H_2SO_4 and a second acid, specifically TFA, to give narrow GONRs. It was found that when H_2SO_4 was present at any ratio with TFA, the produced narrow GONRs were still significantly shortened in length. However, when pSWCNTs were exposed to the same conditions as reaction **7** (TFA/TFAA only, 5× $KMnO_4$, room temperature for 24 h, with the exception that the pSWCNTs were suspended for 12 h in TFA/TFAA before addition of $KMnO_4$), they appeared to be less intertwined and longer than those prepared with H_2SO_4. TEM imaging (Figure 6.6a) revealed that the GONRs are not completely exfoliated and tend to form bundled networks. Nevertheless, within these network structures single GONRs could be located (Figure 6.6b-d). AFM images (not shown) reveal similar network structures, but single ribbons were unable to be resolved. The narrow GONRs shown in Figure 6.6 appear to be 3-5 nm in width, as expected when derived from pSWCNTs ~1 nm in diameter.

XPS and Raman spectroscopy were used to compare the degree of oxidation of narrow GONRs prepared with H_2SO_4 and TFA. The XPS C1s spectra given in Figure 6.7a show that the peaks at 286, 287, and 289 eV, assigned to C-O and C=O functionalities, are significantly less intense for the narrow GONRs synthesized in TFA. Therefore, the narrow GONRs prepared by the second method are less oxidized; the XPS atomic concentrations (Figure 6.7c) confirm that they have ~10% less oxygen than narrow GONRs prepared in H_2SO_4. The fewer oxygen-containing functionalities on the narrow GONRs prepared in TFA can also account for the majority of the GONRs remaining bundled and forming network structures – the conditions with TFA alone as the acid medium are not sufficient to exfoliate the starting pSWCNT bundles. Raman spectroscopy (Figure 6.7b), however, confirms that the sp^2 hybridized conjugation is disrupted (D:G ratio of 1:1, Figure 6.7b, bottom left) and that no tube structures remain after oxidation, as indicated by disappearance of the RBMs (Figure 6.7b, bottom right). Further studies which expose pSWCNTs to $KMnO_4$ in other acid media, such as H_3PO_4, should be continued so that the optimum conditions for formation of long and exfoliated narrow GONRs may be found.

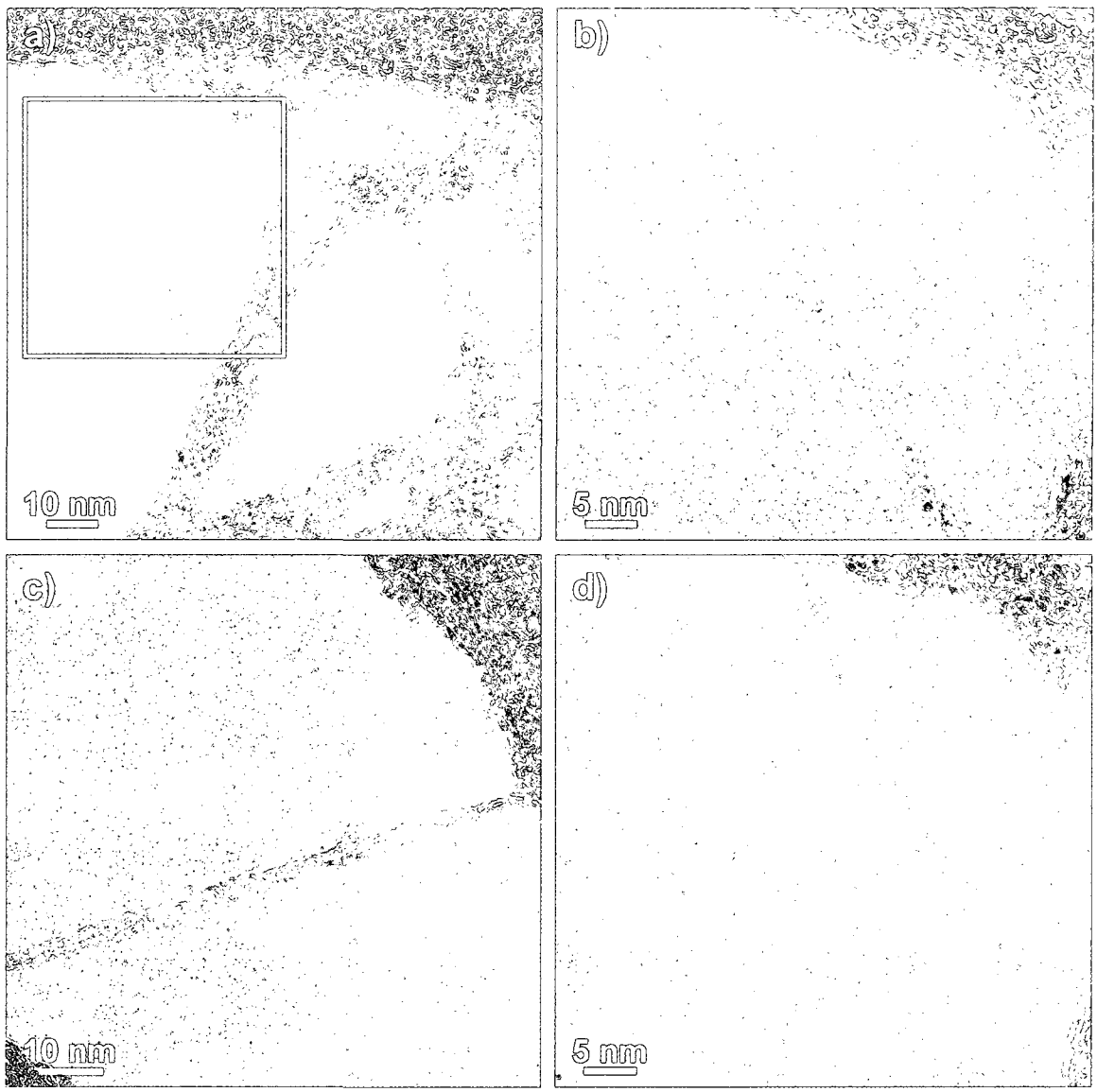

Figure 6.6. TEM images of narrow GONRs prepared in TFA medium (similar to reaction 7). The network structures that are formed are evident in image (a). b) High magnification image of the GONR from boxed region in image (a). c-d) Additional narrow GONRs found in the sample. The transparency and low contrast of the ribbon structures indicate that they are likely singles. If the electron beam was focused too long on the ribbon, the collected energy caused them to oscillate and eventually break.

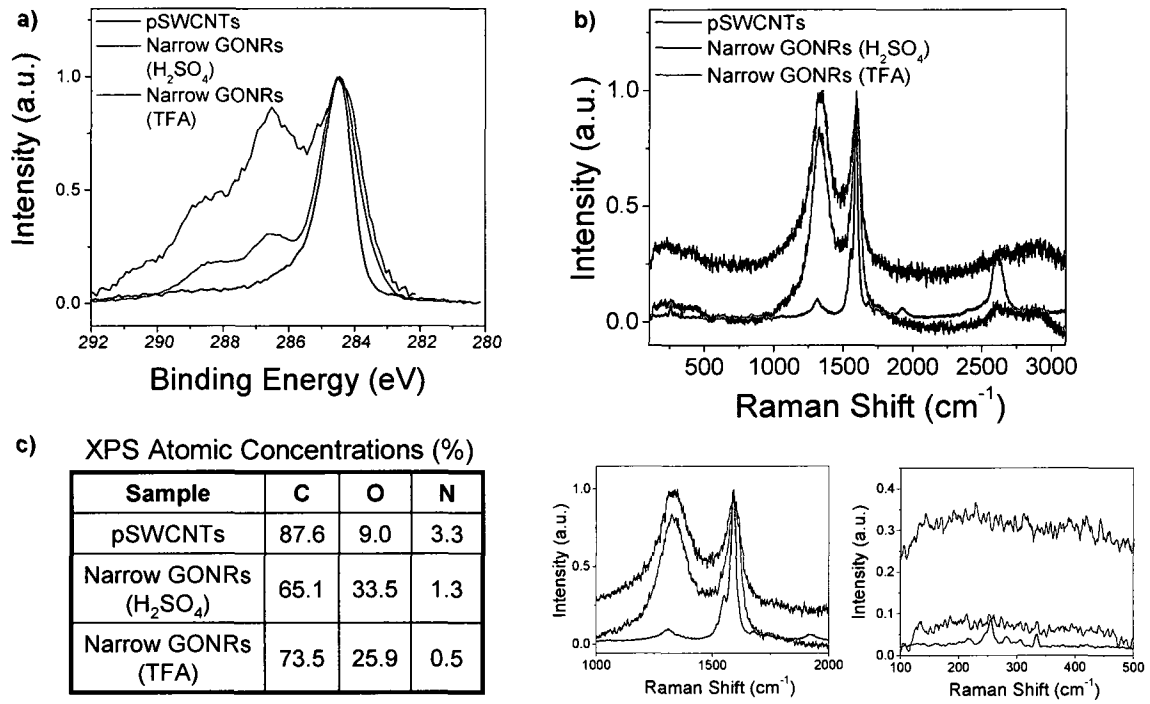

c) XPS Atomic Concentrations (%)

Sample	C	O	N
pSWCNTs	87.6	9.0	3.3
Narrow GONRs (H_2SO_4)	65.1	33.5	1.3
Narrow GONRs (TFA)	73.5	25.9	0.5

Figure 6.7. a) XPS C1s spectra comparing narrow GONRs prepared in H_2SO_4 medium (red) to those prepared in TFA medium (green); the spectrum of pSWCNTs is also given for reference. The less intense C-O and C=O peaks at 287 and 289 eV, respectively, for TFA-synthesized narrow GONRs indicate the lesser degree of oxidation. b) The Raman spectra (633 nm laser excitation) of narrow GONRs prepared in H_2SO_4 medium (red) and those prepared in TFA medium (green) compared to pSWCNTs (black). Enlarged portions of the D and G bands (bottom left) and RBMs (bottom right) are also given. d) XPS-determined atomic concentrations of narrow GONRs and pSWCNTs corresponding to the C1s spectra shown in (a).

6.3 Conclusions

Variations in the reaction conditions for the synthesis of GONRs[1] including the acid medium, time, and temperature were explored to determine the significance of each variable, and to further elucidate the mechanism of interaction of the acid medium and oxidizing agent with the MWCNTs. It was found that sufficient H_2SO_4 (~90 vol%) was crucial for complete formation and exfoliation of the nanoribbons; in addition, elevation of the reaction temperature to 60 °C was necessary. Most interesting, however, was that addition of 10 vol% of a second acid such as TFA or H_3PO_4 greatly enhanced the quality of the nanoribbons that are produced. The new nanoribbons have a higher degree of oxidation (diols) but lower levels of hole formation that bear carbonyl and carboxyl moieties. These new forms of GONRs are termed extreme graphene oxide nanoribbons, or XGONRs. The improved procedure did not result in the digestion of the thinner, < 100 nm in width, nanoribbons. This also maximizes the aspect ratio of the products obtained. These observations were confirmed by AFM, SEM, and TEM; electrical conductivity testing of devices is currently underway and preliminary results with XGNRs indicate improvement up to an order of magnitude compared to devices constructed with GNRs.

6.4 Experimental

6.4.1 Preparation of Nanoribbons

MWCNTs were used as received from Mitsui & Co., Ltd. (Lot No. 05072001K28). These MWCNTs (MWNT-7) are now produced in the same manner but under the sole oversight of Hodogaya Chemical Co., Ltd and they can be purchased from that entity (2-4-1, Shiba Koen, Minato-Ku, Tokyo 105-0011, Japan, +81-3-6430-3600). SWCNTs used were produced via the HiPco process[12] (batch number 187.4) by the Carbon Nanotechnology Laboratory at Rice University and purified[11] prior to use. The remaining chemicals were purchased from Sigma-Aldrich and used as received, except for the concentrated sulfuric acid (Fisher Scientific) and oleum (Alfa Aesar). Deionized (DI) water (18 MΩ resistivity) obtained from a NanoPure system (Barnstead, Dubuque, IA USA) was used throughout this work. *Note*: Once nanoribbons are formed, they must only be manipulated with gentle stirring or short exposure bath sonication; use of high sheer homogenization, probe sonication, or cup-horn sonication will result in shortened GNRs. All suspensions were prepared with gentle magnetic stirring, unless otherwise indicated. Bath sonication was performed with a Cole Parmer ultrasonic cleaner, Model 08849-00 for the specified amount of time.

Nanoribbon formation. Formation of nanoribbons from MWCNTs via procedure **1 – 5** was carried out as previously described in Chapter 5 (section 5.4.1),[1] with variations in the time and temperature as noted. ***Caution**: Do not exceed ~0.5% wt/vol, weight $KMnO_4$ to volume of H_2SO_4. It is reported that at much higher concentrations, namely 7% wt/vol $KMnO_4$ in H_2SO_4, the mixture can*

explode upon heating.[13] Briefly, MWCNTs (150 mg, 12.5 mequiv of carbon) were suspended in 30 mL conc H_2SO_4 for a minimum of 1 h and up to 12 h. $KMnO_4$ (750 mg, 4.75 mmol) was then added and the mixture allowed to stir for 1 h at room temperature. The reaction was then heated according to the reaction specifications in Table 6.1. Reaction **1** was identical to the procedure previously described[1] (gradual increase to 70 °C over a period of 1 h) while reaction **2** was maintained at room temperature for 2 h. Reaction **3** was heated to 60 °C for 1 h, reaction **4** to 85 °C for 1 h, and reaction **5** to 100 °C for 1 h. Upon completion, the mixture was removed from the heat source and allowed to cool to room temperature, followed by work-up as described below.

Reaction **6** – 150 mg of MWCNTs were suspended in 15 mL conc H_2SO_4 for 15 min. The reaction mixture was placed in an ice bath and 15 mL oleum (H_2SO_4, 20% free SO_3) was slowly added. The mixture was stirred for 1 h, during which time the temperature was allowed to equilibrate to 25 °C by removing/applying an ice bath as appropriate. $KMnO_4$ (750 mg) was then added and the mixture allowed to stir for 24 h at room temperature. The product was isolated as described below.

Reaction **7** – 150 mg MWCNTs were suspended in 60 mL TFA and 15 mL TFAA by stirring for 15 min followed by bath sonication for 10 min. $KMnO_4$ (750 mg) was then added and the mixture was bath sonicated for an additional 5 min. The solution was allowed to stir at room temperature for 24 h, with intermittent bath sonication (5 min) every few h. Before quenching, the consumption of $KMnO_4$ was monitored by taking 0.1 mL of reaction mixture and diluting it with 1

mL water. When no purple color was detected, the reaction was complete and the work-up procedures followed as described below.

Reaction **8** - 150 mg MWCNTs were suspended in 37.5 mL TFA and 37.5 mL H_2SO_4 by stirring for 15 min followed by bath sonication for 10 min. $KMnO_4$ (750 mg) was then added and the mixture was bath sonicated for an additional 5 min. The solution was allowed to stir at room temperature for 24 h, with intermittent bath sonication (5 min) every few h. Before quenching, the consumption of $KMnO_4$ was monitored by taking 0.1 mL of reaction mixture and diluting it with 1 mL water. When no purple color was detected, the reaction was complete the and work-up procedures followed as described below.

Reactions **9** and **10** – 150 mg MWCNTs were suspended in 36 mL H_2SO_4 by stirring for a period of 1 h. TFA (4 mL) was then added and allowed to stir another 15 min before addition of $KMnO_4$ (750 mg). For reaction **9**, the reaction mixture was allowed to stir at room temperature for 24 h; for reaction **10**, the reaction mixture stirred 1 h at room temperature and 2 h at 65 °C. Once the contents had cooled, the work-up procedure was followed as described below.

Reaction **11** – 150 mg MWCNTs were suspended in 36 mL H_2SO_4 by stirring for a period of 1 h. H_3PO_4 (85%, 4 mL) was then added and allowed to stir another 15 min before addition of $KMnO_4$ (750 mg). The reaction mixture was then heated at 65 °C for 2 h, then the mixture was allowed to cool to room temperature before product isolation.

Reaction **12** - 150 mg MWCNTs were suspended in 36 mL H_2SO_4 by stirring for a period of 1 h. H_3PO_4 (85%, 4 mL) was then added and the mixture

was allowed to stir another 15 min before addition of $KMnO_4$ (1.2 g). The reaction mixture was heated at 65 °C for 2 h, then allowed to cool to room temperature before product isolation.

Work up procedures. The products obtained from reactions **1** – **6** were worked up by pouring the cooled reaction mixture onto 400-mL of ice containing 5 mL of 30% H_2O_2 (to prevent precipitation of insoluble MnO_2). After vacuum filtration through a PTFE membrane (5.0 μm pore size), the solid was removed and stirred in 150 mL water for 30 min, followed by bath sonication for 15 min. The material was coagulated by addition of 20 vol% conc HCl (30 mL). The solid was filtered through a PTFE membrane (0.45 μm pore size) followed by removal of the solid and stirring in 150 mL ethanol for 30 min and bath sonication for 15 min. The material was coagulated by addition of 100 vol% ether (150 mL) followed by filtration through a PTFE membrane (0.45 μm pore size). The final product was washed 2× with ether (50 mL each) and dried in vacuo to give the following yields: **1** – 360 mg; **2** – 189 mg; **3** – 308 mg; **4** – 293 mg; **5** – 204 mg; **6** – 150 mg.

Reactions **7** and **8** – The reaction mixture was poured onto ice (100 mL) containing H_2O_2 (30%, 5 mL) and filtered through a PTFE membrane (5.0 μm pore size) to give a black solid. The solid was washed with 20 vol% HCl (2× 60 mL) and redispersed in ethanol (100%, 120 mL) with stirring (30 min) and bath sonication (15 min) before filtering through the same PTFE membrane. The product was washed 2× with ethanol (15 mL each), 2× with ether (15 mL each), and dried in vacuo to give the following yields: **7** – 150 mg; **8** – 201 mg.

Reactions **9** and **10** – The dispersion was poured onto 120 mL of ice containing H_2O_2 (30%, 5 mL), filtered through a PTFE membrane (5.0 μm pore size), and washed 3x with 10 vol% HCl (40 mL each). The solid was then dispersed in ethanol (100%, 30 mL) by stirring (30 min) and bath sonication (15 min). Ether (20 mL) was added to coagulate the product, which was again filtered over the same PTFE membrane. The remaining solid was washed with 2x with ether (50 mL each) and dried *in vacuo* to give the following yields: **9** – 240 mg; **10** – 248 mg.

Reaction **11** – The reaction mixture was poured onto 100 mL ice containing H_2O_2 (30%, 5 mL). The product was allowed to coagulate for 14 h before filtering over a 200 nm PTFE membrane. The brown filter cake was washed 2x with 20% HCl (6 mL each), resuspended in H_2O (60 mL) by stirring for 2 h and recoagulated with HCl (30%, 40 mL). The product was filtered on the same PTFE membrane and then dispersed in ethanol (100%, 40 mL) for 2 h with stirring. Ether (60 mL) was then added to the suspension and the mixture was allowed to coagulate for 1 h before filtering through a 200 nm PTFE membrane. The remaining solid was washed 2x with ether (10 mL each) and vacuum dried to yield 267 mg of product **11**.

Reaction **12** – The reaction mixture was poured onto 100 mL ice containing H_2O_2 (30%, 5 mL). The resulting light-brown colored precipitate was collected on a 200 nm PTFE membrane, washed 2x with HCl (20 vol%, 6 mL each) and resuspended in H_2O (60 mL) by stirring for 2 h. Then HCl (30 vol%, 60 mL) was added to coagulated the product, which was then was collected on

the same PTFE membrane, washed 2× with HCl (20%, 6 mL each) and dispersed in ethanol (40 mL) for 2 h with stirring. Then the product was again coagulated by addition of ether (60 mL), filtered over the same PTFE membrane, washed 3× with ether (6 mL each) and vacuum dried to yield 215 mg of product **12**.

6.4.2 Sample Analysis

The procedures and instruments used for sample analysis are the same as described in Chapter 5, section 5.4.5.

6.5 References

1. Kosynkin, D. V.; Higginbotham, A. L.; Sinitskii, A.; Lomeda, J. R.; Dimiev, A.; Price, B. K.; Tour, J. M. *Nature* **2009**, *458*, 872-876.
2. Lerf, A.; He, H.; Forster, M.; Klinowski, J. *J. Phys. Chem. B* **1998**, *102*, 4477-4482.
3. Mkhoyan, K. A.; Contryman, A. W.; Silcox, J.; Stewart, D. A.; Eda, G.; Mattevi, C.; Miller, S.; Chhowalla, M. *Nano Lett.* **2009**, *9*, 1058-1063.
4. Eda, G.; Fanchini, G.; Chhowalla, M. *Nature Nanotech.* **2008**, *3*, 270-274.
5. Dzhabiev, T. S.; Denisov, N. N.; Moiseev, D. N.; Shilov, A. E. *Russ. J. Phys. Chem.* **2005**, *79*, 1755-1760.
6. Stankovich, S.; Dikin, D. A.; Piner, R. D.; Kohlhaas, K. A.; Kleinhammes, A.; Jia, Y.; Wu, Y.; Nguyen, S. T.; Ruoff, R. S. *Carbon* **2007**, *45*, 1558-1565.

7. Tung, V. C.; Allen, M. J.; Yang, Y.; Kaner, R. B. *Nature Nanotech.* **2009**, *4*, 25-29.

8. Schniepp, H. C.; Li, J.-L.; McAllister, M. J.; Sai, H.; Herrera-Alonso, M.; Adamson, D. H.; Prud'homme, R. K.; Car, R.; Saville, D. A.; Aksay, I. A. *J. Phys. Chem. B* **2006**, *110*, 8535-8539.

9. Sinitskii, A.; Dimiev, A.; Kosynkin, D. V.; Tour, J. M. *submitted* **2009**.

10. Midgley, P. A.; Weyland, M. *Ultramicroscopy* **2003**, *96*, 413-431.

11. Chiang, I. W.; Brinson, B. E.; Huang, A. Y.; Willis, P. A.; Bronikowski, M. J.; Margrave, J. L.; Smalley, R. E.; Hauge, R. H. *J. Phys. Chem. B* **2001**, *105*, 8297-8301.

12. Nikolaev, P.; Bronikowski, M. J.; Bradley, R. K.; Rohmund, F.; Colbert, D. T.; Smith, K. A.; Smalley, R. E. *Chem. Phys. Lett.* **1999**, *313*, 91-97.

13. Olley, R. H.; Bassett, D. C. *Polymer* **1982**, *23*, 1707-1710.

6.6 Experimental Contributions

My contributions to the experimental work in this chapter are the following: obtained all TEM images in Table 6.1 and Figure 6.5c-e, as well as all AFM, XPS, UV, TGA, Raman, and IR data presented. Dmitry Kosynkin performed reactions **1 – 12**, assisted in analyzing the collected data, and conceived and proposed the mechanism presented in Scheme 6.1. Alexander Sinitskii collected the SEM images in Table 6.1, and Zhengzong Sun obtained the HAADF TEM images in Figures 6.4 and 6.5a-b.

Chapter 7

Covalent Functionalization of Surfactant-Wrapped Graphene Nanoribbons

7.1 Introduction

The graphene oxide nanoribbons (GONRs) isolated from the solution-based bulk method from oxidative treatment of MWCNTs presented in Chapter 5, although produced in quantitative yield, have highly oxidized sidewalls.[1] In order to restore the ribbons to a more graphene-like structure, subsequent chemical reduction with hydrazine must be carried out. Though some of the electrical conductivity is restored after reduction, the GNRs were found to aggregate and precipitate from solution very quickly if surfactant is not used. This hinders the processability of GNRs in reduced form. Furthermore, once isolated from the reduction reaction, the aid of sonication is necessary to disperse the reduced GNRs in organic solvents such as *N,N*-dimethylformamide (DMF) and *N*-methyl-2-pyrrolidinone (NMP) which causes shortening of the ribbons.

Previous work in our group has shown that covalent functionalization can be successfully carried out on chemically converted graphene sheets[2] and carbon nanotubes[1,3-5] in order to increase the processability of those materials. This chapter presents two different covalent functionalization methods that were developed for GNRs. In addition to direct diazonium salt addition, an in situ route using an aniline and organic nitrite was successfully applied. The resulting functionalized GNRs (f-GNRs) are readily soluble in organic solvents such as DMF and NMP. The f-GNRs were also found to be in the reduced state, with minimal sp^2 carbon disruption, while also keeping the ribbon shape.

7.2 Results and Discussion

Owing to the high yield of individual nanoribbons, chemical unzipping of carbon nanotube to graphene nanoribbons exhibits advantages over other methods.[6-9] The restoration of the ribbons to a graphene-like structure has been confirmed.[1] This procedure, as a high-throughput method, will be preferred for preparation of composites or transparent electrode materials, where large quantities are required.

The two routes for functionalization are shown in Scheme 7.1. The treatment of GNRs with aryl diazonium salts (Route I) was found to proceed similarly to the reaction of surfactant wrapped, chemically converted graphene sheets with aryl diazonium salts.[2,10] While the in situ functionalization of GNRs using organic nitrite and aniline (Route II) has not yet been reported for graphene materials, it has been successfully applied to functionalization of carbon nanotubes.[4,11]

X-ray photoelectron spectroscopy (XPS) was used to verify the success of functionalization reactions. Previous results on the chemical reduction of GNRs indicated there was significant removal of oxygen groups by hydrazine treatment.[1] Similar results were observed by high resolution XPS C1s spectra of the f-GNRs, which show a significant decrease of signals at 286-288 eV, indicating the loss of C-O and C=O functionalities (Figure 7.1). The surface oxygen groups in GNRs were estimated to be 42%, while after treatment with hydrazine the atomic concentration of oxygen decreased to 16%.[1] Since these are ribbon structures, the high remaining edge carboxyl units will undergo little

reductive loss. Depending on the functional groups, the surface oxygen in f-GNRs range from 11 to 32% (Table 7.1). A small portion of nitrogen content exists in all products, which can be attributed to hydrazones (except the N1s XPS spectra of **2c** and **3c**, which exhibit a significant contribution from the nitro group as well).[12,13]

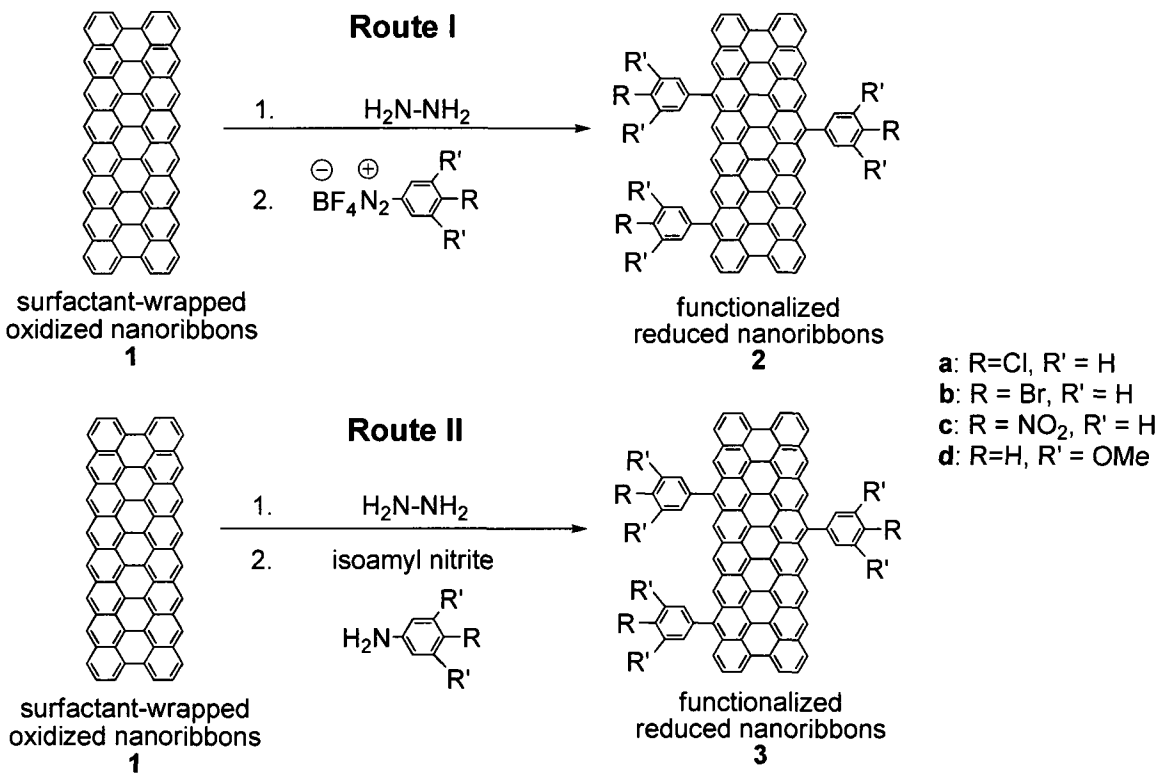

Scheme 7.1. Syntheses routes I and II for the production of f-GNRs. The oxidized starting material nanoribbons (**1**) bear oxygen-containing functionalities such as carbonyls, carboxyls, epoxides, and hydroxyls (not shown). Covalent attachment of the aryl moieties is not limited to the edges of the nanoribbons as depicted for functionalized products **2** and **3**; attachment at the basal plane is also expected.

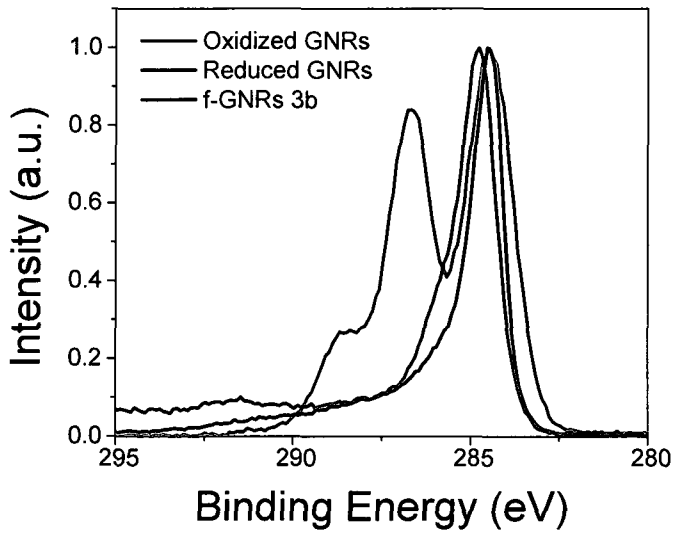

Figure 7.1. High-resolution XPS C1s spectra of oxidized GNRs (red), reduced GNRs (black), and f-GNRs **3b** (blue) showing significant loss of C-O and C=O groups after reduction.

Upon treatment with the diazonium salts (Route I) or with the in situ functionalization procedure (Route II), a significant percentage of halogen markers (Cl or Br) were detected with very little accompanying nitrogen, implying that the surface has been successfully functionalized (Figure 7.2). Therefore, the data supports the conclusion that both routes resulted in successful functionalization. Similar to the previous report of functionalization of graphene sheets, the functionalized graphene nanoribbons were formed by covalent grafting of diazonium species.[2,14] High-resolution XPS of **2c** and **3c** show two signals for the N1s peak. The signal at 405 eV can be attributed to the nitro group (Figure 7.2). High resolution XPS of **2d** and **3d** show a broad C1s signal,

which is partially due to the presence of the C-O bond, such as that found in a methoxy group on a substituted phenyl ring. The fitting of C1s (Figure 7.3) exhibits a clear peak from C-O (286.2 eV) as well as a residual signal from carboxylic acids C=O (287.7 eV).

Table 7.1. High-resolution XPS results of **2** and **3**.*

Sample	Atomic concentration (%)				
	C	N	O	Cl	Br
2a	80.2	2.8	10.9	5.0	-
2b	77.5	5.5	11.4	-	5.6
2c	70.8	9.5	19.5	-	-
2d	73.6	3.9	22.5	-	-
3a	74.1	3.1	16.4	6.4	-
3b	79.6	3.5	14.3	-	2.6
3c	66.9	5.6	27.5	-	-
3d	65.4	3.0	31.6	-	-
Oxidized GNRs	52.0	1.3	35.8	-	-
Reduced GNRs	79.1	3.5	17.3	-	-

* A dash indicates an atomic concentration of <0.5% was detected by XPS.

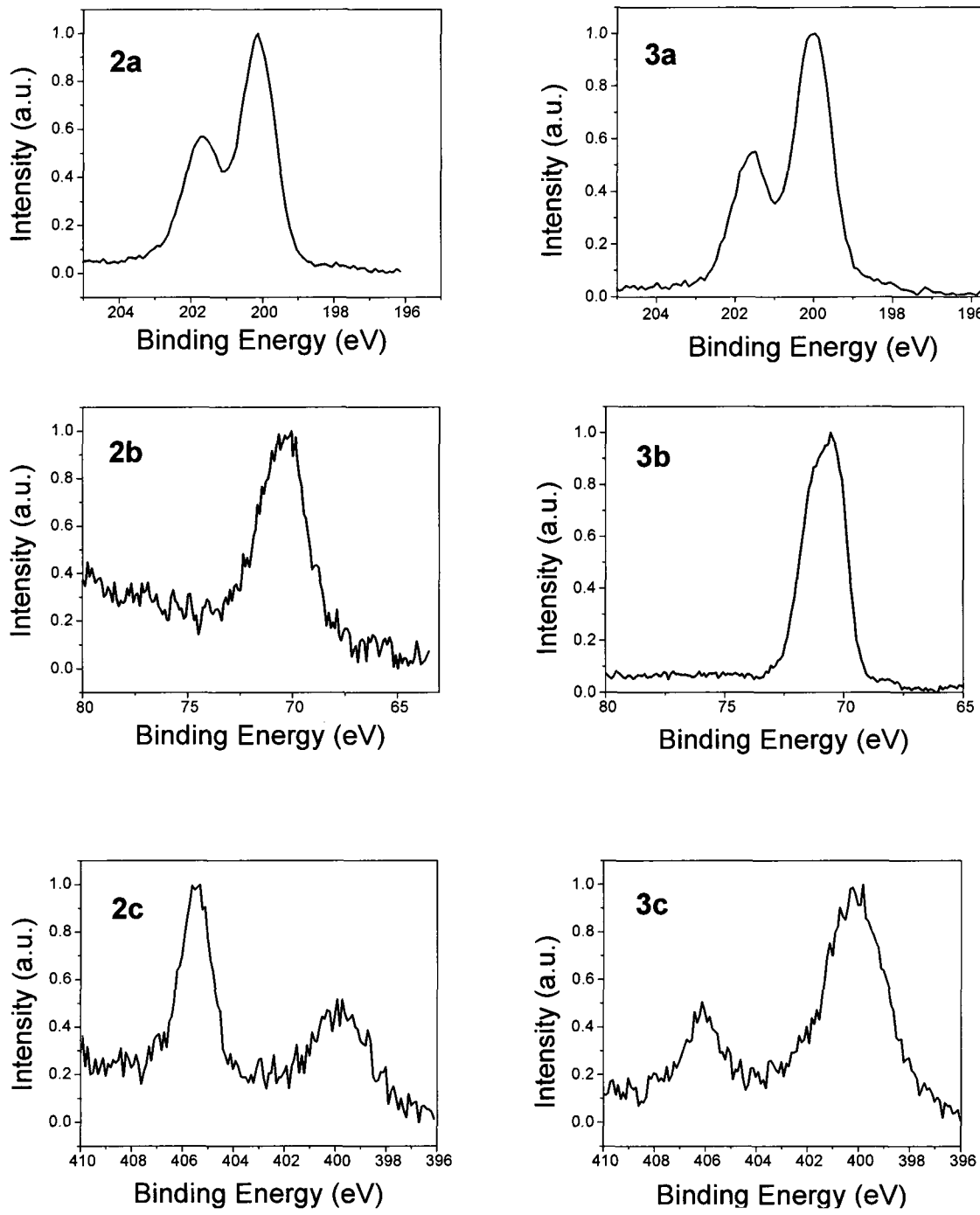

Figure 7.2. High-resolution XPS Cl2p spectra of **2a** and **3a** (top row), Br3d spectra of **2b** and **3b** (middle row), and N1s spectra of **2c** and **3c** (bottom row).

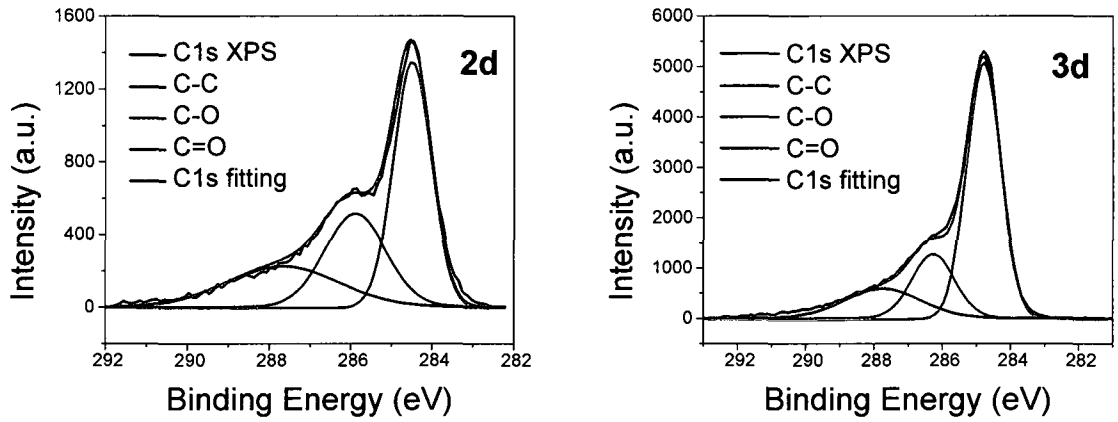

Figure 7.3. Fitting of high-resolution XPS C1s spectrum of **2d** and **3d** (C-C: 284.5 eV, C-O: 285.9 eV and C=O: 287.7 eV).

Control experiments for both routes were conducted by adding chlorobenzene, instead of the analogous diazonium salt or aniline derivative, to the reduced GNR surfactant suspension. The typical workup procedure was then followed and XPS analysis was done to ensure that the Cl detected in the functionalization reactions was present due to covalent attachment as opposed to physisorption and intercalation of chlorinated material between the ribbons. XPS analysis of the control sample detected <0.1% atomic concentration of Cl present at 200 eV. Hence, this confirms that functionalization was successful and that partial rearomatization of the nanoribbons occurred after hydrazine reduction, thus providing a suitable surface for aryl grafting of the diazonium species.[2,10]

Thermogravimetric analysis (TGA) was used to determine the degree of functionalization of the f-GNRs, by comparing the weight loss of the

functionalized samples to the weight loss of the oxidized GNR starting material and reduced-only GNRs. The TGA weight loss of the f-GNRs is presented in Figure 7.4; the weight loss of all f-GNRs is between 28 – 44%, which falls in the middle of the weight loss recorded for oxidized GNRs (46.3%), and reduced GNRs with no attached functional groups (15%).[1] This indicates that fewer volatile sidewall functionalities are present on the functionalized graphene nanoribbon surface compared with the oxidized starting materials. The reduced ribbons and the product of the control reaction were found to undergo less weight loss, which is due to the absence of functional groups. The defunctionalization of the f-GNRs is estimated to occur between 200 and 700 °C; from these data it is estimated that there is approximately one functional group for every 20~50 carbons.

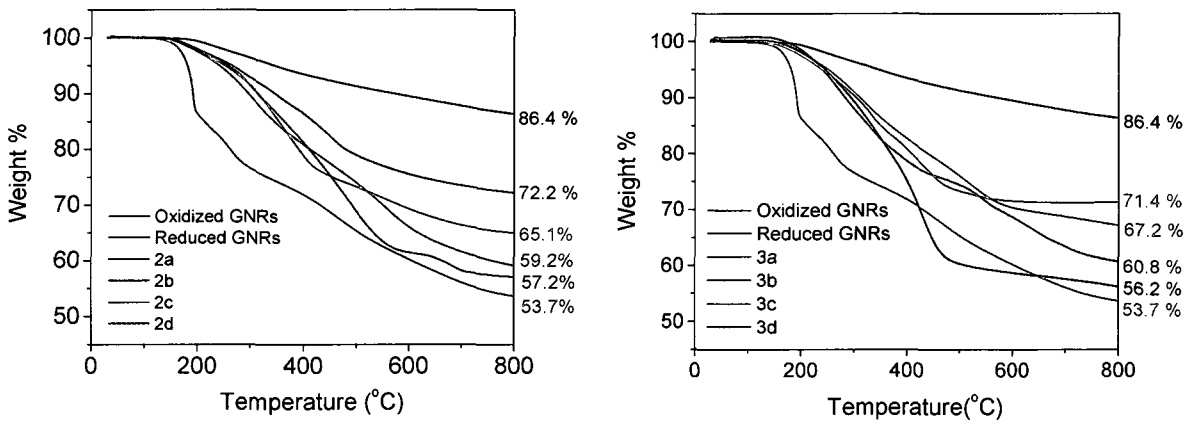

Figure 7.4. TGA thermograms of f-GNRs **2** (left) and **3** (right) compared to oxidized GNR starting material and reduced GNRs with no functional group attached.

The λ_{max} and relative intensities of UV-vis absorption of the different GNR samples indicates the degree of π-conjugation present in the system; a highly conjugated system will have λ_{max} at higher wavelengths and an increased intensity of absorption over the entire spectrum (>230 nm). The UV spectra of the oxidized GNR starting material, reduced GNRs and f-GNRs (**3**) are shown in Figure 7.5a. As expected, a bathochromic shift of λ_{max} and hyperchromicity over the entire range was observed after hydrazine reduction, indicating that electronic conjugation was restored in the oxidized GNR starting material.[15] After functionalization, λ_{max} was hypsochromic shifted while the hypochromicity was maintained over the entire range (>230 nm); this indicates that the conjugated system was shortened slightly by covalent aryl grafting. Although the functionalization decreased the aromaticity of the reduced GNRs, they are still more highly conjugated than the oxidized starting material.

AFM imaging (Figure 7.5b) indicates the presence of long ribbons after the functionalization reactions. The f-GNR shown in Figure 7.5b is greater than 3 μm in length and is a single layer with an average height of ~1.2 nm. In general, the AFM-determined thickness of single layer f-GNRs was measured to be 1.1-1.5 nm, which is slightly higher than that of reduced GNRs (0.75-1.6 nm). It is predicted that single-layer f-GNRs will have increased thickness due to the perpendicular covalent attachment of the functional group moieties and the possibility of diazonium salt polymerization on the GNR surface.

SEM imaging (Figure 7.6) emphasizes the high aspect ratio ribbon structure of the f-GNRs. The typical length is 1 – 5 μm with widths from 80 to

320 nm. Figure 7.6a shows a single-layer folded nanoribbon that is over 2 μm in length and <200 nm wide. Longer few-layered ribbons such as those found in Figures 7.6c-d are representative of many that were imaged, with lengths >6 μm and widths ~300 nm.

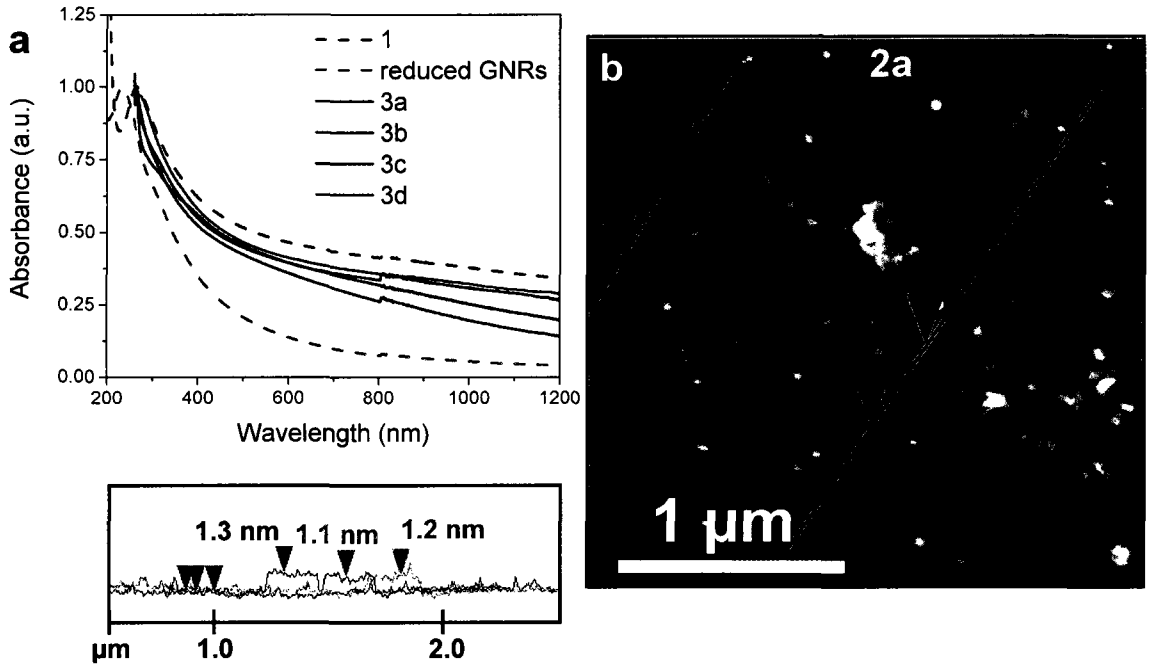

Figure 7.5. a) UV-vis spectra of GNRs and f-GNRs. Spectra of **1** and reduced GNRs were measured in 1 wt% SDS water solution. Spectra of **3a** – **3d** were measured in DMF. b) AFM image of a single, >3 μm long f-GNR from sample **2a**. The height data are given in the bottom left panel.

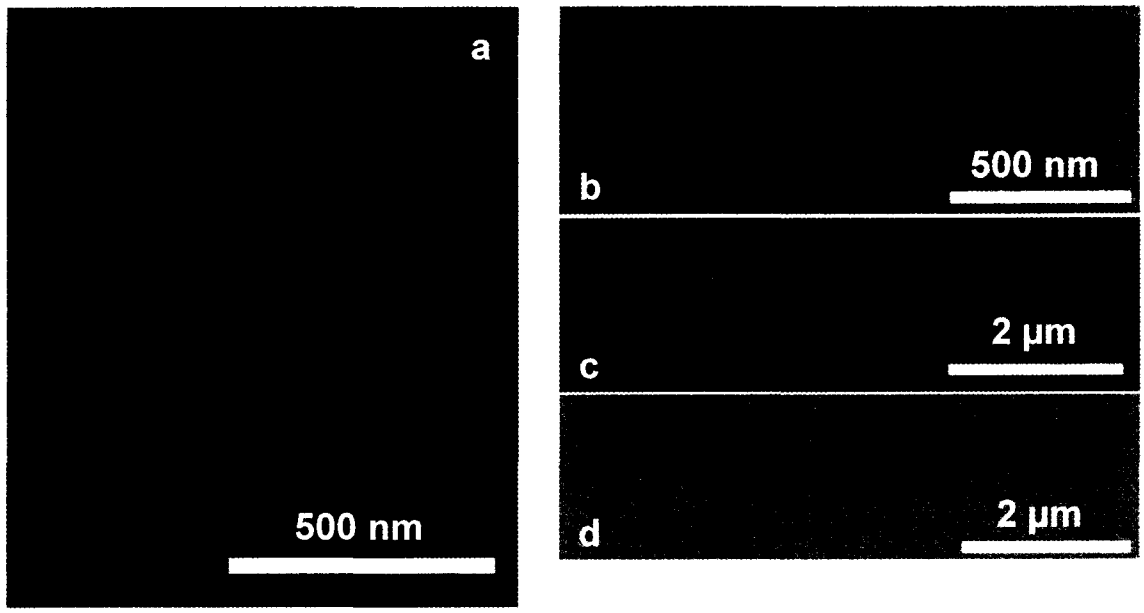

Figure 7.6. SEM images of f-GNRs from sample **2a**. A fresh DMF solution of f-GNRs was prepared and spin-coated onto a silicon surface coated with a 500 nm layer of SiO_2 prior to imaging. The f-GNRs shown in images a-b are single layers while those in c-d are few-layered stacks.

Infrared (IR) spectroscopy is able to identify functional groups with characteristic stretches and was used to confirm the unique presence of the nitro groups in **2c** and **3c**. The attenuated total reflectance IR (ATR-IR) spectrum (Figure 7.7a) of oxidized GNRs shows a C-O stretch at ~1200 cm^{-1}, an O-H/COO-H stretch at 3600-2700 cm^{-1}, and a C=O stretch at 1720-1690 cm^{-1}. The spectrum of the reduced GNRs (Figure 7.7b), however, is devoid of any informative signal and resembles that of the MWCNT (graphite-like) starting material. Figure 7.7c shows the ATR-IR spectrum of f-GNRs **2c**. Asymmetric and symmetric stretches at 1520 and 1340 cm^{-1}, respectively, are attributed to

the NO_2 group while the peak at 852 cm^{-1} can be assigned to the C-N bond. In addition, the aromatic stretch at 1586 cm^{-1} indicates the presence of nitrobenzene moieties on the f-GNRs.[16,17] The presence of NO_2 in **2c** and **3c** was also confirmed by XPS with a strong signal at 405 eV (Figure 7.2).

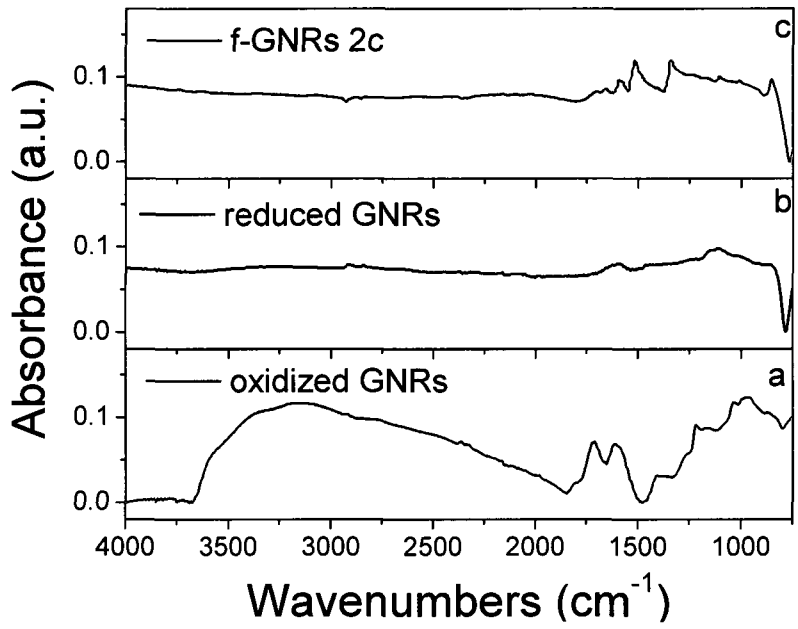

Figure 7.7. ATR-IR spectra of oxidized GNR starting material (a), reduced GNRs (b) and f-GNRs **2c** (c).

The Raman spectra of bulk f-GNRs and reduced GNRs using 633 nm laser excitation (Figure 7.8) show a similar profile to that of the oxidized starting material. The diamondoid (D) to graphitic (G) peak ratio is close to 1, confirming incomplete recovery of the graphene structure, similar to what was observed for functionalized graphene sheets.[2] The degree of functionalization was difficult to gauge using Raman spectroscopy. Edge defects may be responsible for the minimal change in the D/G ratios, and should be even more pronounced in

ribbons than in graphene sheets due to their high percentage of edge to basal plane content.[2]

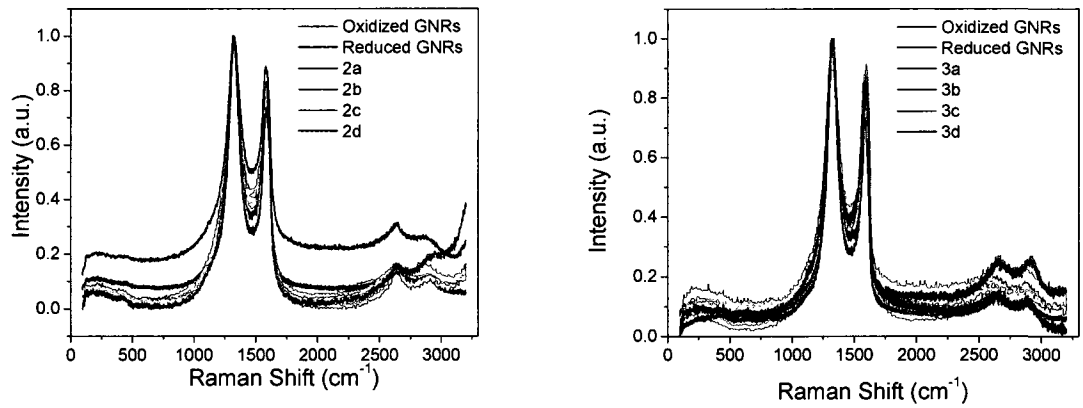

Figure 7.8. Raman spectra (633 nm laser excitation) of oxidized GNRs, reduced GNRs and f-GNRs.

The electrochemical properties of the f-GNRs prepared by Route II were studied using cyclic voltammetry (CV). Oxidative and reductive cycles of **3** are shown in Figure 7.9. The onset potential can be determined from the intersection of two tangents drawn at the rising and background current of the CV. All f-GNRs exhibit oxidative response between 0.84 V and 1.35 V (vs. ferrocenium/ferrocene, Fc^+/Fc), while the reductive response could not be observed even under an air-free environment. This phenomenon is consistent with the reduced state of f-GNRs. The oxidized starting material shows reductive response, which is similar to graphite oxide.[18] The CV experiments confirm that the f-GNRs are in the reduced state.

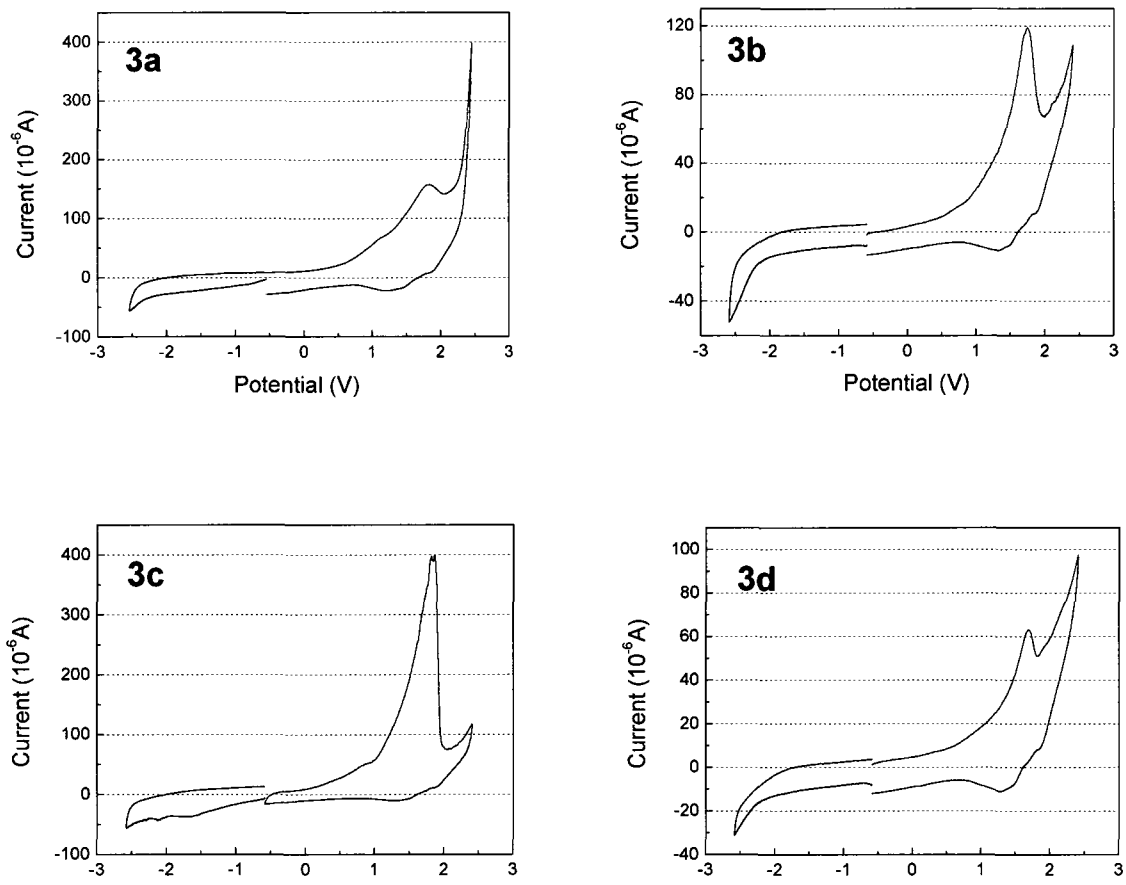

Figure 7.9. Cyclic voltammograms of f-GNRs **3a – 3d**.

The f-GNRs can be readily dispersed in DMF and NMP up to 1 mg/mL with minimal sedimentation. To further illustrate their respective solubilities in DMF, 3 mg f-GNRs was dispersed in 3 mL of DMF using an ultrasonic cleaner (Cole-Parmer model 08849-00) for 5 min followed by centrifugation in an Adams Analytical centrifuge (model CT 3201) for 15 min at 3200 rpm, after which a 2 mL aliquot of each supernatant was precipitated in acetone and filtered. The filter cake was then washed with acetone, dried, and weighed. The supernatant of f-

GNRs gave dark solutions with some sedimentation (see images in Figure 7.10). The solubilities of the f-GNRs are as follows: **2a**, 0.20 mg/mL; **2b**, 0.25 mg/mL; **2c**, 0.35 mg/mL; and **2d**, 0.15 mg/mL; **3a**, 0.15 mg/mL; **3b**, 0.2 mg/mL; **3c**, 0.15 mg/mL; and **3d**, 0.1 mg/mL.

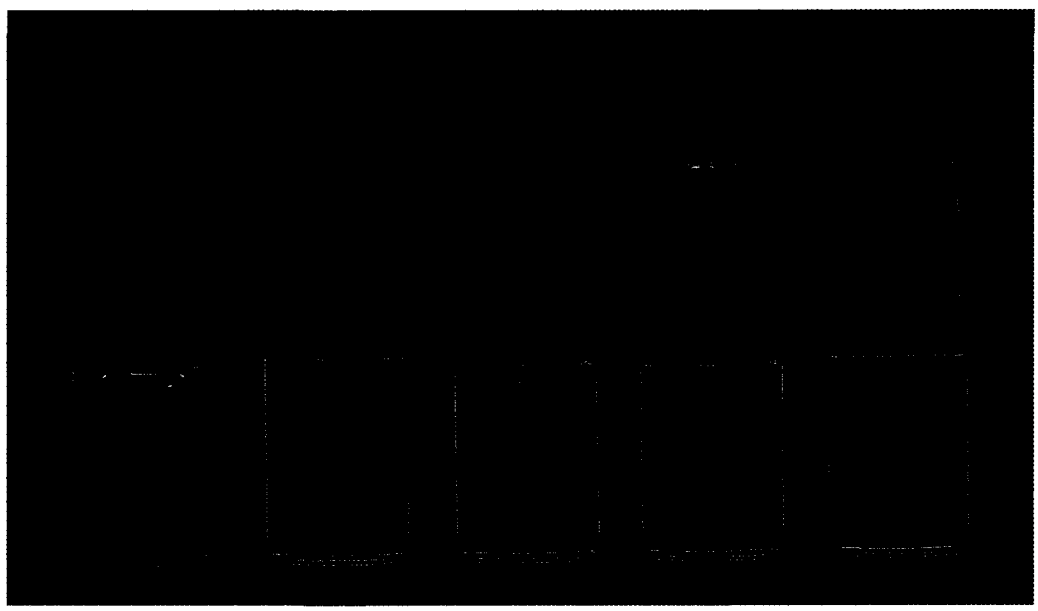

Figure 7.10. Supernatant remaining of post-centrifuged samples for solubility determination in DMF. From left to right, the samples are as follows: unfunctionalized control (reduced only), **2a**, **2b**, **2c**, **2d**.

7.3 Conclusions

Two convenient procedures were developed for the functionalization of graphene nanoribbons, allowing the nanoribbons to become soluble in organic solvents. One of the procedures successfully functionalized graphene material for the first time using in situ generated diazonium salts, which broaden the possibilities of functionality since anilines can be used instead of pre-prepared diazonium salts. Due to their high aspect ratio and soluble properties, these ribbons might be useful materials for applications including composites, fibers and thin film materials, and we are currently exploring those areas.

7.4 Experimental

4-Nitroaniline, 4-chloroaniline, 4-bromoaniline and 2,4-dimethoxyaniline were obtained from Sigma-Aldrich or Acros Organics and used without further purification. Anilines were converted into the corresponding diazonium terafluoroborate via diazotization in aqueous hydrochloric acid followed by addition of fluoroboric acid to precipitate the arenediazonium tetrafluoroborate salt, following the procedure described in the literature.[19] Fluoroboric acid, sodium nitrite, isoamyl nitrite, hydrazine hydrate and acetonitrile were purchased from Fisher or Acros Organics and were used as received. GONRs were prepared from Mitsui MWCNTs using the procedure reported in Chapter 5, section 5.4.1.

7.4.1 General Procedure for the Synthesis of Functionalized GNRs (Route I)

The as-prepared oxidized GNRs were wrapped in SDS surfactant by gently stirring 30 mg of GNRs in 30-mL 1 wt % aqueous sodium dodecylsulfate (SDS) for 1 h, followed by bath sonication of the solution for 10 min (Cole Parmer ultrasonic cleaner, Model 08849-00). The suspension was then filtered through a 5-cm plug of glass wood and transferred to an Erylenmeyer flask. We have found that gentle stirring or short bath sonication of the nanoribbons is fine, however, use of high sheer homogenization, probe sonication, or cup-horn sonication will result in shortened GNRs. Chemical reduction was carried out by adding 30 μL of concentrated NH_4OH (0.444 mmol) followed by 30 μL of $N_2H_4 \cdot H_2O$ (98%, 0.606 mmol). The reaction mixture was heated at 95 °C for 1 h in a gently boiling water bath (no stirring). The heating bath was then removed and the reaction mixture was allowed to cool to room temperature. Functionalization was carried out by pre-dissolving the solid diazonium salt (10 mmol, 4 equivalent per nanoribbon carbon) into a minimum amount of water. This solution was then added dropwise with stirring to the reduced nanoribbon solution. The reaction contents were allowed to stir for 1 h at room temperature. The mixture was then poured into 100-mL acetone to coagulate the f-GNRs. This mixture was filtered through a 0.45 μm PTFE (Teflon) membrane, followed by washing with water and acetone (3x) and resuspended in DMF to remove SDS and excess diazonium salt. This was followed by filtration (0.45 μm PTFE) and copious washing of the filter cake with acetone. The resulting solid was dried at 70 °C in a vacuum oven overnight typically yielding 36-38 mg of f-GNRs.

7.4.2 General Procedure for the Synthesis of Functionalized GNRs (Route II)

The surfactant wrapping and hydrazine reduction of the ribbons (starting from 30 mg oxidized GNRs) were performed as described above. Functionalization was carried out in a 250 mL three neck flask, to which the aniline (10 mmol, 4 equivalent of carbon, predissolved in 30 mL acetonitrile) and 30-mL reduced graphene ribbon solution (1 mg/mL GNRs) were added. To this mixture, isoamyl nitrite (10 mmol) was slowly added dropwise under nitrogen atmosphere. The reaction mixture was heated with stirring to 70 °C for 12 h. The reaction was then cooled and the suspension filtered through a 5-cm plug of glass wool. The filtrate was then filtered through a 0.45 μm PTFE membrane. The filter cake was washed with acetone and re-suspended in DMF, filtered again and the resulting filter cake washed with copious DMF, deionized water and acetone. Though soluble in DMF, the GNRs do not penetrate the filter membrane. The product was collected and dried in vacuo at 70 °C for 24 h before it was used for any characterization and typically yielded 25-35 mg of f-GNRs.

7.4.3 Sample Analysis

All products were characterized by UV-vis, TGA, Raman spectroscopy, ATR-IR, XPS, AFM and SEM as described in Chapter 5, section 5.4.5. Cyclic voltammetry was carried out by casting a thin film of f-GNRs suspended in DMF onto a glass carbon electrode and cycled in degassed, anhydrous acetonitrile

containing 0.1 M tetrabutylammonium hexafluorophosphate as the electrolyte salt. The counter and reference electrodes were platinum and silver, respectively. The voltage data were corrected using ferrocene; scan rate was 25 mVs^{-1} and the temperature was 20 °C.

7.5 References

1. Kosynkin, D. V.; Higginbotham, A. L.; Sinitskii, A.; Lomeda, J. R.; Dimiev, A.; Price, B. K.; Tour, J. M. *Nature* **2009**, *458*, 872-876.
2. Lomeda, J. R.; Doyle, C. D.; Kosynkin, D. V.; Hwang, W.-F.; Tour, J. M. *J. Am. Chem. Soc.* **2008**, *130*, 16201-16206.
3. Bahr, J. L.; Yang, J.; Kosynkin, D. V.; Bronikowski, M. J.; Smalley, R. E.; Tour, J. M. *J. Am. Chem. Soc.* **2001**, *123*, 6536-6542.
4. Bahr, J. L.; Tour, J. M. *Chem. Mater.* **2001**, *13*, 3823-3824.
5. Dyke, C. A.; Tour, J. M. *Nano Lett.* **2003**, *3*, 1215-1218.
6. Li, X.; Wang, X.; Zhang, L.; Lee, S.; Dai, H. *Science* **2008**, *319*, 1229-1232.
7. Yang, X. Y.; Dou, X.; Rouhanipour, A.; Zhi, L. J.; Rader, H. J.; Mullen, K. *J. Am. Chem. Soc.* **2008**, *130*, 4216-4217.
8. Campos-Delgado, J.; Romo-Herrera, J. M.; Jia, X.; Cullen, D. A.; Muramatsu, H.; Kim, Y. A.; Hayashi, T.; Ren, Z.; Smith, D. J.; Okuno, Y.; Ohba, T.; Kanoh, H.; Kaneko, K.; Endo, M.; Terrones, H.; Dresselhaus, M. S.; Terrones, M. *Nano Lett.* **2008**, *8*, 2773-2778.

9. Jiao, L.; Zhang, L.; Wang, X.; Diankov, G.; Dai, H. *Nature* **2009**, *458*, 877-880.

10. Si, Y.; Samulski, E. T. *Nano Lett.* **2008**, *8*, 1679-1682.

11. Dyke, C. A.; Tour, J. M. *J. Am. Chem. Soc.* **2003**, *125*, 1156-1157.

12. Stankovich, S.; Piner, R. D.; Chen, X.; Wu, N.; Nguyen, S. T.; Ruoff, R. S. *J. Mater. Chem.* **2006**, *16*, 155-158.

13. Becerril, H. A.; Mao, J.; Liu, Z.; Stoltenberg, R. M.; Bao, Z.; Chen, Y. *ACS Nano* **2008**, *2*, 463-470.

14. Bekyarova, E.; Itkis, M. E.; Ramesh, P.; Berger, C.; Sprinkle, M.; de Heer, W. A.; Haddon, R. C. *J. Am. Chem. Soc.* **2009**, *131*, 1336-1337.

15. Li, D.; Mueller, M. B.; Gilje, S.; Kaner, R. B.; Wallace, G. G. *Nat. Nanotechnol.* **2008**, *3*, 101-105.

16. Allongue, P.; Delamar, M.; Desbat, B.; Fagebaume, O.; Hitmi, R.; Pinson, J.; Saveant, J.-M. *J. Am. Chem. Soc.* **1997**, *119*, 201-207.

17. Delamar, M.; Hitmi, R.; Pinson, J.; Saveant, J. M. *J. Am. Chem. Soc.* **1992**, *114*, 5883-5884.

18. Kotov, N. A.; Dekany, I.; Fendler, J. H. *Adv. Mater.* **1996**, *8*, 637-641.

19. Curtin, D. Y.; Ursprung, J. A. *J. Org. Chem.* **1956**, *21*, 1221-1225.

7.6 Experimental Contributions

My contribution to the experimental work in this chapter are the following: synthesis of the aryl diazonium salts used in the reactions of Route I, synthesis of products **2a-d**, and all analysis of products **2a-d** including XPS, TGA, ATR-IR, Raman spectroscopy, solubility in DMF, and AFM imaging. Yu Zhu synthesized products **3a-d** and performed XPS, TGA, Raman spectroscopy, solubility in DMF, CV, and AFM/SEM imaging analysis on **3a-d**. The oxidized GNRs used for both functionalization methods were prepared by Dmitry Kosynkin.